

Sheffield Hallam University

Prediction of cutting forces in orthogonal machining.

LAHRECHE, Tahar.

Available from the Sheffield Hallam University Research Archive (SHURA) at:

<http://shura.shu.ac.uk/19936/>

A Sheffield Hallam University thesis

This thesis is protected by copyright which belongs to the author.

The content must not be changed in any way or sold commercially in any format or medium without the formal permission of the author.

When referring to this work, full bibliographic details including the author, title, awarding institution and date of the thesis must be given.

Please visit <http://shura.shu.ac.uk/19936/> and <http://shura.shu.ac.uk/information.html> for further details about copyright and re-use permissions.



POLYTECHNIC LIBRARY
POND STREET
SHEFFIELD S1 1WB

03221

Sheffield City Polytechnic Library

REFERENCE ONLY

~~17/3 17.59~~

14 SEP 2005

SPM

12/8/2006 SPM

ProQuest Number: 10697242

All rights reserved

INFORMATION TO ALL USERS

The quality of this reproduction is dependent upon the quality of the copy submitted.

In the unlikely event that the author did not send a complete manuscript and there are missing pages, these will be noted. Also, if material had to be removed, a note will indicate the deletion.



ProQuest 10697242

Published by ProQuest LLC (2017). Copyright of the Dissertation is held by the Author.

All rights reserved.

This work is protected against unauthorized copying under Title 17, United States Code
Microform Edition © ProQuest LLC.

ProQuest LLC.
789 East Eisenhower Parkway
P.O. Box 1346
Ann Arbor, MI 48106 – 1346

**PREDICTION OF CUTTING FORCES
IN ORTHOGONAL MACHINING**

By

TAHAR LAHRECHE

B.Eng, Annaba University, Algeria

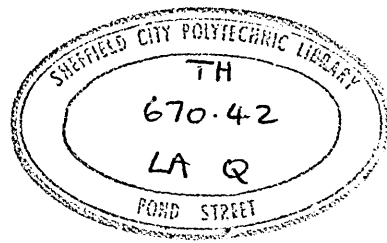
**A THESIS SUBMITTED TO
THE COUNCIL FOR NATIONAL ACADEMIC AWARDS
IN PARTIAL FULFILMENT FOR
THE DEGREE OF MASTER OF PHILOSOPHY**

**Department of Mechanical and Production Engineering
Sheffield City Polytechnic**

October 1987

**Collaborating Establishment:
Davy McKee, Sheffield**

**Sponsoring Establishment:
Sheffield City Polytechnic**



ABSTRACT

PREDICTION OF CUTTING FORCES IN ORTHOGONAL MACHINING

By

T LAHRECHE

In this investigation two methods of machining analysis have been used to make predictions of cutting forces from a knowledge of the workpiece material flow stress and the cutting conditions. The first method of the analysis is used with three different materials namely EN₈, Aluminium and 70-30 Brass. In this analysis the work material flow stress is obtained from a simple quasi-static compression test where the effects of temperature and strain rate are considered to be negligible. Predicted results for the cutting forces obtained from the first method of analysis were compared with experimental results. The comparison of predicted results with experimental results shows only limited agreement.

In order to improve the agreement between experimental and predicted results the machining model was improved by the inclusion of flow stress properties obtained from high speed compression tests. In addition the effect of temperature on the flow stress was allowed for by the use of the velocity modified temperature concept. An excellent agreement is shown between predicted cutting forces obtained from the improved model of machining, with the cutting forces obtained by experiment.

Conclusions are drawn and suggestions for further work are made.

CONTENTS

	<u>Page</u>
ACKNOWLEDGEMENTS	i
DECLARATION	ii
NOMENCLATURE	iii
FIGURES	vi
CHAPTER 1 : INTRODUCTION	1
(i) Empirical Equations	2
(ii) Machinability Data Banks	3
(iii) Analytical Approaches	4
CHAPTER 2 : PREDICTION OF CUTTING FORCES FROM METAL CUTTING ANALYSIS	6
2.1 Description and Terminology of Machining	7
2.2 Chip Formation in Machining	9
2.2.1 Continuous Chip	9
2.2.2 Continuous Chip with Built-Up-Edge	10
2.2.3 Discontinuous Chip	11
2.3 Deformation Zones in Machining	11
2.4 Temperatures in Machining	13
2.5 Forces in Machining	15
CHAPTER 3 : SEMI-EMPIRICAL MODEL OF ORTHOGONAL MACHINING	20
3.1 Introduction	21
3.2 Analysis	21
CHAPTER 4 : EXPERIMENTAL TECHNIQUE AND PROCEDURE	29
4.1 Cutting Tests	30
4.2 Cutting Tools	30
4.3 Workpiece Materials	30
4.4 Compression Tests	31
4.5 Preparation of the Workpieces	32
4.6 Cutting Conditions	33
4.7 Force Measurements	35
4.8 Chip Thickness Measurement	35
4.9 Quick-Stop Device	36
4.10 Measurements of the Dimensions of the Primary and Secondary Shear Zone Widths and the Height of the Built-Up-Edge	37
4.11 The Scanning Electron Microscopy	38

CHAPTER 5 : RESULTS	40
5.1 Variation of the Cutting Forces with Change in Cutting Speed	41
5.2 Variation of the Chip Thickness Ratio with Change in Cutting Speed	41
5.3 Variation of Cutting Forces with a Change in the Undeformed Chip Thickness	41
5.4 Variation of the Chip Thickness Ratio with the Undeformed Chip Thickness	42
5.5 Variation of Cutting Forces with a Change in Rake Angle	42
5.6 Variation of the Chip Thickness Ratio with a Change in Rake Angle	42
5.7 Built-Up-Edge Height and Built-Up-Edge Layer Results	42
5.8 Deformation Zone Measurements	43
5.9 Compression Test Results	43
CHAPTER 6 : DISCUSSION	44
6.1 Introduction	45
6.2 Variation of Cutting Forces with Cutting Speed	45
6.3 Variation of the Chip Thickness Ratio with Cutting Speed	46
6.4 Variation of Cutting Forces with the Change in the Undeformed Chip Thickness	47
6.5 Variation of Cutting Forces with Change in Rake Angle	48
6.6 Assumptions Made in the Semi-Empirical Model used in Chapter 4	48
CHAPTER 7 : MACHINING THEORY ALLOWING FOR STRAIN-RATE AND TEMPERATURE EFFECTS	52
7.1 Introduction	53
7.2 Analysis	53
7.3 Predicted Results from the Machining Model Allowing for Strain Rate and Temperature Effects	59
CHAPTER 8 : CONCLUSIONS AND RECOMMENDATIONS FOR FUTURE WORK	62
8.1 Conclusions	63
8.2 Recommendations for Future Work	64
REFERENCES	65
FIGURES	70

PLATES	118
APPENDICES	139
APPENDIX I : DEMONSTRATION OF SOME EXPRESSIONS USED IN THE SEMI-EMPIRICAL MODEL (CHAPTER 3)	140
APPENDIX II : AN EXAMPLE OF CALCULATING THE FORCES IN USING THE SEMI-EMPIRICAL MODEL	146
APPENDIX III: RESULTS IN TABULATED FORM	149

ACKNOWLEDGEMENTS

The author would like to express his immense gratitude to his supervisor Dr D Gillibrand who has shown much concern and readiness to help during the supervision of the research programme. His indispensable guidance and encouragement are well appreciated.

The author wishes to thank Dr M Sarwar for his help, advice and discussions on many aspects of the work.

The author is also grateful for the resources and facilities provided by the Department of Mechanical and Production Engineering.

The author would also like to acknowledge the assistance provided by Bob Teasdale and the technical staff of the Department of Mechanical and Production Engineering. Particular thanks go to Stewart Leigh, Tim O'Hara and Showmen Bowl.

The author is largely indebted to Ammar Abbachi, Abdullah Alzouabi and Zorlo for their moral support.

The author would also like to take advantage of this opportunity to express his gratitude for the constant encouragement given to him by his family throughout the period of the present work.

Last, but not least, special thanks are due to Maggie Bedingham for typing this thesis.

NOMENCLATURE

C	Constant in the empirical strain-rate relation (Equation 7.2)
F	Friction force
F_c	Horizontal cutting force
F_s	Shearing force
F_t	Vertical cutting force (or thrust force)
h	Tool-chip contact length
K	Shear flow stress
k	Thermal conductivity of the work material in Equation (7.8)
K_{AB}	Shear flow stress at AB
L	Length of AB
m	The slope of the idealized stress-strain curve
N	Force normal to the shear plane
n	Strain hardening index
P	Hydrostatic stress at any point
P_A	Hydrostatic stress at point A
P_B	Hydrostatic stress at point B
R	Resultant cutting force
r_c	Chip thickness ratio
R_T	Thermal number
S	Specific heat of work material
s	Cutting feed
s_z	Length to the width of the shear zone $\left[\frac{t_1}{\Delta S_1 - \sin \varphi} \right]$
t_1	Undeformed chip thickness
t_2	Chip thickness

T_{AB}	Temperature at AB
T_c	Average temperature rise in the chip
T_{int}	Average temperature at the tool-chip interface
T_M	Maximum temperature rise in the chip
T_w	Initial work temperature
U	Cutting speed
V_c	Chip velocity
V_s	Shear velocity
w	Width of cut
α	Rake angle
ΔK	Total change in shear flow stress
ΔS_1	Width of the primary shear zone
ΔS_2	Undeformed length of the small element of the shear zone measured along AB
Δp	The change in the hydrostatic stress
δt_2	Width of the secondary shear zone
φ	Shear angle
ϵ	Natural strain
$\dot{\epsilon}$	Direct strain
ϵ_0	Constant in Equation (7.18)
η	Constant in Equation (7.6)
γ_{AB}	Shear strain along AB
$\dot{\gamma}_{AB}$	Maximum shear strain rate
γ_{EF}	Total shear strain
$\dot{\gamma}_{int}$	Maximum shear strain rate at the tool-chip interface
λ	Friction angle
σ_1	Flow stress at strain ($\epsilon = 1$)

$\bar{\sigma}$	True stress
σ_N	Average normal stress
θ	Angle made between the resultant cutting force and the shear plane AB (Figure 27)
ψ	Angle made between a tangent to the slip line field " α " at any point and a reference axis "x"

LIST OF FIGURES

	<u>Page</u>
FIGURE 1 : Machining process	71
FIGURE 2 : Cutting operation	72
FIGURE 3 : Orthogonal machining with the lathe method	73
FIGURE 4 : Section through the tool and chip	73
FIGURE 5 : Rake angle sign	74
FIGURE 6 : Shear plane model of chip formation	74
FIGURE 7 : Continuous chip type	75
FIGURE 8 : Continuous chip with built-up-edge type	75
FIGURE 9 : Cycle of built-up and break down	76
FIGURE 10: Built-up-edge occurrence	76
FIGURE 11: Discontinuous chip type	77
FIGURE 12: Primary and secondary deformation zones	78
FIGURE 13: Shear zone model	79
FIGURE 14: Slip field model	79
FIGURE 15: Deformation zone model	79
FIGURE 16: Generation of heat in orthogonal cutting	80
FIGURE 17: Temperature distribution in workpiece and chip during orthogonal cutting for free cutting mild steel	80
FIGURE 18: Idealized model of cutting process employed in theoretical work on cutting temperature	81
FIGURE 19: Effect of $R \tan \phi$ on division of shear zone heat between chip and workpiece	81

FIGURE 20:	Effect of cutting speed on cutting temperature (theoretical)	82
FIGURE 21:	Variation in tool-chip interface temperature with cutting speed	83
FIGURE 22:	Variation in shear zone temperature with cutting speed	83
FIGURE 23:	Variation in tool-chip interface temperature with depth of cut	84
FIGURE 24:	Variation in shear zone temperature with depth of cut	84
FIGURE 25:	Shear plane model of analysis	85
FIGURE 26:	The diagram of forces	85
FIGURE 27:	The shear plane model	86
FIGURE 28:	Model of analysis presented by Okushima and Hitomi	87
FIGURE 29:	Idealized shear flow stress-strain curve	87
FIGURE 30:	Geometry of cutting	88
FIGURE 31:	Configuration of the specimen used in the compression test	89
FIGURE 32:	Plain strain section	89
FIGURE 33:	Principle of the scanning electron microscope	90
FIGURE 34:	Variation of the cutting forces with change in cutting speed in machining EN ₈	91
FIGURE 35:	Variation of the cutting forces with change in cutting speed in machining Aluminium	92
FIGURE 36:	Variation of the cutting forces with change in cutting speed in machining 70-30 Brass	93
FIGURE 37:	Variation of the chip thickness ratio with cutting speed	94

FIGURE 38:	Variation of the cutting forces with change in the undeformed chip thickness in machining EN ₈	95
FIGURE 39:	Variation of the cutting forces with change in the undeformed chip thickness in machining Aluminium	96
FIGURE 40:	Variation of the cutting forces with change in the undeformed chip thickness in machining 70-30 Brass	97
FIGURE 41:	Variation of the chip thickness ratio with the undeformed chip thickness	98
FIGURE 42:	Variation of the cutting forces with a change in rake angle when machining EN ₈	99
FIGURE 43:	Variation of the cutting forces with a change in rake angle when machining Aluminium	100
FIGURE 44:	Variation of the cutting forces with a change in rake angle when machining 70-30 Brass	101
FIGURE 45:	Variation of the chip thickness ratio with change in rake angle	102
FIGURE 46:	True stress-strain curve for EN ₈	103
FIGURE 47:	True stress-strain curve for Aluminium	104
FIGURE 48:	True stress-strain curve for 70-30 Brass	105
FIGURE 49:	Variation of the cutting forces with cutting speed in machining EN ₈	106
FIGURE 50:	Variation of the cutting forces with cutting speed in machining Aluminium	107
FIGURE 51:	Variation of the cutting forces with cutting speed in machining 70-30 Brass	108
FIGURE 52:	Variation of the cutting forces with change in the undeformed chip thickness	109
FIGURE 53:	Variation of the shear flow stress with shear strain	110
FIGURE 54:	Model of chip formation	111

FIGURE 55:	Flow stress (σ_1) and strain hardening index (n) variations with velocity modified temperature	112
FIGURE 56:	Variation of cutting forces with cutting speed	113
FIGURE 57:	Variation of cutting forces with the undeformed chip thickness	114
FIGURE 58:	Variation of cutting forces with change in rake angle	115
FIGURE 59:	Machining model to determine the expression of $\tan \varphi$	116
FIGURE 60:	Machining model used to determine the expression $\theta = \varphi - \alpha + \lambda$	117

A knowledge of the cutting forces in a machining operation is of considerable value to the engineer engaged in the design of machine tools, the production engineer responsible for the selection of a cutting tool, the metallurgist who must provide cutting tool materials with the appropriate strength and hardness, and the production planner who must select suitable jigs and fixtures.

The four decades following the end of the second world war have seen an enormous effort directed towards the measurement of the forces which arise when cutting a workpiece, and coupled with this effort have been many investigations into the physical fundamentals of the cutting process. One of the principal objectives of these investigations has been the development of methods which would allow the prediction of cutting forces from the machining conditions and the workpiece material properties, thus offsetting the need to carry out expensive and time consuming cutting force measurements.

A survey of the work carried out shows that the problem of cutting force prediction has been approached in three different, although overlapping ways.

(i) Empirical Equations

Machining processes are characterised by very large numbers of variables which derive from the wide range of types of machining operation (single-point or multi-point cutting for example), the different types of workpiece material each with its own specific properties, coupled with the geometrical and kinematic aspects of any particular machining operation (for example, workpiece dimensions and shape, cutting speed; feed, depth of cut etc).

On the basis of extensive practical machining tests some investigators have attempted to classify the above variables into generic groups, eg workpiece properties, each of which can be represented by a coefficient, or constant. The group coefficients may then be incorporated with the cutting variables, eg speed, feed, depth of cut, into empirical equations for cutting force, power or surface finish. The most detailed account of the procedures involved in the development of empirical equations is that due to Kronenberg [1].

The principal restriction on the development of empirical equations is the extensive testing which is necessary, because this involves considerable cost in terms of both time and money.

(ii) Machinability Data Banks

Banks of machining data have been developed over many years in particular by large industrial companies associated with the aerospace industries. One of the earliest data banks was established by Metcut Research Associates who carried out extensive practical conventional and non-conventional cutting tests for the American space programme. In more recent years the advent of large computers with massive data storage capabilities coupled with rapid retrieval has rekindled interest in machinability data banks. More recently established data banks incorporate information obtained from in-practice machining rather than from machining tests. The strength of data banks lies in their ability to provide information, concerning the machining of a new component, based on previous experience of machining similar components. Although modern data banks incorporate some empirical equations their ability to predict cutting forces, power and surface roughness is limited in cases where data from earlier

machining situations is unavailable.

(iii) Analytical Approaches

A study of the machining literature shows that many attempts have been made to predict the cutting forces, roughness, tool wear, power etc, on the basis of fundamental studies of the deformation occurring during a machining process. Early attempts were based on a shear plane model of machining as described in Chapter 2, while later models have attempted to allow for the behaviour of the workpiece material as it passed through finite deformation zones.

In recent years models of the machining process have been analysed using slip-line field and finite-element techniques of stress analysis. Such models require large computers and extensive computer time if realistic results are to be obtained. This latter fact has restricted the use of analytical techniques based on slip-line field and finite-element methods.

It is clear that each of the above approaches to machining has its strengths as well as its weaknesses. In the last fifteen years a further alternative approach to machining has been developed by a number of workers which attempts to combine the simplicity of the early analytical approaches based upon the shear plane, or "thin" shear zone, with empirical data relating to the properties of the workpiece material and the deformation zone dimensions. The type of machining model assumed is sometimes referred to as a "semi-empirical" model.

The results of a limited number of studies using a semi-empirical model of machining have been reported, and the results for cutting forces and cutting temperatures look promising. However, results have only been reported for low and medium carbon steel. It would be valuable to investigate the accuracy with which cutting forces are predicted by the semi-empirical method, and also the case with which the semi-empirical method can be extended to non-ferrous materials.

CHAPTER 2

PREDICTION OF CUTTING FORCES FROM METAL CUTTING ANALYSIS

- 2.1 Description and Terminology of Machining
- 2.2 Chip Formation in Machining
 - 2.2.1 Continuous Chip
 - 2.2.2 Continuous Chip with Built-Up-Edge
 - 2.2.3 Discontinuous Chip
- 2.3 Deformation Zones in Machining
- 2.4 Temperatures in Machining
- 2.5 Forces in Machining

2.1 Description And Terminology Of Machining

A machining process is basically a simple process in which the required surface is generated by providing suitable relative motion to the cutting tool and the workpiece. To produce the required surface, all conventional metal cutting operations are similar in that the cutting tool removes a layer of material called a chip as shown in Figure 1.

Simple cutting operations usually adopt one of the two basic tool workpiece geometries illustrated in Figure 2, and which are known as oblique and orthogonal machining operations respectively.

If the angle between the cutting edge and the cutting speed motion is other than a 90 degree angle, then the cutting geometry is known as oblique (Figure 2a). If the angle formed by the cutting edge and the cutting speed motion is equal to a 90 degree angle, this is known as orthogonal machining as shown in Figure 2b.

Although in practice, most metal cutting operations are oblique, most of the research investigation, concerned with the mechanics of cutting have dealt with orthogonal machining, since this is effectively two dimensional.

Orthogonal machining can be carried out on a shaping (or planing) machine where the tool reciprocates over the workpiece, taking a cut on the forward stroke. In shaping or planing operations, the cutting speeds are limited and the cutting action is intermittent.

An alternative arrangement which allows continuous cuts of longer duration is shown in Figure 3. This figure depicts the lathe method used for orthogonal machining, which is widely used in research investigations.

Figure 4 shows a section perpendicular to the cutting edge through the tool and chip. From Figure 4 it is shown that the cutting tool consists of two surfaces intersecting to form the cutting wedge. One surface along which the chip flows is known as the rake face, and the other face of the cutting tool is known as the flank face. In order to prevent rubbing between the flank face and the new machined surface, the cutting tool is provided with a clearance angle.

One of the more important variables in a machining process is the slope of the tool rake face, and this slope is specified in orthogonal machining by the angle between the tool face and a line perpendicular to the machined surface. This angle is known as the rake angle " α ", and Figure 5 illustrates how the sign of the rake angle is defined.

In orthogonal machining, the depth of the material removed by the action of the tool with a cutting speed " u " is known as the undeformed chip thickness " t_1 " (Figure 4). The thickness of the chip is known as the chip thickness " t_2 ".

The ratio of the undeformed chip thickness to the chip thickness (ie t_1/t_2) is known as the chip thickness ratio " r_c ". The acute angle which is formed between the plane AB (Figure 6) and the direction of cutting is termed the shear angle " ϕ ".

The following sections have been included to give an overview of the main features which are likely to be encountered during a machining operation, and which can have a great effect on the prediction of the cutting forces.

2.2 Chip Formation In Machining

Whatever the cutting conditions may be, the chips produced are one of the three basic types, which were classified by Ernest [2] as follows:

- (i) Continuous chip
- (ii) Continuous with built-up edge

and

- (iii) Discontinuous chip.

2.2.1 Continuous Chip

The continuous chips are associated with the machining of the more ductile materials, such as mild steel at high speeds, copper, and aluminium. Machining with this type of chip gives good surface finish, low cutting forces, low cutting temperatures, and long tool life.

Most of the research conducted into metal cutting has dealt with continuous chip production since it can be considered to be a steady-state process. The formation of a continuous chip is shown in Figure 7.

2.2.2 Continuous Chip With Built-Up-Edge

This type of chip formation is shown in Figure 8. It is similar to the continuous chip (stated above), except that hard metal builds upon the tool tip and acts as a very rough cutting tool, usually causing a deterioration in the surface finish of the workpiece.

According to Nakayama [3] this type of chip formation occurs at speeds where the temperature at the chip-tool interface is relatively low, so that fracture may occur within the chip along a plane approximately at right angles to the shear plane, leaving behind a portion of chip attached to the tool face, as shown in Figure 8. This attached material then acts as the cutting edge of the tool, and is called a built-up-edge.

Built-up-edge formation is a dynamic phenomenon in which the size of the built-up-edge increases until it becomes unstable, fracture occurs, and sections of the built-up-edge are carried away in the underside of the chip and on the machined surface. Experimental work was carried out by Shwerd [4] on the built-up-edge formation cycle. It was shown [4] that when machining with conditions which promote built-up-edge formation, an extremely rapid cycle of build-up and break-down is illustrated in Figure 9.

Trent [5] has shown that the conditions which promote the formation of the built-up-edge when machining steel and cast iron may be summarized on a graph of $\log(v)$ versus $\log(\text{feed})$, and built-up-edge occurrence is then bounded by a straight line as shown in Figure 10.

2.2.3 Discontinuous Chip

Figure 11 shows the formation of a discontinuous chip. Discontinuous chips are produced when machining brittle materials such as grey cast iron and bronze, and normally ductile materials such as mild steel, at very low speeds and high feeds. The tool partly forms the chip before fracture occurs resulting in the formation of a discontinuous chip.

From an observation made by Iwata and Ueda [6] of the machining process inside a scanning electron microscopy, it was stated [6] that the type of chip formation transformed occasionally from one type to another, depending on changes in microscopic parameters (eg inclusions, morphology and grain boundaries) and in cutting conditions (eg rake angle and cutting speed).

The merit of each type of chip formation depends on which aspect of a machining process needs to be controlled. For the purpose of this investigation the continuous type of chip formation is most relevant since it can be treated as a steady-state process.

2.3 Deformation Zones In Machining

Studies carried out by many workers [7-12] have established that the process of chip formation during a machining operation involves a considerable amount of plastic flow. The bulk of this work occurs in two zones known as the primary and secondary deformation zones respectively as shown in Figure 12.

The primary deformation zone is due to the extensive shear which accompanies chip formation. At high cutting speeds with a continuous chip the primary deformation zone resembles a narrow, parallel sided band which has been treated as a "shear plane" for the purpose of analysis by numerous workers [13-16]. Further attention will be given to the "shear plane" approach to machining in Section 2.5.

The secondary deformation zone arises due to the contact between the chip and the rake face of the cutting tool. This contact is characterised by heavy shear in lower layers of the chip producing a further amount of deformation.

Palmer and Oxley [17] studied the deformation in metal cutting. Using cinephotography to observe the flow of grains in a steel workpiece during slow-speed cutting, they found that the primary deformation zone had the form shown in Figure 13. This model was criticized because only very low speeds were used and also the tool and the chip are not in contact at the tool point.

A slip line field model constructed by Enahoro and Oxley [18] is shown in Figure 14. This model demonstrates how the interaction between the chip and the tool affect the deformation in the lower layers of the chip.

Roth and Oxley [19] have constructed a model for the deformation zones which is a combination of the slip line field models previously proposed [17,18] and is shown in Figure 15.

The deformation zone in machining is very small [20] and it has been suggested that a size effect exists in which the flow stress in the deformation zone is greater than that of the bulk material. The flow stress can be increased significantly by

the high values of strain and strain rate. Both the strain and strain rate are known to have high values in metal cutting in the range 1 to 3 in the case of strains and between 10^5 and 10^6s^{-1} for strain-rates. The flow stress is reduced at high temperatures which can in machining reach values in excess of 800°C . The temperatures in machining will be dealt with in Section 2.4.

2.4 Temperatures In Machining

The extensive plastic deformation occurring in the primary and secondary deformation zones is accompanied by significant heat generation and high temperatures.

During machining heat is generated in the region of the tool cutting edge [21].

This heat can have a controlling effect on the properties of the workpiece material being machined, the rate of wear of the cutting tool, on friction between the chip and the tool, and thus, on the prediction of the cutting forces.

In machining, the workpiece material being machined is subjected to high strains, and the elastic deformation forms a very small proportion of the total deformation [21]. It was assumed by Trent [21] that all the energy is converted into heat (eg when the material is deformed plastically).

Boothroyd [22] stated that the conversion of the energy into heat occurs in the primary and secondary deformation zones as depicted in Figure 16.

Figure 17 shows the experimental work carried out [22] for the determination of the temperature distribution in the workpiece and the chip during an orthogonal machining. In his attempt to calculate the temperature distribution, Boothroyd [22] deduced that the generation of heat was confined uniformly within the shear plane and the chip-tool interface rather than being propagated over a finite primary and secondary shear zones.

Several theoretical analyses of the temperature distribution in the workpiece and chip-tool interface have been carried out [23 to 26]. Figure 18 shows the idealized model of the cutting process employed in theoretical analyses [23 to 26]. In these attempts it was assumed that the primary shear zone could be regarded as a plane heat source of uniform strength (ie no heat is lost from the free surfaces of the workpiece and the chip, and that the thermal properties of the workpiece material were constant and independent of the temperature).

In an attempt to find an exact solution to calculate the temperature in the workpiece and at the tool-chip interface, Rapier [26] deduced that an exact solution was not possible and further assumptions were necessary.

A useful suggestion was made by Nakayama [27], who assumed that no heat was conducted in the material in the direction of its motion. Nakayama [27] carried out experimental work and compared the results obtained to the theoretical analysis suggested by the experimental and theoretical results are shown in Figure 19.

One conclusion was deduced [27], that is the maximum temperature in the chip occurs where the material leaves the secondary deformation zone.

Murarka et al [28] carried out experimental machining tests in which the cutting temperature was measured for a range of 150 and 700°C. It was shown that (i) the mean shear zone temperature increases slightly with increasing the cutting speed, and tends to become constant and (ii) the maximum tool-face temperature increases rapidly with an increase in cutting speed. This is shown in Figure 20.

From the work carried out by Hashmi [29] it is deduced that the shear zone temperature and the tool-chip interface temperature increase with an increase in cutting speed as shown in Figures 21 and 22. The tool-chip interface temperature (Figure 23) increases slightly with an increase in the undeformed chip thickness, and the shear zone temperature increases to a certain value and then decreases as the undeformed chip thickness increases as depicted by Figure 24.

It can be concluded from the foregoing work on the cutting temperatures that the temperature changes with a change in cutting parameters such as cutting speed and undeformed chip thickness. This change in cutting temperature can have a controlling effect on the properties of the work material and hence on the cutting forces.

2.5 Forces In Machining

Investigators in the metal cutting field have attempted to develop an analysis of the cutting process which provides a clear understanding of the fundamentals of the process and which enables the prediction of cutting forces without the need for empirical testing. It should be realised that relatively simple cases have been studied and that the available methods of analysis have not been explored or extended to allow for cutting with two or more cutting edges or with form tools. For a number of operations where cutting is performed essentially with one cutting

edge, eg turning, the cutting theory is used to predict the important forces (ie the horizontal and vertical cutting force).

The cutting theory which can predict the cutting forces can only be used under one model of machining.

Several models to describe the process of machining have been developed; some have been fairly successful in describing the process, but none can be fully substantiated and definitely stated to be the correct solution. Thus, while none of the analyses can precisely predict conditions in a practical cutting situation, the analyses are worth examining because they can qualitatively explain phenomena observed and indicate the direction in which conditions should be changed to improve cutting performance.

As early as 1945 Merchant [13] had developed an analysis based on the thin shear plane model (Figure 25) within which he made the following assumptions:

- (i) The tool tip is sharp and no rubbing or ploughing occurs between the tool and the workpiece.
- (ii) The deformation is two dimensional, ie no side spread.
- (iii) The stresses on the shear plane are uniformly distributed.
- (iv) The resultant force "R" on the chip applied at the shear plane is equal, opposite and collinear to the force R applied to the chip at the tool chip interface.

For these conditions a force diagram as shown in Figure 26 was constructed.

The cutting force (ie horizontal and vertical) were established as:

$$F_c = \frac{t_1 w K_{AB}(\lambda-\alpha)}{\sin \varphi \cos(\varphi+\lambda-\alpha)} \quad (2.1)$$

$$F_t = \frac{t_1 w K_{AB} \sin(\lambda-\alpha)}{\sin \varphi \cos(\varphi+\lambda-\alpha)} \quad (2.2)$$

where:

- F_c - horizontal cutting force
- F_t - vertical cutting force
- t_1 - undeformed chip thickness
- w - width of cut
- K_{AB} - shear stress
- λ - friction angle
- α - rake angle
- φ - shear angle

To determine the shear angle, Merchant [13] assumed that the minimum-energy principle applied in metal cutting, so that the deformation process adjusted itself to a minimum energy condition. He established this condition by equating $dF_p/d\varphi$ to zero, for constant cutting speed, that is,

$$\frac{dF_p}{d\varphi} = \frac{t_1 w K_{AB} \cos(\lambda-\alpha) \cos(2\varphi+\lambda-\alpha)}{\sin^2\varphi \cos^2(\varphi+\lambda-\alpha)} = 0$$

$$\varphi = \frac{\pi}{4} - \frac{1}{2} (\lambda-\alpha) \quad (2.3)$$

The cutting forces were therefore expressed as

$$F_c = \frac{t_1 w K_{AB} \cos(\lambda-\alpha)}{\sin[(\pi/4)-(\frac{1}{2})(\lambda-\alpha)] \cos[(\pi/4)+(\frac{1}{2})(\lambda-\alpha)]}$$

$$= 2t_1 w K_{AB} \cot \varphi \quad (2.4)$$

and

$$F_t = \frac{t_1 w K_{AB} \sin(\lambda-\alpha)}{\sin[(\pi/4)-(\frac{1}{2})(\lambda-\alpha)] \cos[(\pi/4)+(\frac{1}{2})(\lambda-\alpha)]}$$

$$= t_1 w K_{AB} (\cot^2\varphi - 1) \quad (2.5)$$

Equations (2.3), (2.4) and (2.5) were based on two further assumptions which make them open to considerable doubt. First they involve the minimum-energy principle, which is not supported by evidence; second, the differentiation assumed λ and K_{AB} are constants, independent of φ .

Merchant [13] ran experimental tests to determine the forces, shear angle, coefficient of friction and shear-plane stresses in metal cutting. He found that the values obtained were different from the values expected. Quantitatively the shear angle relationship (equation (2.3)) has been found to be inaccurate. Also the shear stresses and coefficient of friction values were higher than those established by conventional tensile and friction tests.

Oxley [30] applied a simplified slip-line field to a shear plane model in metal cutting. The model is shown in Figure 27. In his model [30] the deformation zone was assumed to be bounded by straight and parallel slip lines at an angle φ to the direction of motion. In his analysis [30] Oxley has expressed the shear angle by the relationship

$$\varphi = 50 - 0.8(\beta - \alpha) \quad (2.6)$$

Experimentally, equation (2.6) was found to agree with measured shear-angle values somewhat closer than equation (2.3), but it is not an exact expression.

The deformation in metal cutting at very low speeds was studied by Palmer and Oxley [16], and they have presented a model shown in Figure 13 for their analysis. In this model they suggested that the tool chip and the tool were not in contact at the tool tip and that the chip was curved so that the contact zone was some distance up the rake face of the tool. A disappointing feature of Palmer and Oxley's analysis is that the deformation cannot be predicted analytically, so

that the cutting forces cannot be predetermined.

Another model of analysis shown in Figure 28 has been presented by Okushima and Hitomi [31]. No attempt was made to fit a slip-line field to the deformation zone, but the analysis was based purely on the geometry of the boundaries of the zone. In some ways it was similar to the Merchant analysis except that a range of shear planes was considered.

From the foregoing models of analysis, the zone of deformation approaches the shear plane model as the cutting speed is increased. The model used for analysis by Oxley [30] with the shear zone approaching the shear plane seems to be the most valid. This model of analysis which is based on two main assumptions (i) the width to the length shear zone is taken as a constant and (ii) the flow stress data is taken to have the value of a quasi-static stress where the effects of strain rate and temperature are not considered. This model is then referred to as the semi-empirical model of machining and is used in this investigation with three different materials as described in the following chapter.

CHAPTER 3

SEMI-EMPIRICAL MODEL OF ORTHOGONAL MACHINING

- 3.1 Introduction
- 3.2 Analysis

3.1 INTRODUCTION

It is usual when considering the mechanics of metal cutting [1-8] to restrict attention to orthogonal machining as described previously in Chapter 2, section 1, and it is usual to consider conditions under which the metal is removed in the form of a continuous chip.

Orthogonal machining with a continuous chip can be approximated to a plane strain steady motion problem and it is this class of problem which can be most easily analysed.

In the present investigation a semi-empirical model of machining has been used. The semi-empirical model incorporates theoretical aspects of analysis along with experimentally determined values, namely the shear zone length to width ratio and the work material properties.

3.2 MACHINING ANALYSIS

The model of chip formation used in this analysis in which the chip is formed in a finite plastic zone is shown in Figure 27a. The finite plastic zone is idealized to a parallel sided shear zone, with AB, CD and EF straight parallel slip-lines representing the directions of maximum shear-stress and maximum shear-strain rate. Chip curl is neglected and it is assumed that the state of strain, and therefore the shear flow stress, along each of the parallel slip-lines is constant.

Neglecting any up-thrust on the base of the tool, the slip-line AB (Figure 27a) will transmit the resultant cutting force and it is therefore convenient to base the analysis on the slip-line AB.

The method of analysis is to analyse the stresses along AB and then to select the values of shear angle " φ " (ie the angle made by shear plane AB and the direction of cutting) to give a resultant cutting force direction across AB which is consistent with the direction given by considering the angle of friction at the tool-chip interface. From a geometrical view point AB can be looked upon as the shear plane and φ as the shear angle. The angle φ is given by the following expression as demonstrated in Appendix I:

$$\tan \varphi = \frac{t_1/t_2 \cos \alpha}{1 - t_1/t_2 \sin \alpha} \quad (3.1)$$

where

t_1 : undeformed chip thickness

t_2 : chip thickness

and

α : rake angle.

To describe the stress conditions in the plastic zone, modified Hencky relationships [32] with a workhardening term are used. These are:

$$p + 2k\psi + \int \frac{\Delta k}{\Delta s_2} \Delta s_1 = \text{const along } (\alpha) \text{ line}$$

$$p + 2k\psi + \int \frac{\Delta k}{\Delta s_1} \Delta s_2 = \text{const along } (\beta) \text{ line}$$

(3.2)

where:

- p : the hydrostatic stress at any point
 k : shear flow stress
 ψ : angle made between a tangent to the slip-line " α " at any point and a reference axis " x "
 Δk : the total change in shear flow stress
 Δs_1 : the width of the shear zone

and

- Δs_2 : undeformed length of the small element of the shear zone measured along AB, shown in Figure 27b.

The hydrostatic stress in the region of A is calculated from the free surface condition in the surface ahead of A. At the free surface (ie in the region of A in Figure 27a) the following conditions are assumed to apply:

- (i) Boundary AB bends to meet the free surface at 45° (ie free surface condition);
(ii) No force is exerted at the tool tip;
and
(iii) The tangential and normal stresses on the rake face of the tool are uniformly distributed over the tool-chip contact region.

It follows from assumption (i) above that as $p = k$ (compressive) at the free surface it can be shown from slip-line theory that

$$p_A = k_{AB} \left[1 + 2 \left[\frac{\pi}{2} - \varphi \right] \right] \quad (3.3)$$

where:

p_A : is the hydrostatic stress at A (ie the normal stress acting on AB at A).

From Figure (27b) (ie the small element of the shear zone) as the material passes through the shear zone its shear flow stress will change as a result of strain-hardening and temperature. Therefore, the shear flow stress along CD (ie initial shear flow stress at zero plastic strain) is $k - \Delta k/2$, and the shear flow stress along EF is $k + \Delta k/2$.

Resolving forces parallel to AB as demonstrated in Appendix I gives:

$$\Delta p = \frac{\Delta k}{\Delta s_1} \cdot \Delta s_2 \quad (3.4)$$

where:

Δp : is the change in the hydrostatic stress.

Applying this equation between A and B, it can be obtained:

$$p_A - p_B = \frac{\Delta k}{\Delta s_1} \cdot \frac{t_1}{\sin \varphi} \quad (3.5)$$

$$p_B = p_A - \frac{\Delta k}{\Delta s_1} \cdot \frac{t_1}{\sin \varphi} \quad (3.6)$$

where:

p_B : is the hydrostatic stress at B (ie normal stress on AB at B).

In order to calculate the hydrostatic stress p_B in equation (3.6), it is necessary to know the value of the total change in the shear flow stress Δk between A and B. Therefore, let Figure 29 represent the idealized shear flow stress - shear strain curve of the material corresponding to the shear strain rate in the shear zone (the

slope of the curve and the total change in the shear flow stress will vary with strain rate [34]). Then if the total shear strain occurring as an element of material passes through the shear zone at the slip-line EF is γ , then from CD to EF the change in shear flow stress is given by

$$\Delta k = m \cdot \gamma_{EF} \quad (3.7)$$

where:

m : is the slope of the idealized stress-strain curve
and γ_{EF} (the total shear strain) is given by [34] that is:

$$\gamma_{EF} = \frac{\cos \alpha}{\sin \varphi \cos(\varphi - \alpha)} \quad (3.8)$$

The shear strain occurring along the slip-line AB (γ_{AB}) is given by

$$\gamma_{AB} = \frac{\cos \alpha}{2 \sin \varphi \cos(\varphi - \alpha)} \quad (3.9)$$

Before the theory can be used it is necessary to know the width of the shear zone Δs_1 in equation (3.6). Thus, an assumption must be made about the length to the width ratio of the shear zone (ie $t_1/\Delta s_1 \cdot \sin \varphi$). From the experimental work carried out by Kececioglu [34] and Nakayama [35] when machining a range of plain carbon steel (0.13% C to 0.38% C) at relatively high cutting speeds (eg from 600 up to 1000 fpm), and Enahoro [36], Palmer and Oxley [9] when machining a range of plain carbon steel (0.13% C to 0.58% C) at low cutting speeds (eg from 3 to 17 fpm) it was found that $t_1/\Delta s_1 \cdot \sin \varphi$ changed with cutting conditions (ie it increased with increase in cutting speed). However it was shown that the value lay in the range 6 to 14 for all the cutting conditions used.

For the purpose of the calculations carried out in the present work the ratio has been assumed to have a constant value of 10, which is the mean value of range of variation reported by the earlier workers.

It follows that if the angle θ in Figure 27 is the angle made between the resultant cutting force and the shear plane AB, it is then expressed [37] by the following expression

$$\tan \theta = \frac{P_A + P_B}{2 k_{AB}} \quad (3.10)$$

The value of the angle θ is also defined geometrically (Appendix I) in terms of the shear angle " φ ", the friction angle " λ " and the rake angle " α " that is:

$$\theta = \varphi + \lambda - \alpha \quad (3.11)$$

where:

- θ : angle made between the resultant cutting force and the shear plane AB
- φ : shear angle made between the shear plane AB and the direction of cutting
- λ : angle of friction along the tool chip interface

and

- α : the rake angle.

In order to determine the shear flow stress k_{AB} , uniaxial flow stress results are related to the plain strain machining conditions in the following way [38]:

$$\left. \begin{aligned} k_{AB} &= \sqrt{\frac{1}{3}} \sigma_1 \cdot \epsilon_{AB}^n \\ \epsilon_{AB} &= \sqrt{\frac{1}{3}} \cdot \gamma_{AB} \end{aligned} \right\} \quad (3.12)$$

where:

- k_{AB} : shear flow stress
- σ_1 and n : are constants in the stress-strain curve given in the following equation $\sigma = \sigma_1 \epsilon^n$ (where σ and ϵ the axial flow stress and natural strain)
- ϵ_{AB} : natural strain
- γ_{AB} : the shear strain.

The resulting cutting force transmitted by the shear plane AB and also transmitted by the tool-chip interface is given by the following expression demonstrated in Appendix I:

$$R = \frac{k_{AB} \cdot t_1 \cdot w}{\sin \varphi \cdot \cos \theta} \quad (3.13)$$

where:

- R : resulting cutting force transmitted by the shear plane AB and the tool-chip interface as shown in Figure 27
- k_{AB} : the shear flow stress
- w : the width of cut
- φ : the shear angle
- θ : the angle made by the direction of the cutting force and the shear plane AB.

Once the resultant cutting force is known, the following geometric force relations (Appendix I) can be obtained as shown in Figure 26:

$$\left. \begin{aligned} F_c &= R \cos(\lambda - \alpha) \\ F_t &= R \sin(\lambda - \alpha) \\ N &= R \cos \lambda \\ F_s &= R \cos \theta \end{aligned} \right\} \quad (3.14)$$

where:

F_c : is the cutting force against which work is done

F_t : is the thrust force (or feed force)

N : is the force normal to the shear plane AB

F_s : is the shearing force

and

R : is the resultant cutting force.

A typical example of cutting forces calculation using the semi-empirical model is shown in Appendix II.

CHAPTER 4

EXPERIMENTAL TECHNIQUE AND PROCEDURE

- 4.1 Cutting Tests
- 4.2 Cutting Tools
- 4.3 Workpiece Materials
- 4.4 Compression Tests
- 4.5 Preparation of the Workpiece
- 4.6 Cutting Conditions
- 4.7 Force Measurements
- 4.8 Chip Thickness Measurement
- 4.9 Quick-Stop Device
- 4.10 Measurements of the Primary and Secondary Shear Zone Widths and the Height of the Built-Up-Edge
- 4.11 The Scanning Electron Microscopy

4.1 CUTTING TESTS

The machining tests were carried out on a heavy duty tool-room lathe. The latter was a Churchill Denhams model SRIOV 22" swing centre lathe, equipped with an infinitely variable range of speeds between 15 and 2000 revs per minute; a 30Kw motor, and a choice of 54 longitudinal feed rates in the range 0.057 to 3.75mm per rev. The lathe is shown in Plate 1.

The cutting tests were carried out under orthogonal conditions. This was achieved by feeding the tool axially into the end of a tube rotating in the spindle of the lathe as shown schematically in Figure 30. The actual experimental set up is shown in Plate 2.

4.2 CUTTING TOOLS

The cutting tests were performed with cemented carbide cutting tools corresponding to the ISO P10 classification. A new tool was used for each cutting test. The duration of each test was short in order to ensure that tool wear effects were not important. The tools were designed to fit in the tool holder of a quick-stop device (the quick-stop device is detailed in Section 4.9) and had a flat at the top of their body for positioning and clamping in the tool holder.

4.3 WORKPIECE MATERIALS

Workpiece materials used to carry out the cutting tests in the present investigation were chosen to give continuous chip formation.

ONWOCHUKWA, O

Sheffield Hallam University Learning Centre	
Adsetts Centre Thesis Request Form	
Please complete one form per thesis and hand in at the information desk on L3 or L5.	
Your Name ONWOCHUKWA OGBONNA	Stack No. 3221
Learning Centre No. 21222153	Thesis Title Production of cutting tools for extrusion of aluminium
Date and time request submitted 13/09/05 ; 4.18pm	
Please complete the above in Block Capitals	
Please submit your request 45 minutes prior to collection time	
Date required 14/09	11:00
NB: Morning collection only during non-semester weeks	
You may view up to three theses at one time	
Please collect your thesis from the Issues and returns counter on Level 4.	

as Tahav
/Lahreche

The materials were:

- (i) a medium carbon steel "EN₈" in the normalized conditions,
 - (ii) an aluminium alloy,
- and
- (iii) a 70-30 brass.

Composition of these materials is shown in Table 1.

4.4 COMPRESSION TEST

Quasi-static compression tests performed in this investigation (in order to calculate the flow stress data) were carried out on a standard testing machine, type Denison universal testing machine model T428 with a capacity of 50 tons (this is shown in Plate 3).

In order to perform the quasi-static compression tests, a cylindrical specimen of 6×6mm in dimensions was prepared. The cylindrical specimen (Figure 31) used had plane end faces and was compressed between plane parallel platens that have been hardened and tempered and then ground and polished, as shown in Plate 4. The end faces of the cylindrical specimen were machined with shallow concentric grooves, that is to entrap lubricant. To minimise the frictional resistance at the interfaces (ie between the end surfaces of the compression specimen and the platens) a graphite in tallow was used as a lubricant. Results of the compression tests are dealt with in Chapter 5, Section 9.

Table 1 : Composition of workpieces materials used

%	EN ₈	Aluminium	70-30 Brass
C	0.38	-	-
Mg	-	0.67	<0.001
Si	0.19	0.60	<0.005
S	0.30	-	-
Cu	-	0.03	70.3
Mn	0.81	0.42	<0.001
Ni	0.16	-	0.001
Zn	-	-	29.65
P	0.014	-	-
Fe	Remainder	0.23	0.02
Cr	0.18	<0.01	-
Zr	-	0.03	-
Li	-	<0.001	-
Mo	0.05	-	-
V	0.01	-	-
Al	0.011	Remainder	-
Pb	-	-	0.18

4.5 PREPARATION OF THE WORKPIECES

Test workpieces were prepared as follows:

- For the medium carbon steel "EN₈", the tube was mounted between the chuck and a rotating centre as shown in Plate 5. The tube was then turned and bored to give a wall thickness of 3.20mm.

- For the aluminium alloy and the 70-30 brass, the workpieces materials were brought with tube wall thickness of 3.20 and 3.35mm respectively.

4.6 CUTTING CONDITIONS

Two groups of cutting test were carried out under dry cutting conditions.

- A. The first group of cutting tests were carried out under three sets of cutting conditions in order to investigate the effect of machining variables on cutting forces and chip thickness. The cutting conditions for the first group are given in Table 2.

- B. The second group of cutting tests were carried out to investigate the effect of machining variables on the dimensions of the primary and secondary deformation zones and on the height of the built-up-edge. The cutting conditions for the second group of cutting tests are given in Table 3.

Table 2 : Group A of cutting tests

Sets No.	Cutting Speed "V" (m/min)	Undeformed chip thickness "t ₁ " (mm)	Rake angle "α" (degree)
1	30 to 400	0.488 for EN ₈ and aluminium 0.244 for 70-30 brass	0
2	200	0.057 to 0.488	0
3	200	0.244	-10 to +25

The cutting tool in Group A of cutting tests was held in a tool holder mounted in and secured to the top of a three component dynamometer as shown in Plate 5.

Table 3 : Group B of cutting tests

Sets No.	Cutting speed "V" (m/min)	Undeformed chip thickness "t ₁ " (mm)	Rake angle "α" (degree)
1	30 to 150	0.488 for EN ₈ and aluminium 0.244 for 70-30 brass	0

The sets of cutting tests in Group B were carried out using a quick-stop device (the quick-stop device is detailed in Section 9). Experimental set up of Group B of cutting tests is shown in Plate 6.

4.7 FORCE MEASUREMENTS

The cutting force " F_c " and the feed force " F_t " acting on the tool during machining were measured using the three component piezo-electric dynamometer in conjunction with an amplifier connected to a platform recorder. The dynamometer used was a Kistler Quartz type 9257A capable of measuring vertical forces in the range 0-10KN and horizontal forces in the range -5 to +5KN with a resolution of 0.01N. The experimental set up for the force measurements is shown in Plate 1. Plate 7 shows the amplifier and the platform recorder used. Typical trace of the cutting forces " F_c " and " F_t " is shown in Plate 8.

4.8 CHIP THICKNESS MEASUREMENT

Measurements of the chip thickness were needed in order to determine the orientation of the shear plane. To measure the thickness of the chip a digimatic micrometer in conjunction with a digimatic mini-processor was used as shown in Plate 9. The digimatic micrometer was a 293 series Mitutoyo type. This digimatic micrometer is a high precision electronic measuring instrument with a resolution of 1 micron.

The digimatic mini-processor connected to the digimatic micrometer was a Mitutoyo 264 series - it is a functional data processing unit for the electronic digital instrument with an output function. Digimatic mini-processor was connected to an AC adaptor from which the power was supplied. Experimental set up is shown in Plate 10.

For each test condition ten measurements of the chip thickness were made at various points along the chip, and from these readings the mean chip thickness was determined.

4.9 QUICK-STOP DEVICE

In order to investigate the dimensions of the primary and secondary shear zones, and the height of the built-up-edge, the chip has to be attached to the machined surface. For this reason a quick-stop device was used as shown in Plate 11.

The quick-stop device used was an explosively driven bolt type (the bolt being provided by a human killer) and should not be used on speeds in excess of 465m/min [39]. The cutting tool was held in place by a tool holder resting on a shearing pin strong enough to withstand the cutting forces. The shearing pin was a silver steel material of 1%C high carbon steel. When the human killer gun is fired, the pressure builds up in the firing chamber accelerates the hammer which hits the top of the tool holder. Under the action of impact of the hammer the shear pin breaks, and releases the tool from the workpiece. The tool holder is then brought to a stop by plasticine. In order to allow for the feeding action of the tool, a cant angle is provided so that the tool retraction from the workpiece takes place at an angle to the machined surface, hence avoiding contact between the latter and the tool flank after the quick-stop has been operated. Plate 12 shows the quick-stop device used in the present investigation mounted on the cross-slide of the lathe and ready for machining operation. Plate 13 is a close up showing the tool holder, the machined surface, and the hole through which the hammer hits the tool holder.

Immediately after the quick-stop device tool had been operated, the spindle rotation and the feed were stopped and drops of oil were put on to the machined surface attached to it the chip root, that is to preserve it (them) from oxidation and corrosion for subsequent examination and measurements. Then, the machined surface attached with the chip root, was parted off and numbered using an etching pen for identification later on.

4.10 MEASUREMENT OF THE DIMENSIONS OF THE PRIMARY AND SECONDARY SHEAR ZONE WIDTHS AND THE HEIGHT OF THE BUILT-UP-EDGE

Microscopy was used to examine the dimensions of the primary and secondary shear zones and the built-up edge. The chip attached to the machined surface (left when the quick-stop device was used) was parted off in a specimen of the size one centimeter smaller than the size of the mount (1 inch in diameter).

Methods of mounting and polishing used were metallurgically standard.

During mounting, the chip root was carefully and properly orientated to give plane strain after polishing of 1mm in depth of the sample as shown in Figure 32.

To reveal structural details by the preferential attack of reagents on metal surfaces etching was done.

Etchants used in this present investigation were:

- A solution of 2% nital used for etching plain carbon steels "EN₈".

- The aluminium was etched with a solution of a hydrofluoric acid and mixed with water.
- A solution of also ferric chloride with water was used for etching the 70-30 brass.

After etching, specimens were washed with water and alcohol, then they were put in an electrosonic cleaner to take off all the spots of dirt from the specimens. Then the specimens were taken to a scanning electron microcopy (as detailed in Section 5.11) to examine and to take pictures of the chip root as shown in Plates 14 to 25. The angle at which the specimen was orientated in the scanning electron microscopy was taken zero degree.

Magnifications of the photographs (Plates 14 to 25) are stated under each photograph. From these photographs, dimensions of the primary and secondary shear zones, and the height of the built-up-edge were carried out by means of a ruler and their results are shown in Tables 14 to 17.

4.11 THE SCANNING ELECTRON MICROSCOPY

The scanning electron microscopy used in this investigation was of the type "PSEM500" shown in Plate 26. The PSEM is designed to combine high performance versatility and ease of operation with the special feature that full quantity of measurement could be made. It offers greater potential than a conventional optical microscope, being capable of resolving topographical details of less than 300\AA with a depth of focus 500 times that of an optical system.

The basic principles of its operations are shown in Figure 33. Electrons are generated at a hot tungsten filament and accelerated through an anode by means of a 1 to 50KV potential with respect to the filament. The magnetic condenser lenses reduce the electron beam diameter until a probe of 100 to 200Å diameter is formed on the specimen surface. This beam of electrons generates a wide variety of signals when it interacts with a solid metal surface. These signals include back-scattered electrons (high energy), secondary electrons (low energy), photons and x-rays all of which are produced by the scattering of the incident electrons by the atoms in the specimens. The deflection coils are connected to a scan generator which causes the incident beam to be scanned over the specimen in an x-y pattern. The scanning generator is also connected, in series, to the deflection coils of the cathode ray tube monitor so that the beam in the microscope column and the beam in the cathode ray tube are scanning the specimen and screen respectively, in a synchronized manner. Thus, there is one-to-one relationship between the position of the electron beam on the specimen and that of the spot on the cathode ray tube. Intensity variation of the spot on the cathode ray tube is controlled by the strength of the signal reaching the control grid. This signal, which is generated by the electron detection unit, is a direct function of the secondary electron emission developed through the interaction of the primary electron probe and the specimen. It is the spot intensity variation that forms the image on the cathode ray tube screen.

Once the chip root and the machined surface appear through the screen of the SEM and, after focussing, a picture is taken with the desired magnification by a camera incorporated to the SEM used in this investigation.

CHAPTER 5

RESULTS

- 5.1 Variation of the Cutting Forces with Change in Cutting Speed
- 5.2 Variation of the Chip Thickness Ratio with Change in Cutting Speed
- 5.3 Variation of Cutting Forces with a Change in the Undeformed Chip Thickness
- 5.4 Variation of the Chip Thickness Ratio with the Undeformed Chip Thickness
- 5.5 Variation of Cutting Forces with a Change in Rake Angle
- 5.6 Variation of the Chip Thickness Ratio with a Change in Rake Angle
- 5.7 Built-Up-Edge Height and Built-Up-Edge Layer Results
- 5.8 Deformation Zone Measurements
- 5.9 Compression Test Results

5.1 VARIATION OF THE CUTTING FORCES WITH CHANGE IN CUTTING SPEED

The variation of the vertical and horizontal cutting forces with change in cutting speed is shown in graphical form in Figures 34, 35 and 36 for EN₈, aluminium and 70-30 brass respectively. The results of the cutting forces with the change of the cutting speed are also given in tabulated form in Appendix III.

5.2 VARIATION OF THE CHIP THICKNESS RATIO WITH CUTTING SPEED

The variation of the cutting ratio with change in cutting speed for EN₈, aluminium and 70-30 brass is shown in Figure 37.

5.3 VARIATION OF THE CUTTING FORCES WITH UNDEFORMED CHIP THICKNESS

The variation of the vertical and horizontal cutting forces with change in the undeformed chip thickness in cutting EN₈, aluminium and 70-30 brass, is shown in graphical form in Figures 38, 39 and 40 respectively. The results of the cutting forces with the change of the undeformed chip thickness are given in tabulated form in Appendix III.

5.4 VARIATION OF THE CHIP THICKNESS RATIO WITH THE UNDEFORMED CHIP THICKNESS

The cutting ratio variation with the change in the undeformed chip thickness is given in Figure 41 for EN₈, aluminium and the 70-30 brass.

5.5 VARIATION OF CUTTING FORCES WITH A CHANGE IN THE RAKE ANGLE

Vertical and horizontal cutting force variation with change in the rake angle is shown in Figures 42, 43 and 44 for EN₈, aluminium and 70-30 brass respectively. Results of the cutting forces with variation in rake angle are given in tabulated form in Appendix III.

5.6 VARIATION OF THE CHIP THICKNESS RATIO WITH A CHANGE IN RAKE ANGLE

The variation of the cutting ratio with a change in rake angle for EN₈, aluminium and the 70-30 brass is shown in Figure 45.

5.7 BUILT-UP-EDGE HEIGHT AND BUILT-UP-LAYER RESULTS

Results of the built-up-edge and built-up layer with variation in cutting speed are given in Table 19.

Built-up-edge height is shown in Plates 14 and 15, and the built-up-layer is shown in Plates 16 and 17.

5.8 DEFORMATION ZONE MEASUREMENTS

Measurements of the primary shear zone width and the secondary shear zone are presented in Tables 20 and 21. Plates 18 to 25 show the variation of the primary shear zone width and the secondary shear zone with variation of the cutting speed.

5.9 COMPRESSION TEST RESULTS

Results of the compression test carried out in this investigation are presented in graphical form. From the compression results obtained, true stress-strain graphs are shown in Figures 46, 47 and 48 for EN₈, aluminium and the 70-30 brass. The value of σ_1 in equation $\sigma = \sigma_1 \epsilon^n$ is obtained as the engineering strain $\epsilon = 1$, and is shown in the Figures 46, 47 and 48

- for EN₈, $\sigma_1 = 940\text{MN.m}^{-2}$
- for aluminium, $\sigma_1 = 360\text{MN.m}^{-2}$

and

- for the 70-30 Brass, $\sigma_1 = 590\text{MN.m}^{-2}$

The value of the strain hardening "n" is obtained from:

$$\text{Log } \sigma = \text{Log } \sigma_1 + n \log \epsilon$$

thus
$$n = \frac{10 \log(\sigma - \sigma_1)}{\log \epsilon}.$$

CHAPTER 6

DISCUSSION

- 6.1 Introduction
- 6.2 Variation of Cutting Forces with Cutting Speed
- 6.3 Variation of the Chip Thickness Ratio with Cutting Speed
- 6.4 Variation of Cutting Forces with the Change in the Undeformed Chip Thickness
- 6.5 Variation of Cutting Forces with Change in Rake Angle
- 6.6 Assumptions Made in the Semi-Empirical Model Used in Chapter 4

6.1 INTRODUCTION

The prediction of the cutting forces, as described in Chapter 4, was carried out for given values of

- (i) cutting speed
 - (ii) undeformed chip thickness
- and
- (iii) rake angle.

The predicted cutting forces were determined using the semi-empirical model for three workpiece materials, namely:

- EN₈, medium carbon steel
- Aluminium
- 70-30 Brass

and were then compared to the experimental results obtained from machining tests as described in Chapter 5.

6.2 VARIATION OF CUTTING FORCES WITH CUTTING SPEED

The predicted and experimentally measured cutting forces when machining the EN₈ and the aluminium are illustrated in Figures 34 and 35 respectively. From these figures it is shown that both the predicted and the experimentally obtained results have similar trends (ie the predicted and experimentally measured cutting forces decrease with an increase in cutting speed) but the predicted results are much

higher in magnitude than those obtained experimentally.

The fact of the decrease in cutting forces with an increase in cutting speed confirms results obtained by previous workers [10 to 13] and this fact is mainly due to a rise in cutting temperature which increases the ductility of the workpiece material.

When machining the 70-30 brass, it is shown that the experimentally measured cutting forces (Figure 36) are independent of cutting speed. The independence of cutting force and cutting speed when machining 70-30 brass was also shown by J E Williams [40]. The predicted results with 70-30 brass are shown to decrease with an increase in cutting speed and are much lower in magnitude than those obtained experimentally.

6.3 VARIATION OF THE CHIP THICKNESS RATIO WITH CUTTING SPEED

Figure 37 shows the variation of the chip thickness ratio with change in cutting speed. The chip thickness ratio (Figure 37) increases with an increase in cutting speed. This increase of the chip thickness is due to the decrease in chip thickness (ie $r_c = t_1/t_2$) which occurs as the cutting speed is increased as shown in Table 16.

6.4 VARIATION OF THE CUTTING FORCES WITH THE UNDEFORMED CHIP THICKNESS

Predicted and experimentally measured cutting forces with a change in the undeformed chip thickness are illustrated in Figures 38, 39 and 40 for EN₈, aluminium and 70-30 brass. Experimentally measured cutting forces in all cases increase with an increase in the undeformed chip thickness. The increase in experimental cutting forces is mainly due to the increase in chip thickness which occurs as the undeformed chip thickness is increased as shown in Figure 4. and also shown in Table 17. This fact of the increased cutting forces with an increase in the undeformed chip thickness was also shown previously [10 to 13].

Predicted cutting forces with the change in the undeformed chip thickness for EN₈ and aluminium (Figures 38 and 39) show the same trend as the experimentally measured cutting forces.

For the 70-30 brass, predicted results for the vertical cutting force show the same trend with results experimentally obtained. However, predicted results obtained for the horizontal cutting force show a different trend with the results experimentally obtained for the horizontal cutting force shown in Figure 40. This led to a verification of the assumptions made to the semi-empirical model used in this investigation.

6.5 VARIATION OF CUTTING FORCES WITH RAKE ANGLE

The effect of rake angle on the vertical and horizontal cutting forces is shown in Figures 42, 43 and 44. It is clear that both forces decrease with an increase in rake angle. Previous workers [36 and 37] had also shown this fact.

The decrease in cutting forces with an increase in rake angle is due to the decrease in chip thickness which in its turn increases the chip ratio as shown in Figure 45. A decrease in chip thickness is due to lower friction between the rake face of the tool and the chip, thus a lower force is obtained.

6.6 ASSUMPTIONS MADE IN THE SEMI-EMPIRICAL MODEL USED IN CHAPTER .

As discussed before in Chapter ., the semi-empirical model used in this investigation makes the following assumptions:

- (i) the length to width of the primary shear zone " s_z " (which was found to vary in the range of 6 to 14 [35 to 37] is assumed to have a constant value of 10) where:

$$s_z = \frac{t_1}{\Delta s_1 \sin \varphi} = 10$$

the value 10 being the mean of range (6 to 14).

From the foregoing comparisons of the predicted and experimentally obtained results for the cutting forces, it was shown that there is a poor agreement between the prediction of cutting forces and forces obtained from experiments.

This led to an examination of the two major assumptions made in the semi-empirical model of machining, namely that the primary shear zone had a constant length to width ratio, and that the shear flow stress was constant.

It has been pointed out in Section 4.5 that earlier workers found the length to width ratio of the shear zone to lie within the range 6 to 14; since " s_z " has an effect on the hydrostatic stress " p_B " (equation 3.6), the predicted values of vertical and horizontal cutting force were therefore recalculated and the results are shown in Figures 49 to 52.

The hydrostatic stress " p_B " affects the angle " θ " (equation 3.10) which has a strong influence on the resultant cutting force " R " calculated from equation 3.13.

In equation 3.6, the hydrostatic stress " p_B " shown to decrease with an increase in the ratio " s_z " and vis versa.

Therefore, in order to decrease the magnitude of the predicted cutting forces with the case of the EN₈ and the aluminium shown in Figures 49 and 50, the ratio " s_z " has then taken the maximum value 14 of the range 6 to 14. From 49 and 51 it is shown that the vertical cutting force found from prediction is similar to that measured experimentally. However, the magnitude of the calculated horizontal cutting force is much higher than the measured one.

In the case of the 70-30 brass the ratio " s_z " is taking the minimum value 6 of the range (6 to 14), that is to increase the value of the predicted cutting forces. From Figures 51 and 52 it is shown that there is an agreement in magnitude of the predicted and measured vertical cutting force. Figure 52 shows that there is

no agreement between the predicted and measured horizontal cutting force.

From the above discussion and changes in the values of the ratio, it is shown from Figures 49 to 52 that the horizontal cutting force found from the prediction has different values than the measured ones.

The horizontal cutting force is calculated from the angle of friction " λ " (equation 3.14) which is affected by the hydrostatic stress " p_B ", since " λ " is calculated (equation 3.11) from the angle " θ ".

In order to improve the angle of friction " λ ", the hydrostatic stress has to be improved. The hydrostatic stress " p_B " is not only affected by the ratio " s_z ", it is also affected by the change in shear flow stress " Δk " (equation 3.7). If " Δk " is small the hydrostatic stress " p_B " calculated from equation 3.6 has a relatively high value and this means that the predicted cutting forces also have high values as is the case with the EN₈ and aluminium (Figures 49 and 50).

In the case of the 70-30 brass, the change in shear flow stress " Δk " is greater than with both EN₈ and aluminium (shown in Figure 53 and also shown in Tables 5 to 15), thus the predicted cutting force are lower than the measured ones.

Therefore the assumption of the ratio " s_z " is not the only reason for the poor agreement between predicted and experimental results.

The other assumption which is made in the semi-empirical machining model is that flow stress is constant, no allowance is made for the effect of temperature and strain rate in machining which could also affect the predicted cutting forces (as the

case with the change in the shear flow stress " Δk " on the hydrostatic stress " p_B ").

It is well established that cutting temperatures and strain rates in machining are both very high. Cutting temperatures and strain rates both have a considerable effect on the flow stress [41 to 44]. The flow stress data which allow for the effect of temperature and strain rate encountered in machining are limited. The only extensive flow stress data known is for plain carbon steel. The EN₈ is one class of plain carbon steel, thus a model which incorporates the effects of temperature and strain rate on flow stress is then described in the following chapter.

CHAPTER 7

MACHINING THEORY ALLOWING FOR STRAIN-RATE AND TEMPERATURE EFFECTS

- 7.1 Introduction
- 7.2 Analysis
- 7.3 Predicted Results

7.1 INTRODUCTION

In the semi-empirical model of machining used in Chapter 3, the chip formation process was represented by a single velocity discontinuity where the parallel-sided plastic zone for primary shear is similar to a thin shear plane [45 to 47]. It has also been mentioned that the semi-empirical model of machining the process of deformation is mostly taken into account in the primary shear zone. For this reason the mechanical behaviour was taken to be similar to that in using a simple compression test, where the strain rate and the temperature effects are not considered important. However, once the material has been sheared through the primary shear zone to form a chip flowing parallel to the rake face of the tool, a secondary shearing action is generally observed at the chip-tool interface. This process has been confirmed by metallographic observations [45 to 48]. By considering the two deformation zones in this analysis it is found that the flow stress of the material being machined is a major consideration (as is discussed earlier in Chapter 2).

7.2 ANALYSIS

The model of the chip formation used in this analysis is shown in Figure 54; plane strain, steady-state conditions are again assumed to apply (orthogonal machining) as shown in Figure 30).

The plane AB (Figure 54) near the centre of the chip formation zone, which is found from the same geometric construction as for the shear plane in the shear plane model of chip formation [48] and the tool-chip interface, are both assumed to be directions of maximum shear stress and maximum shear strain rate.

The basis of the theory is to analyse the stress distribution along the plane AB and along the tool-chip interface in terms of the shear angle " φ " and work material properties. The shear angle is found from equation 3.1. Once " φ " is known then the chip thickness and the various components of force are determined from the following geometric relations (as shown in Appendix I).

$$\begin{aligned}
 t_2 &= t_1 \cos(\varphi-\alpha)/\sin \varphi \\
 F_c &= R \cos(\lambda-\alpha) \\
 F_t &= R \cos(\lambda-\alpha) \\
 F_t &= R \cos(\lambda-\alpha) \\
 F &= R \sin \lambda \\
 N &= R \cos \lambda \\
 R &= \frac{F_s}{\cos \theta} = \frac{k_{AB} \cdot t_1 \cdot w}{\sin \varphi \cos \theta}
 \end{aligned}
 \tag{7.1}$$

where:

- t_1 : is the undeformed chip thickness,
 - w : is the width of cut
 - k_{AB} : is the shear flow stress along AB
- and the forces and angles are as defined before.

By starting at the free surface just ahead of A and applying the appropriate stress equilibrium equation along AB it can be shown that for $0 < \varphi < \pi/4$, the angle θ made by the resultant "R" with AB is given by

$$\tan \theta = 1 + 2 \left[\frac{\pi}{4} - \varphi \right] - Cn \tag{7.2}$$

where:

- C : is the constant in the empirical strain rate relation (Stevenson and Oxley [46])

$$\dot{\gamma}_{AB} = CV_s/L \quad (7.3)$$

where:

$\dot{\gamma}_{AB}$: is the maximum shear strain rate at AB

V_s : (Figure 54) is the shear velocity

L : is the length of AB

and

n : is the strain-hardening index in the empirical stress-strain relation

$$\sigma = \sigma_1 \epsilon^n \quad (7.4)$$

where:

σ and ϵ : are the axial flow stress and strain

and

σ_1 and n : are "constants" which define the stress-strain curve for given values of strain rate and temperature.

From geometry of Figure 54, the angle θ can also be expressed in terms of another angle by the equation:

$$\theta = \varphi + \lambda - \alpha \quad (7.5)$$

The temperature at AB which is needed together with the strain rate and strain at AB to determine " k_{AB} " and " n " is found from the equation

$$T_{AB} = T_w + \eta \left| \frac{1-\beta}{\rho St_1 \cdot w} \cdot \frac{F_s \cos \alpha}{\cos(\varphi-\alpha)} \right| \quad (7.6)$$

where:

T_w : is the initial work temperature

F_s : is the shear force along AB

$\eta(0 < \eta < 1)$: is a factor which allows for the fact that not all of the plastic work of chip formation has occurred at AB

ρ and S : are the density and specific heat of the work which is estimated from the following empirical equations based on a compilation of experimental data made by Boothroyd (1963)

[22]

$$\begin{aligned} \beta &= 0.5 - 0.34 \lg(R_T \tan \varphi) \text{ for } 0.04 < R_T \tan \varphi \\ \beta &= 0.3 - 0.15 \lg(R_T \tan \varphi) \text{ for } R_T \tan \varphi > 10 \end{aligned} \quad (7.7)$$

with R_T a non-dimensional thermal number given by

$$R_T = \rho S v_1 / k \quad (7.8)$$

where

k : is the thermal conductivity of the work material. The limits $0 < \beta < 1$ are also imposed.

The strain at AB is given by:

$$\gamma_{AB} = \frac{\frac{1}{2} \cos \alpha}{\sin \varphi \cos(\varphi - \alpha)} \quad (7.9)$$

The average temperature at the tool-chip interface from which the average shear flow stress at the interface is determined is taken as:

$$T_{int} = T_w + \frac{1-\beta}{\rho S t_1 \cdot w} \cdot \frac{F_s \cdot \cos \alpha}{\cos(\varphi - \alpha)} + \psi T_M \quad (7.10)$$

where:

T_M : is the maximum temperature rise in the chip and the factor ψ ($0 < \psi < 1$) allows for " T_{int} " being the average value. Using numerical methods Boothroyd (1963) [22] has calculated " T_M " by assuming a rectangular plastic zone (heat source) at the tool chip interface and has shown that his results agree well with experimentally measured temperatures. [49].

If the thickness of the secondary plastic zone (as it is defined in Chapter 2 Section 4) is taken " δt_2 ", where " δ " is the ratio of this thickness to the chip thickness " t_2 ", then Boothroyd's results can be represented by the equation

$$\lg \left[\frac{T_M}{T_C} \right] = 0.06 - 0.1958 \left[\frac{R_T \cdot t_2}{h} \right]^{\frac{1}{2}} + 0.5 \lg \left[\frac{R_T t_2}{h} \right] \quad (7.11)$$

where:

T_C : is the average temperature rise in the chip, given by the following equation:

$$T_C = F \cdot \sin \varphi / \rho \cdot S \cdot t_1 \cdot w \cos(\varphi - \alpha) \quad (7.12)$$

and h is the tool-chip contact length which can be calculated from the equation:

$$h = \frac{t_1 \cdot \cos \varphi}{\cos \lambda \sin \varphi} \left[1 + \frac{c \cdot n}{3 [1 + 2 \pi/4 - \varphi] - c \cdot n} \right] \quad (7.13)$$

The above equation is derived by taking moments about B of the normal stresses on AB (shear plane) to find the position of "R" and then assuming that the normal stress distribution at the tool face is uniform so that "R" intercepts the tool at a distance $1/2h$ from B. The maximum shear strain rate at the tool-chip interface, which is also needed in determining the shear flow stress is found from the equation

$$\dot{\gamma}_{int} = V_c / \delta t_2 \quad (7.14)$$

where:

V : is the rigid velocity of the chip as shown in Figure 54.

This implies that the sliding velocity at the cutting face is zero, that is, that seizure has occurred in the tool-chip contact region. This is consistent with the findings of Trent (1977) [50] who has shown, using optical and electron microscopy to examine the chip and tool sections, that the contracting surfaces are, for most practical machining conditions, interlocked with adhering metal penetrating all irregularities in the tool surface. However, for steady-state conditions as assumed in the previous analysis as well as in this method of analysis, the material must

leave the tool-chip interface plastic zone (ie secondary shear zone) with a velocity consistent with the rigid body motion of chip and the sliding velocity cannot be zero over much of this region. It can, however, be much smaller than the chip velocity over much of this region as can be deduced [16] from using a slip line field similar to that suggested by Roth and Oxley (1972) [19]. With fields of this kind the sliding velocity increases in moving along the cutting face away from the cutting edge B (Figure 54) and can have very low values, approaching zero value, while the velocities at the plastic zone boundary are still consistent with the rigid body motion of a rotating (curled) chip. The associated flow shows similar features to those resulting from seizure with, in particular, the layer of chip material in contact with the tool greatly swept back (retarded) relative to the rest of the chip. Therefore, although equation (7.14) will overestimate $\dot{\gamma}_{int}$ and the cutting face will not be exactly a direction of maximum shear strain rate, and hence maximum shear stress, because there is a direct strain rate in this direction, the differences will usually be smaller and can for the purposes of the analysis be neglected.

The above equations used in this analysis are now sufficient to calculate cutting forces and temperatures for given cutting conditions, so long as the appropriate work material properties and the values of "C" in (7.2) and (7.3), the value of " δ " in (7.11) and (7.14) are known. The resolved shear stress at the tool-chip interface is calculated in this method of analysis from the resultant cutting force obtained from the stresses on AB, that is

$$\tau_{int} = F/(h.w) \quad (7.15)$$

In this theory the values of "C" and " δ " in eqations (7.3) and (7.14) respectively have been assumed to remain constant over a range of cutting conditions for plain

carbon steel have been taken, on the basis of experimental results [30], as 5.9 and 0.05 respectively. To determine "C", Oxley and Hastings (1976) [37] considered the stress boundary condition at the cutting edge B which had previously been neglected.

For a uniform normal stress at the interface the average normal stress is given

$$\sigma_N = N/h.w \quad (7.16)$$

The above stress can also be found from the stress boundary condition at B found by working from A along AB. If AB turns through the angle $(\varphi-\alpha)$ (in negligible distance) to meet the interface at right angles, as it must do if the interface is assumed to be a direction of maximum shear stress, then it can be shown that

$$\sigma'_N/k_{AB} = 1 + \frac{\pi}{2} - 2\alpha - 2C.n \quad (7.17)$$

and the value of "C" can be determined from the condition that σ_N and σ'_N must be equal. It has been shown by Oxley and Hastings [37] that the values of "C" and "δ" predicted in this way are in good agreement with experimental results.

7.3 PREDICTED RESULTS FROM THE MACHINING MODEL ALLOWING FOR STRAIN RATE AND TEMPERATURE EFFECTS

In making predictions (of the method of analysis allowing in the machining model for the strain rate and temperature effects) the flow stress and thermal properties of the work material had to be known. The flow stress properties were represented by the values of " σ_1 " and "n" which define the stress-strain curve in (7.4) and which were taken to be functions of a velocity modified temperature " T_{mod} " expressed as shown in Figure 55.

$$T_{\text{mod}} = T(1 - \nu \lg \dot{\epsilon} / \epsilon_0) \quad (7.18)$$

where:

- $T(k)$: is the temperature
 $\dot{\epsilon}$: is the direct strain rate and
 ν and ϵ_0 : are constants.

Figure 56 gives σ_1 and n values corresponding to the chemical composition (ie 0.41%C) of the work material being used with the present theory (with " T_{mod} " calculated taking $\nu = 0.09$ and $\epsilon_0 = 1s^{-1}$). These were obtained from the results of high speed compression tests carried out over a wide range of temperatures done by Oyane et al (1967) [51]. The specific heat " S " and thermal conductivity k needed in the calculations were obtained from the experimental results of Woolman and Mottram [52]

$$S/(\tau.Kg^{-1}.K^{-1}) = 420 + 0.504 T/^{\circ}C \quad (7.19)$$

and

$$K/(Wm^{-1}2 K^{-1}) = 52.61 - 0.0281 T/^{\circ}C \quad (7.20)$$

The density ρ of the work material is assumed constant and taken as 7862 Kg/m³.

In making calculations (method II) for given values of cutting speed, undeformed chip thickness and rake angle, the following procedure is used. Initial work temperature " T_w " takes the value of $T_w = 20^{\circ}C$. For a given value " δ " (the equilibrium $\tau_{\text{int}} = K_{\text{chip}}$) values of " θ " are found for a range of values of " C " [53] and the required value " C " is determined from the condition $\sigma_N = \sigma_N'$. This is repeated for different values of " δ " and the final solution of cutting forces is taken at the values of which maximises " T_{mod} " and thus minimises " K_{chip} ".

In the calculation described here the temperature factors η and ψ in equations (7.6) and (7.10) were both taken as 0.7 [53] based on the finite element determinations of temperature by Tay et al [54].

Predicted results, covering the same range of conditions as used in the experiments for the cutting forces are represented by the solid lines in Figures 56, 57 and 58. Predicted results taken from this theory are also shown in Tables 29, 30 and 31 in Appendix III.

CHAPTER 8

CONCLUSIONS AND RECOMMENDATIONS FOR FUTURE WORK

- 8.1 Conclusions
- 8.2 Recommendations for Future Work

8.1 CONCLUSIONS

1. A semi-empirical model of machining has been used to predict the cutting forces which exist when machining medium carbon steel, aluminium and 70-30 brass. The effects of cutting speed, undeformed chip thickness and rake angle have been examined. Predicted and experimentally obtained values of cutting force show relatively poor correlation.
2. The length to width ratio of the primary shear zone, " s_z ", was found to differ with each workpiece material, but was shown to exert only a small effect on the magnitude of the predicted cutting forces.
3. The change in the shear flow stress in the primary deformation zone " Δk " exerts a strong influence on the magnitude of the hydrostatic stress " p_B " which, in turn, has a major effect on the cutting forces predicted by the semi-empirical model.
4. A modified model of machining which allows for the effects of strain-rate and temperature on the flow stress of the workpiece material has been used to predict cutting forces. This method (Chapter 7) produced close accord between experimental and predicted results, but due to the lack of data for other materials, was restricted to medium carbon steel.
5. The absence of high strain-rate data for aluminium and brass, and restriction of the velocity-modified temperature approach to low and medium carbon steels, places a severe restriction on the semi-empirical method.

8.2 RECOMMENDATIONS FOR FUTURE WORK

1. In order to overcome the restrictions of the machining model discussed in Conclusion 5 above, it is proposed that the flow stress properties of a range of workpiece materials can be obtained at strain rates similar to those occurring during machining (ie 10^4 - 10^6sec^{-1}).
2. Data of the required type could be obtained using a ballistics rig of the kind available in the Department of Mechanical and Production Engineering, Sheffield City Polytechnic.
3. The effect of temperatures up to $\approx 800^\circ\text{C}$ on the flow stress properties should also be investigated.

REFERENCES

1. Kronenburg, M: "Machining Science and Application": Pergamon Press, 1966.
2. Earnist, H: "Physics of Metal Cutting": Trans A S Metals, Vol 1, p1, 1958.
3. Nakayama, K: "Studies on the mechanism of Metal Cutting": Bull Fac Engng Yokohama, Natn University, Vol 7, p1, 1958.
4. Shwers, F: "Neue Untersuchungen Zur Schnittheorie Und Bearbeitbarkeit": Stahl Und Eisen, Vol 16, 1931.
5. Trent, E M: "Metal Cutting": Butterworths and Co (Publishers) Ltd, 1977.
6. Iwata, K and Ueda, K: "The Significance of Dynamic Crack Behaviour in Chip Formation": Annals of the CIRP, Vol 25 (No 1), 1976.
7. Hill, R: "The Mechanics of Machining : A New Approach": J of the Mechanics and Physics of Solids, 3, p47, 1954.
8. Okushima, K and Hitomi, K: "An Analysis of the Mechanics of Orthogonal Cutting and its Application to Discontinuous Chip Formation": Trans Amer Soc Mech Engrs, Series B, J of Engrs for Ind 83, p545, 1961.
9. Kokayashi, S and Thomsen, E G: "Some Observations of the Shearing Process in Metal Cutting": Trans Amer Soc Mech Eng, Series B, J of Eng for Ind, 81, p251, 1959.
10. Palmer, W B and Oxley, P L B: "Mechanics of Orthogonal Machining": Prod Inst Mech Engrs, 173, p623, 1959.
11. Connolly, R and Rubenstein, C: "The Mechanics of Continuous Chip Formation in Orthogonal Cutting": Int J Mech Tool Des Res, Vol 8, p159, Pergamon Press, 1968.
12. Form, G W and Beglinger, H: "Fundamental Considerations in Mechanical Chip Formation": Annals of the CIRP, Vol 18, p153, 1970.
13. Merchant, M E: "'Minimum Energy' Type of Solution for the Determination of the Shear Plane Angle": J Appl Phys, Vol 16, p267, 1945.
14. Zorev, N N: "Interrelation Between Shear Process Occurring Along Tool Face and on Shear Plane in Metal Cutting": Int Res Prod Engrg, p42, 1964.

15. Stevenson, G and Oxley, P L B: "An Experimental Investigation of the Influence of Speed and Scale on the Strain Rate in a Zone of Intense Plastic Deformation": Inst of Mech, Vol 184, p561, 1970.
16. Wright, P K and Robinson, J L: "Material Behaviour in Deformation Zones of Machining Operation": Metals Society, Vol 3, p240, 1977.
17. Palmer, W B and Oxley, P L B: "Mechanics of Orthogonal Machining": Proc Instn Int Mach Mech Engrs, Vol 173, p623, 1959.
18. Enahoro, H E and Oxley, P L B: "An Investigation of the Transition From Continuous To Discontinuous Chip in Orthogonal Machining": Int J Mech Sci, Vol 3, p145, 1961.
19. Roth, R N and Oxley, P L B: "Slip-Line Field Analysis for Orthogonal Machining Based Upon Experimental Field": J Mech Engng Sci, Vol 14, p85, 1972.
20. Armarego, E J A and Brown, R H: "On the Size Effect in Metal Cutting": Int J of Prod Res, Vol 1, 1962.
21. Trent, E M: "Metal Cutting": Butterworths and Co (Publishers) Ltd, 1977.
22. Boothroyd, G: "Temperatures in Orthogonal Metal Cutting": Proc IME, Vol 177, 1963.
23. Weiner, J H: "Shear Plane Temperature Distribution in Orthogonal Cutting": Trans Am Soc Mech Engrs, Vol 77, p133, 1955.
24. Barrow, G: "A Review of Experimental and Theoretical Techniques for Assessing Cutting Temperature": Annals of the CIRP, Vol 22 (No 2), p203, 1973.
25. Veenstra, P C, Bus, C and Staus, A P A G: "Cutting Tool Temperature - An Analysis of Experimental Results": CIRP Conference 1966.
26. Rapier, A C: "A Theoretical Investigation of the Temperature Distribution in the Metal Cutting Process": Br J Appl Phys, Vol 5 (No 11), p400, 1958.
27. Nakayama, K: "Temperature Rise of Workpiece During Metal Cutting": Bull Fac Engrg, Yokohama Nat Univ (Japan), Vol 5, p1, 1958.
28. Murarka, P D, Barrow, G and Hinduja, S: "Influence of the Process Variables on the Temperature Distribution in Orthogonal Machining Using the Finite Element Method": Int J Mech Engng Sci, Vol 21, p445, Peragamon Press, 1979.
29. Hashmi, M S J: "Apparent Strain Analysis of Orthogonal Machining Allowing for the Effects of Strain Rate and Temperature": Proc Inst Mech Engrs, Vol 194, p187, 1980.

30. Oxley, P L B: "A Mechanics of Machining Approach to Assessing Machinability": Proc 22nd Int MTDR Conf, p279, 1981.
31. Okushima, K and Hitomi, K: "An Analysis of the Mechanics of Orthogonal Cutting and Its Application to Discontinuous Chip Formation": Trans Amer Soc Mech Engrs, Series B, J of Engng for Ind, Vol 83, p545, 1961.
32. Rowe, G W: "Element of Metalworking Theory": IBM Press Romon, 1979.
33. Wagoner, R H: "Measurement and Analysis of Plain-Strain Work Hardening": Metall Trans Amer, Vol 11A, p165, 1980.
34. Kececioglu, D: "Shear Strain-Rate in Orthogonal Cutting and Its Effects on Shear Flow Stress": Trans ASME, Vol 80, p149, 1958.
35. Nakayama, K: "Study on the Mechanism of Metal Cutting": Bull Fac Engng Yokohama Natn University, Vol 8, 1959.
36. Enahoro, H E: "Flow Along Tool-Chip Interface in Orthogonal Metal Cutting": J Mech Engng Sci, Vol 8 (No 1), 1966.
37. Oxley, P L B and Hastings, W F: "Minimum Work as a Possible Criterion for Determining the Frictional Conditions at the Tool/Chip Interface in Machining": J Mech Engng Sci, Vol 282, p565, 1976.
38. Boothroyd, G: "Fundamentals of Metal Machining and Machine Tools": MacGraw Hill Book Company, 1975.
39. Crampin, R A and Gillibrand, D: "The Calibration of a Quick-Stop Device": Project, Dept of Mech and Prod Engng, Sheffield City Polytechnic, 1983.
40. Williams, J E: "Experimental Measurement of Cutting Forces and Speeds": Part I, Tool Engr, Vol 27 (No 4), p51, 1951.
41. Shaw, M C: "Metal Cutting Principle": 1984.
42. Yong, H and Wagoner, R H: "An Analytical Investigation of Deformation Induced Heating in Tensile Testing": Int J Mech Sci, Vol 29 (No 3), p179, 1987.
43. Lin, M R and Wagoner, R H: "Effect of Temperature, Strain and Strain Rate on the Tensile Flow Stress of IF Steel and Stainless Steel Type 330": Sci Metall, Vol 20, p143, 1986.
44. Granzow, W G: "The Influence of Tooling Temperature on the Formality of Stainless Steel Sheets": Formality of Metallic Materials - 2000 AD ASTM, p137, 1982.

45. Kobayashi, S and Thomsen, G G: "Some Observations of the Shearing Process in Metal Cutting", Trans Amer Soc Mech Eng, Series B, J of Eng for Ind, Vol 81, p71, 1969.
46. Oxley, P L B and Stevenson, M G: "Measuring Stress/Strain Properties of Very High Strain Rates Using a Machining Test": J of Inst of Metals, Vol 95, p308, 1967.
47. Richardson, R N, Hastings, M G and Oxley, P L B: "Predicting Tool Life and Built-Up Edge Occurrence when Machining Plain Carbon Steel with High Speed Steel Cutting Tools": Australian Conference on Manufacturing Engineering, p47, 1977.
48. Hastings, W F, Mathew, P and Oxley, P L B: "A Machining Theory for Predicting Chip Geometry, Cutting Forces, etc From Work Material Properties and Cutting Conditions": Proc R Soc Cond A371, 1980.
49. Schmidt, A O, Boston, O W and Gilbert, W W: "Measurements of Temperatures in Metal Cutting": Trans Amer Soc Mech Engrs, Vol 68, p208, 1969.
50. Trent, E M: "Metal Cutting": Butterworths, 1977.
51. Oyane, M, Takashima, F, Osakada, K and Tanaka, H: 10th Japanese Congress on Testing Materials, p72, 1967.
52. Woolman, J and Mottram, R A: "The Mechanical and Physical Properties of the British Standard in Steels": British Iron and Steels Research Association, Pergamon Press, 1964.
53. Hastings, W F, Mathew, P, Oxley, P L B and Taylor, J: "Estimated Cutting Temperatures - Their Use as a Prediction of Tool Performance When Machining Plain Carbon Steels": Proc MTDR Conf, p313, 1980.
54. Tay, O A, Stevenson, M G, De Vahl Davis and Oxley, P L B: "A Numerical Method for Calculating Temperature Distributions in Machining from Force and Shear Angle Measurements": Inst J Mach Tool Des Res, Vol 16, p335, 1977.

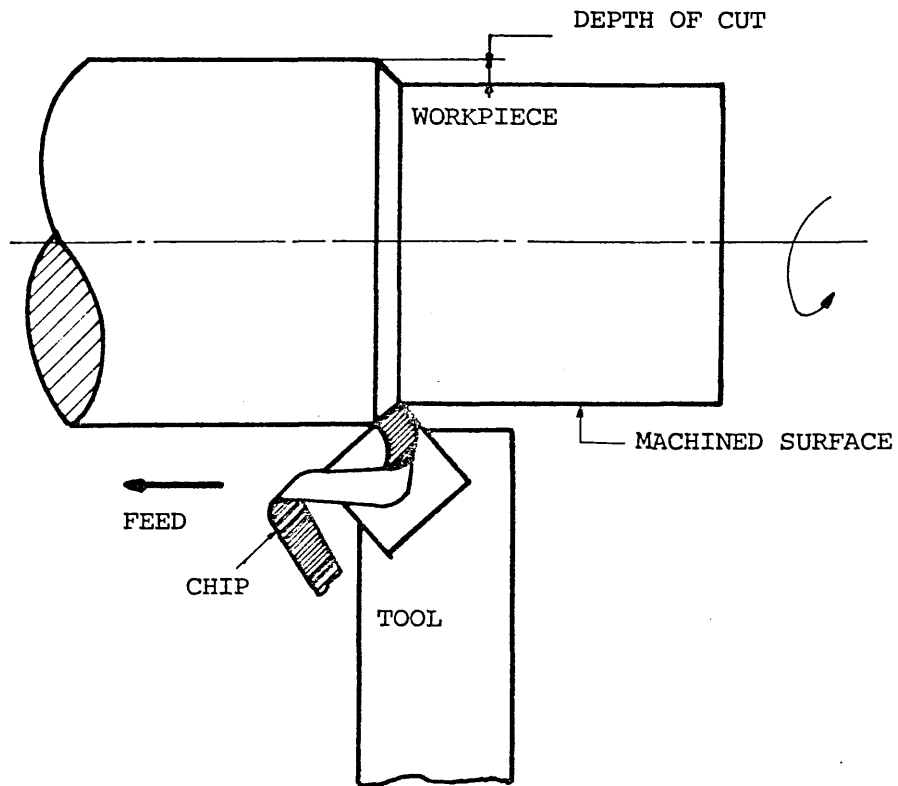


FIGURE 1 : Machining process

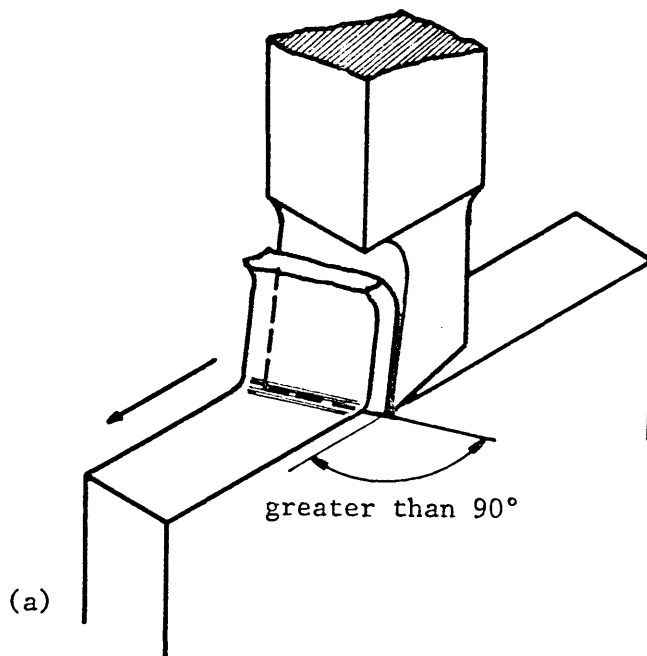
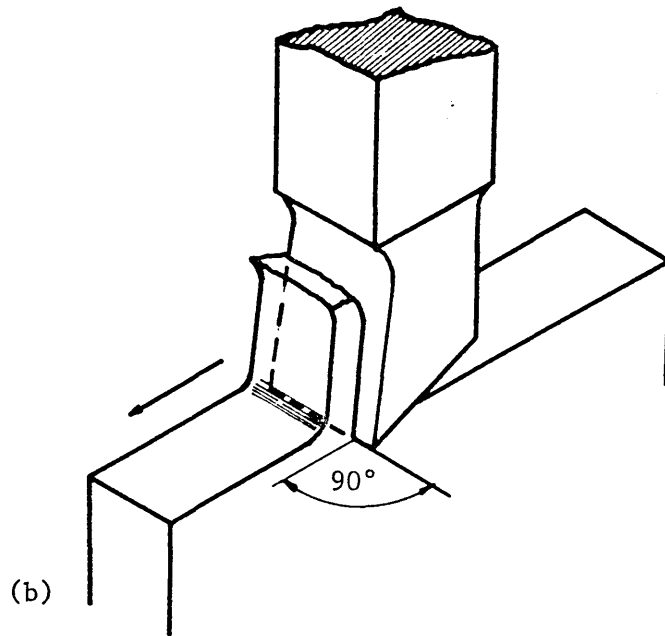


FIGURE 2 : Cutting operation

(a) oblique

(b) orthogonal

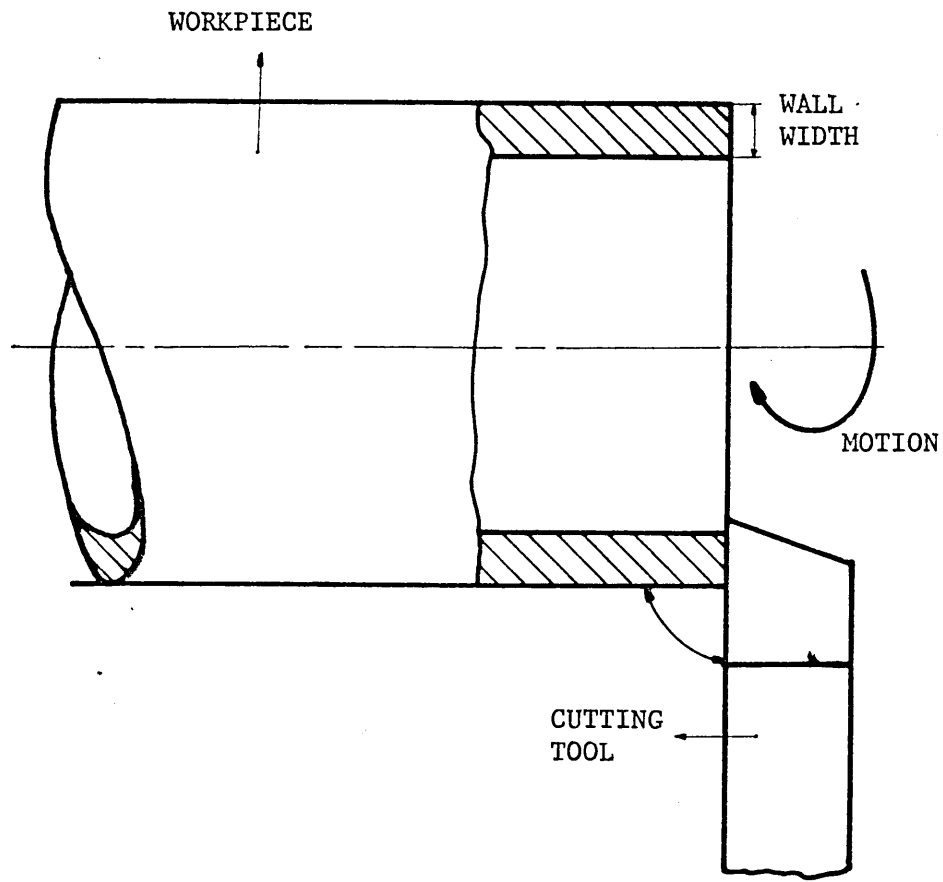


FIGURE 3 : Orthogonal machining with the lathe method

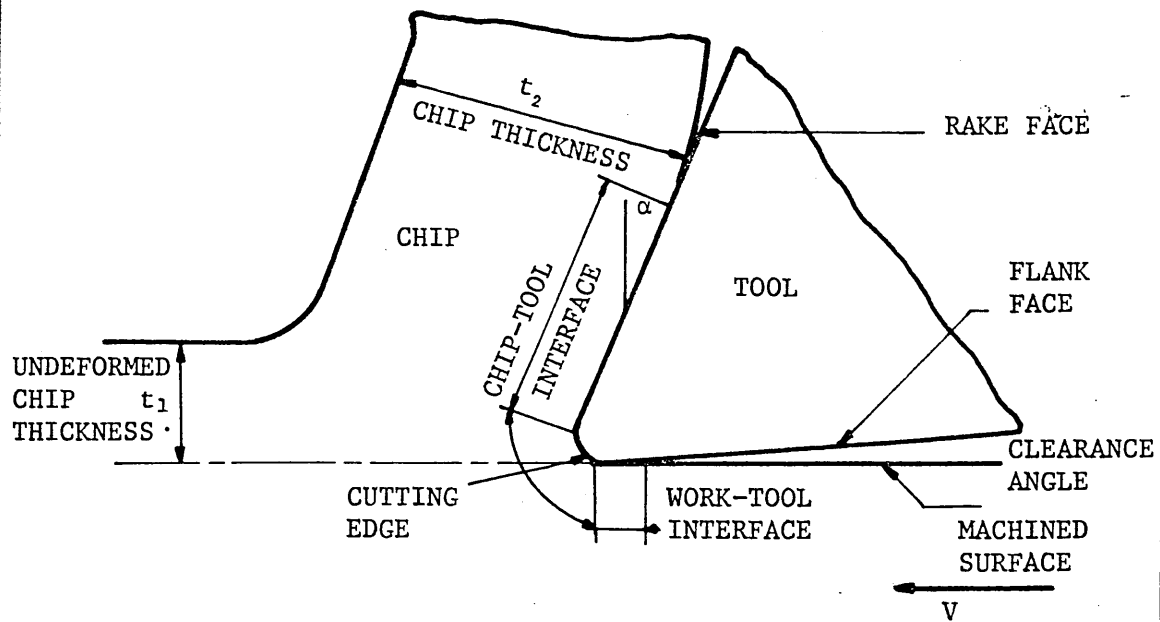


FIGURE 4 : Section through the tool and chip

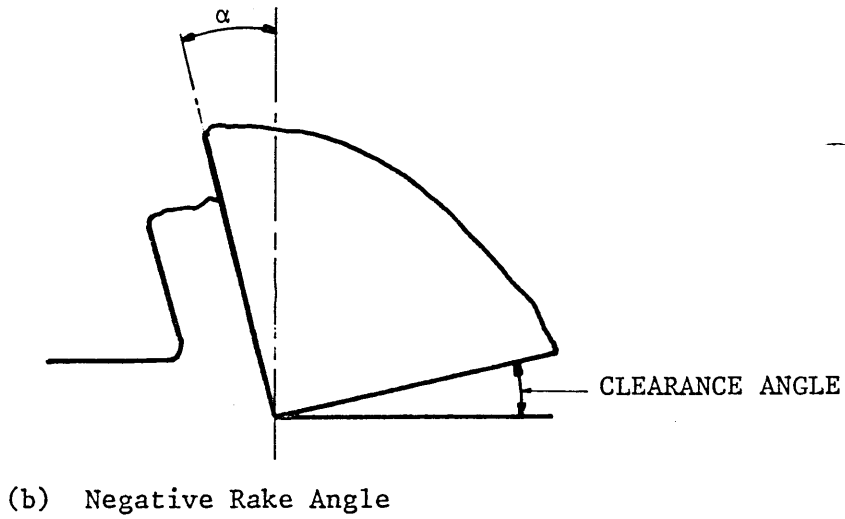
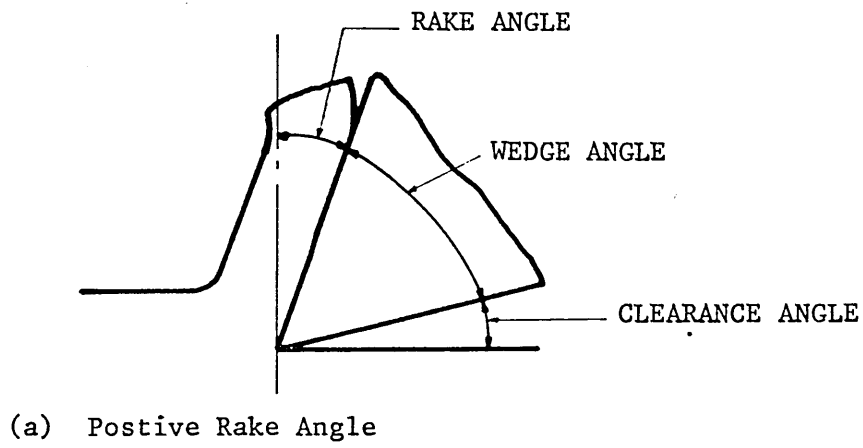


FIGURE 5 : Rake Angle Sign

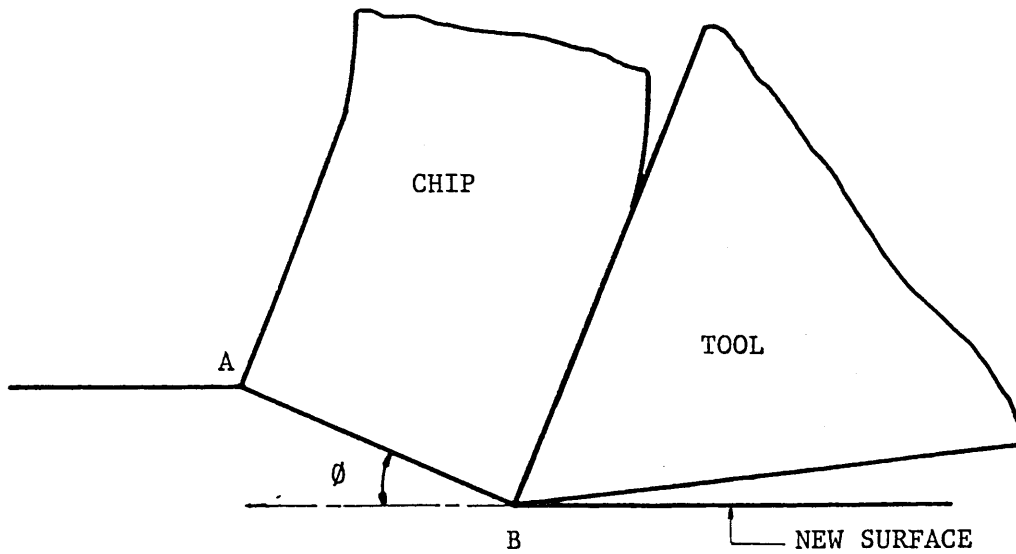


FIGURE 6 : Shear plane model of chip formation

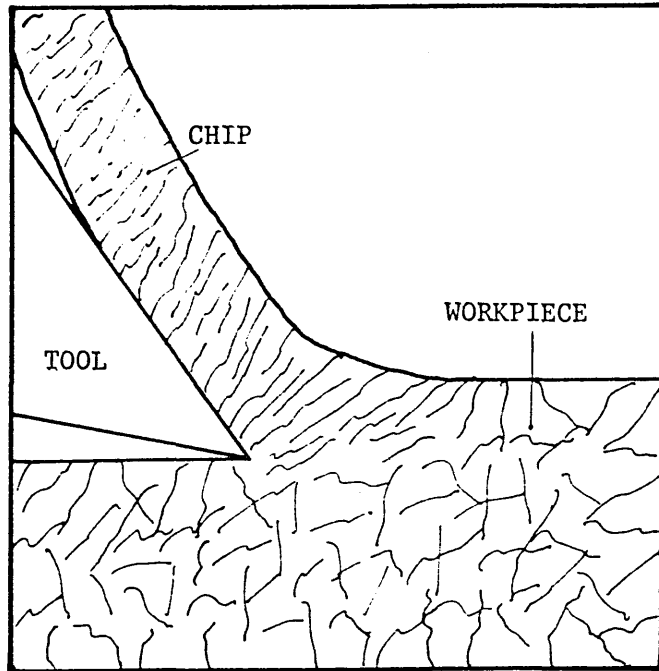


FIGURE 7 : Continuous chip type

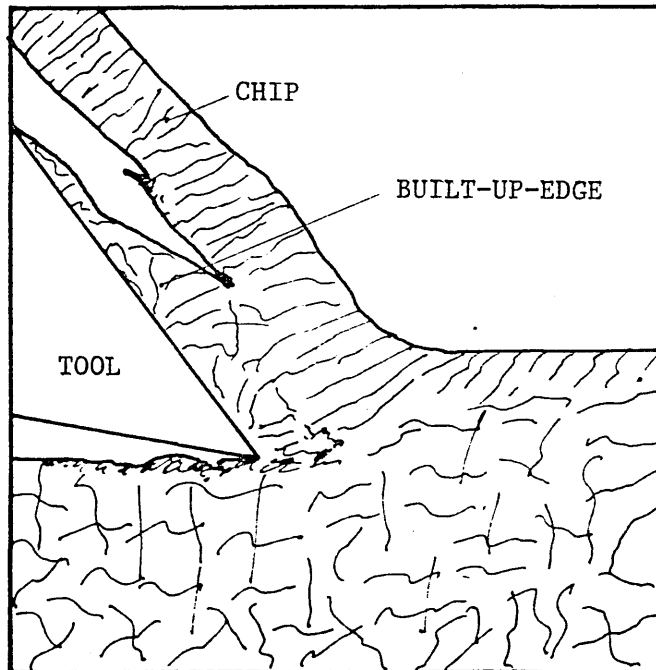


FIGURE 8 : Continuous chip with built-up-edge type

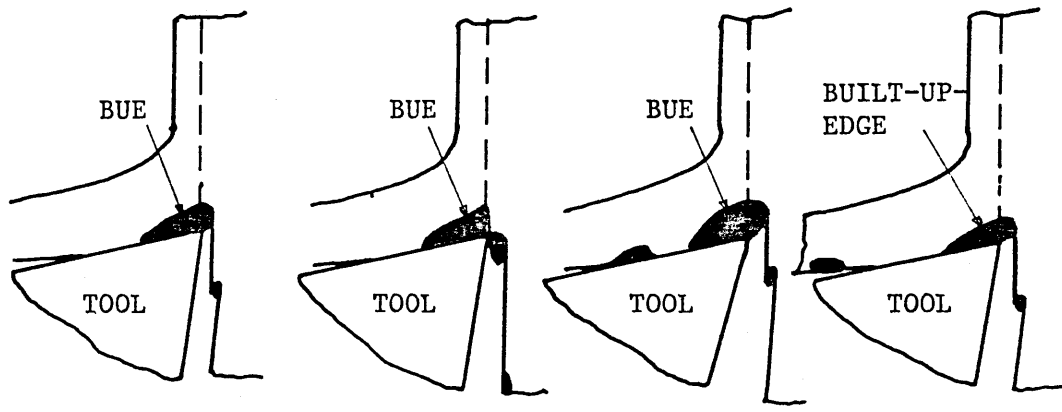


FIGURE 9 : Cycle of built-up-edge and break-down
 Ref [3]

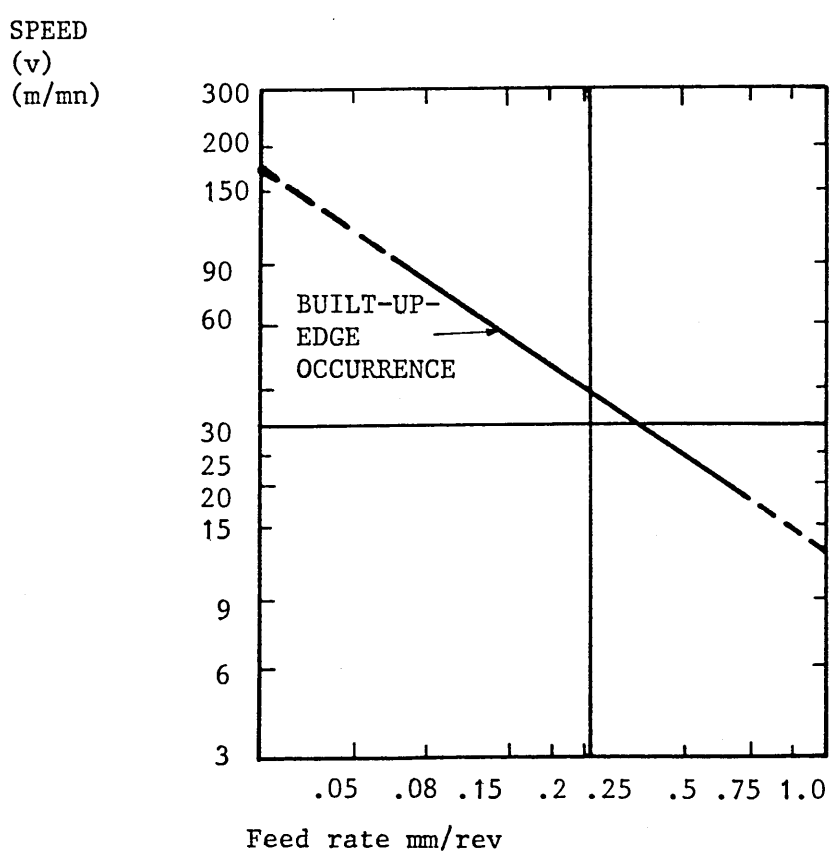


FIGURE 10 : Built-up-edge occurrence
 Ref[5]

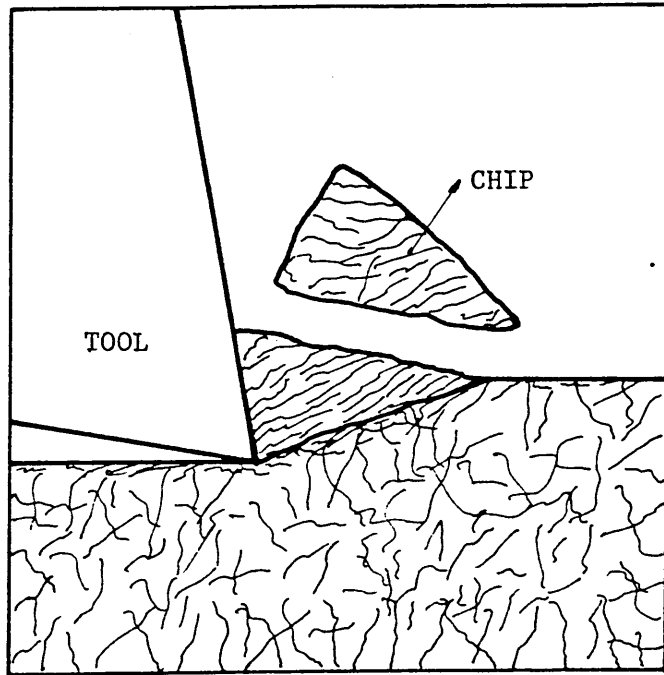


FIGURE 11 : Discontinuous chip type

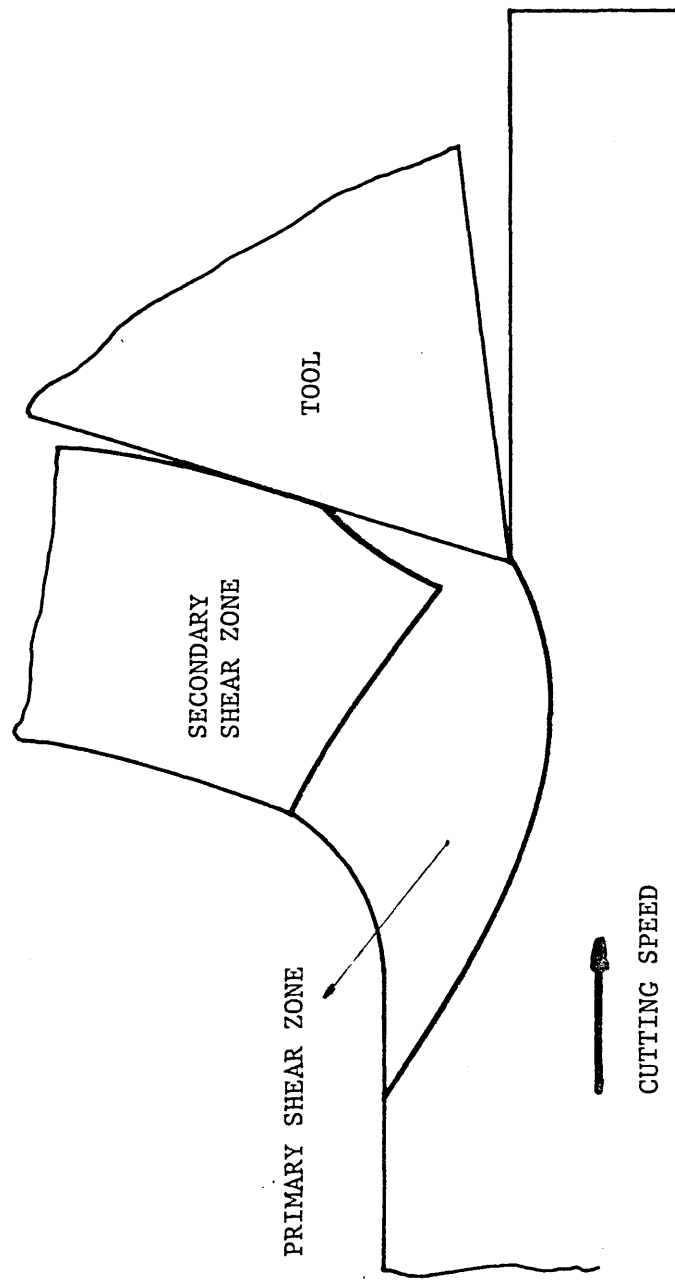
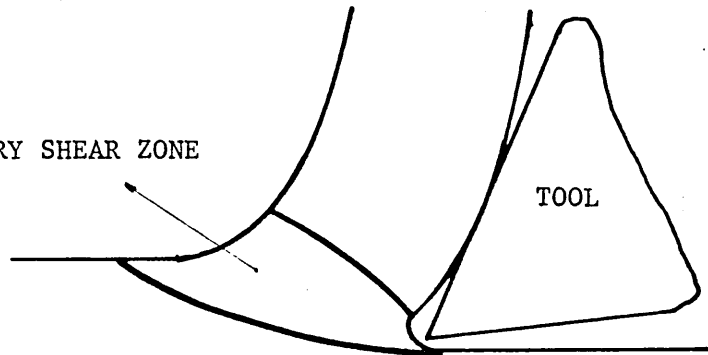


FIGURE 12 : Primary and secondary deformation zones

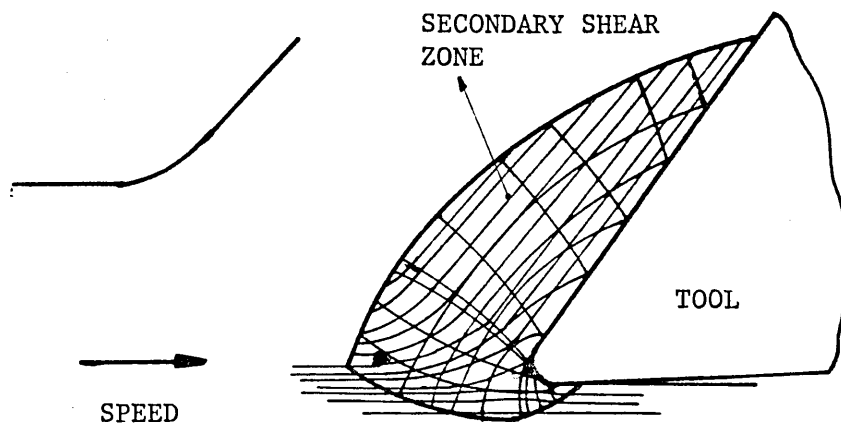
PRIMARY SHEAR ZONE



TOOL

FIGURE 13 : Shear zone model

Ref [17]



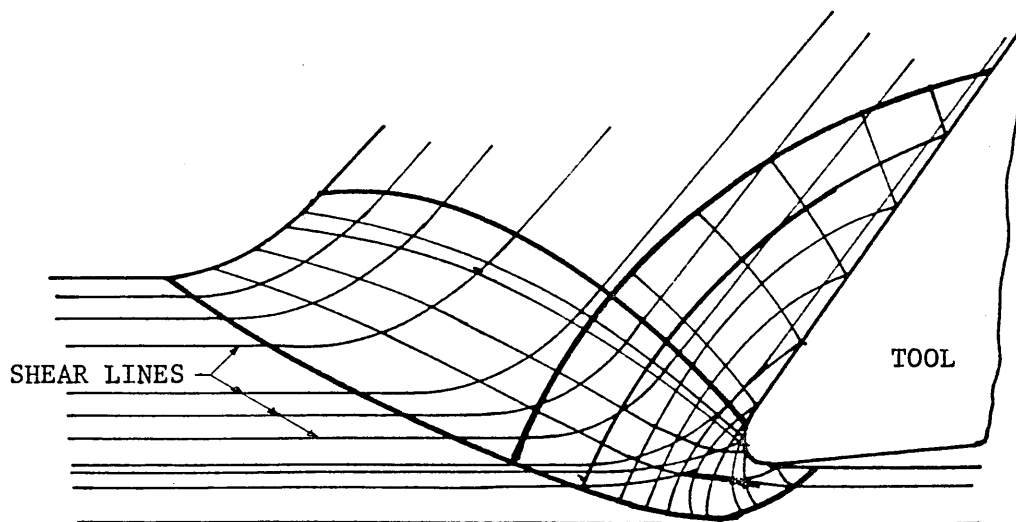
SECONDARY SHEAR ZONE

TOOL

SPEED

FIGURE 14 : Slip field model

Ref [18]



SHEAR LINES

TOOL

FIGURE 15 : Deformation zone model

Ref [19]

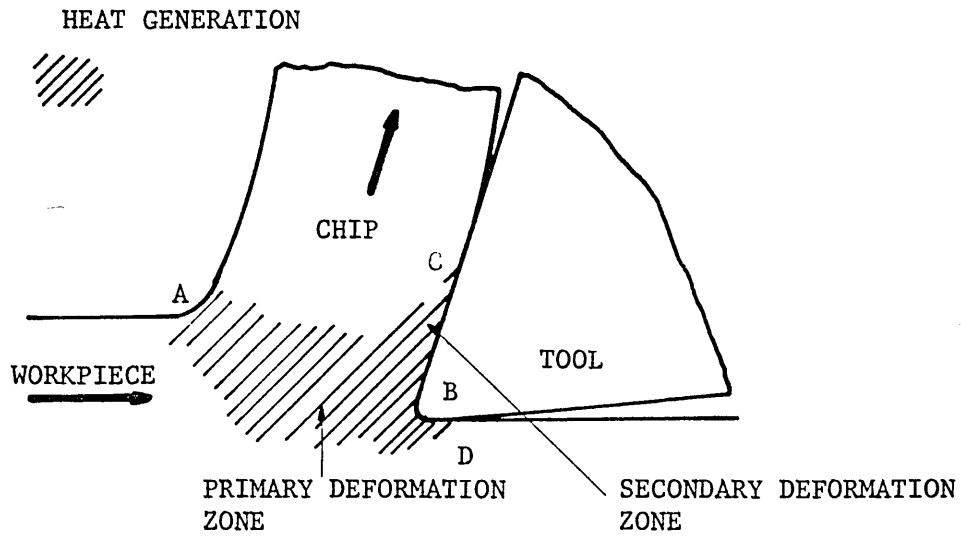


FIGURE 16 : Generation of heat in orthogonal cutting

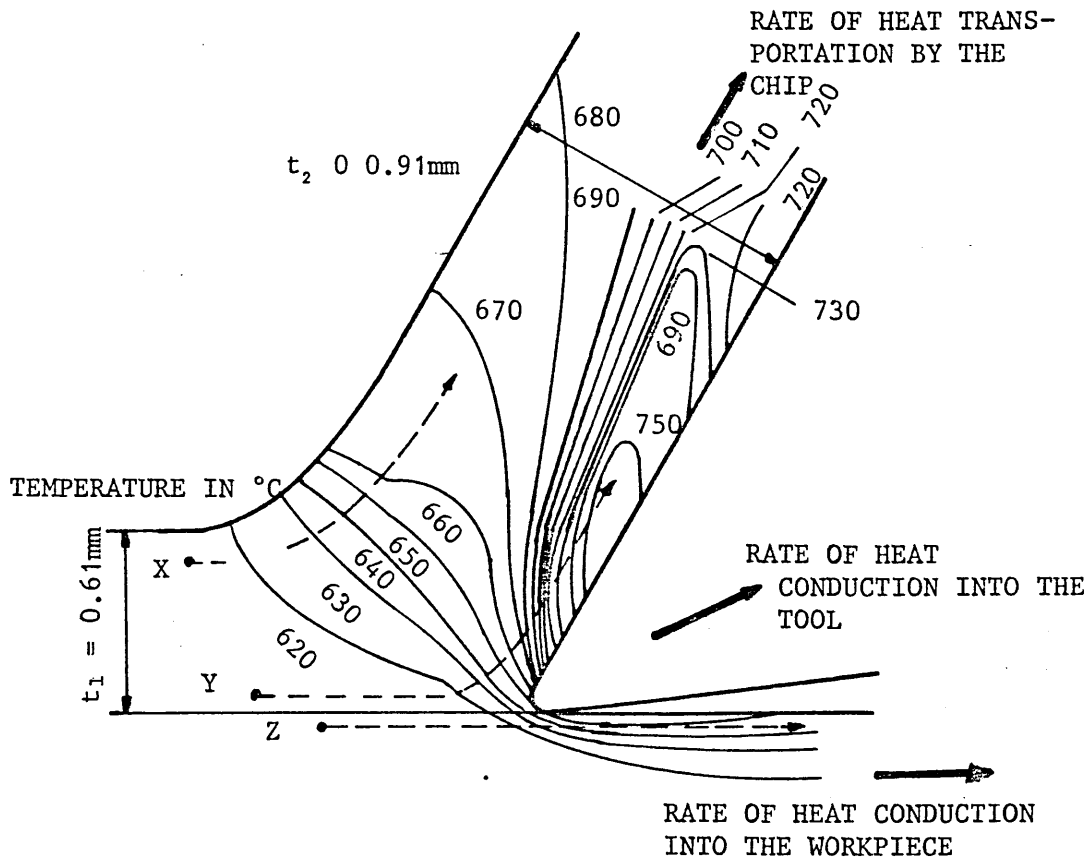


FIGURE 17 : Temperature distribution in workpiece and chip during orthogonal cutting for free cutting mild steel

[Ref 22]

//// = INSULATED SURFACE

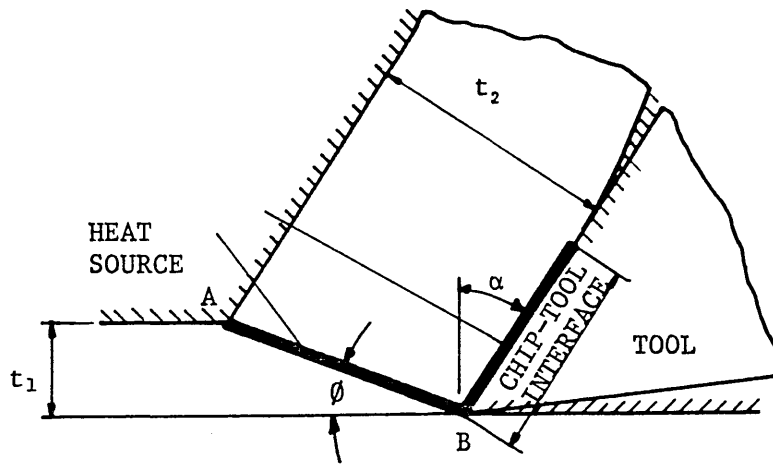


FIGURE 18 : Idealized model of cutting process
employed in theoretical work on cutting
temperature Ref [23-26]

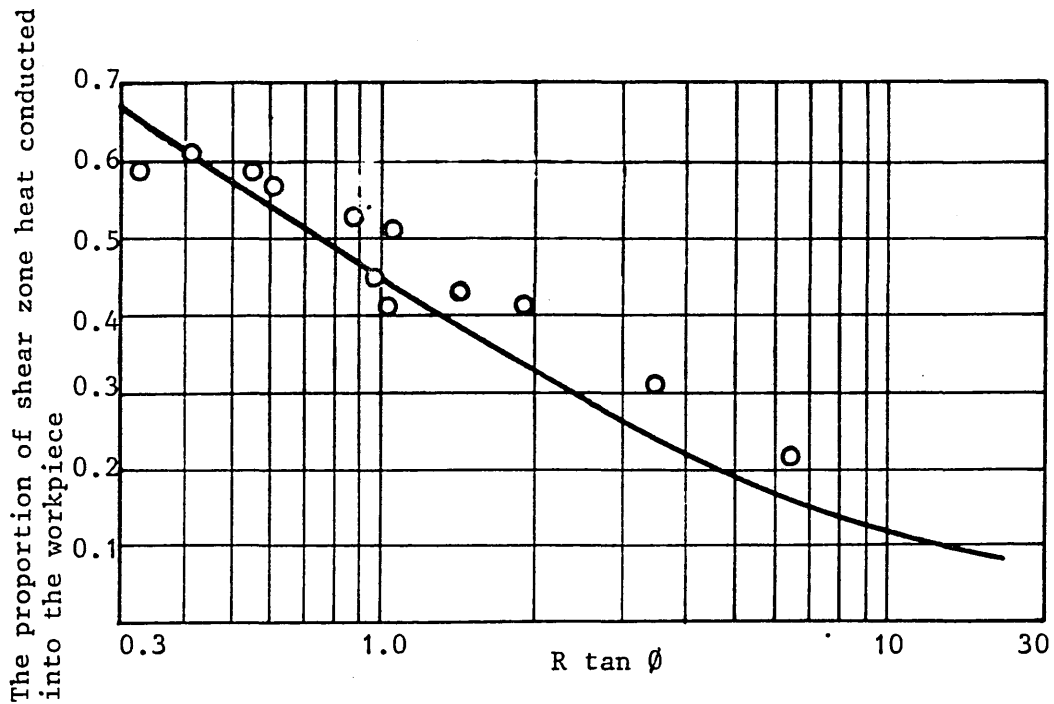


FIGURE 19 : Effect of $R \tan \phi$ on division of shear-zone
heat between chip and workpiece where
 R = thermal number and ϕ = the shear angle
 ϕ , experiments ; continuous line
(theoretical) Ref [27]

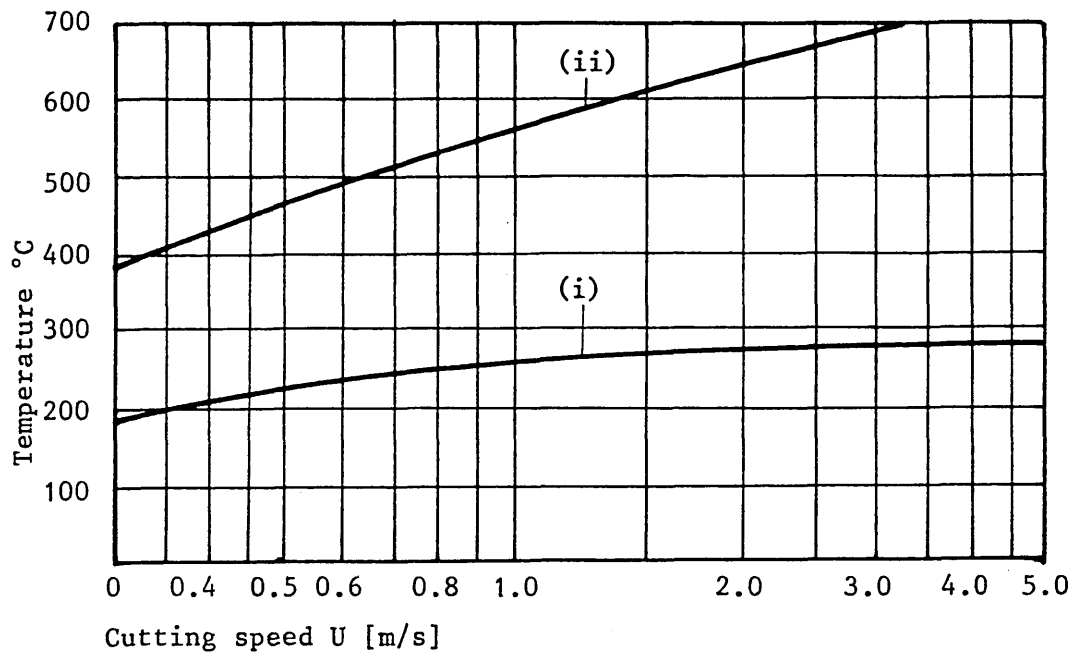


FIGURE 20 : Effect of cutting speed on cutting temperatures (theoretical)
 (i) mean shear zone temperature
 (ii) maximum tool face temperature
 Ref [28]

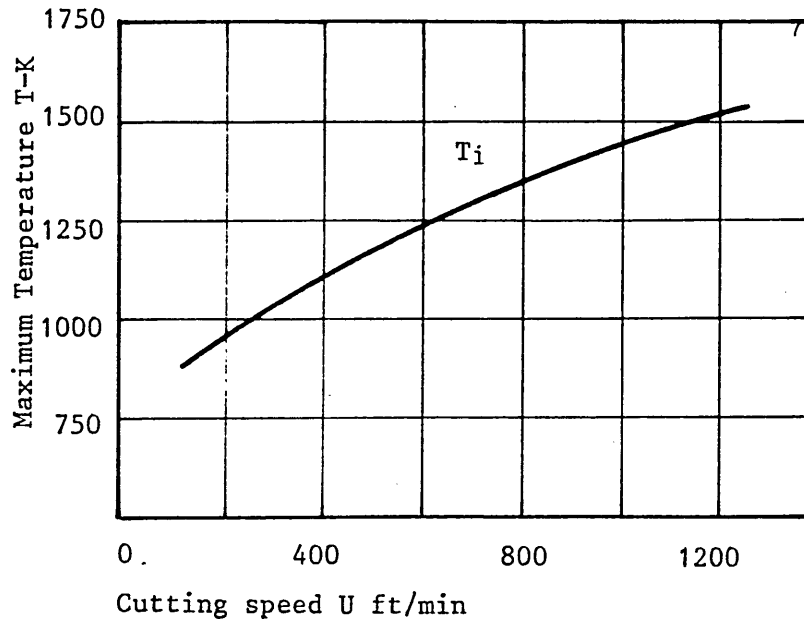


FIGURE 21 : Variation in tool-chip interface temperature with cutting speed
 $t_1 = 0.0037$ inches Ref [29]

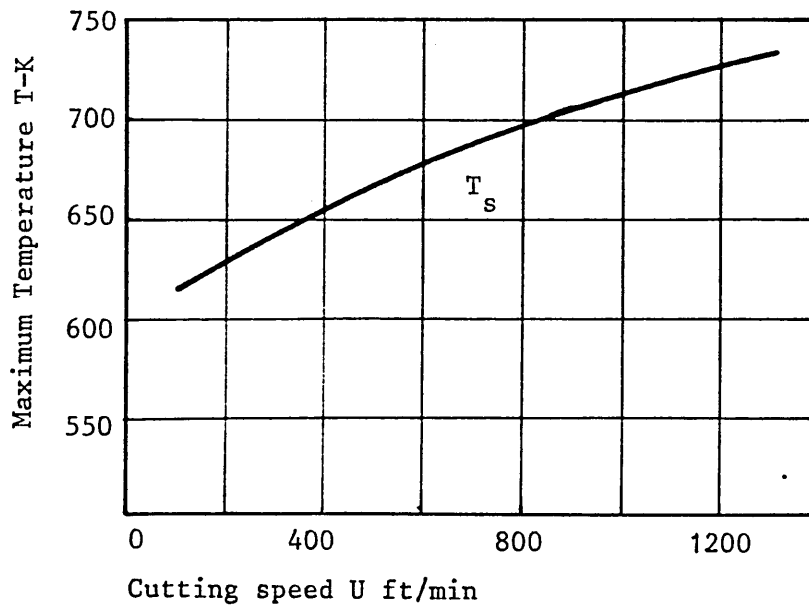


FIGURE 22 : Variation in shear zone temperature with cutting speed
 $t_1 = 0.0037$ inches Ref [29]

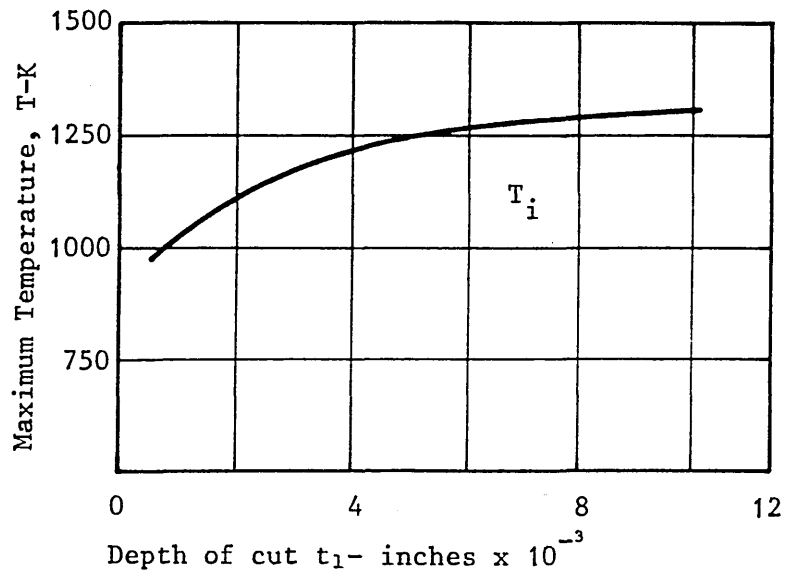


FIGURE 23 : Variation in tool-chip interface temperature with depth of cut
 $U = 542$ ft/min Ref [29]

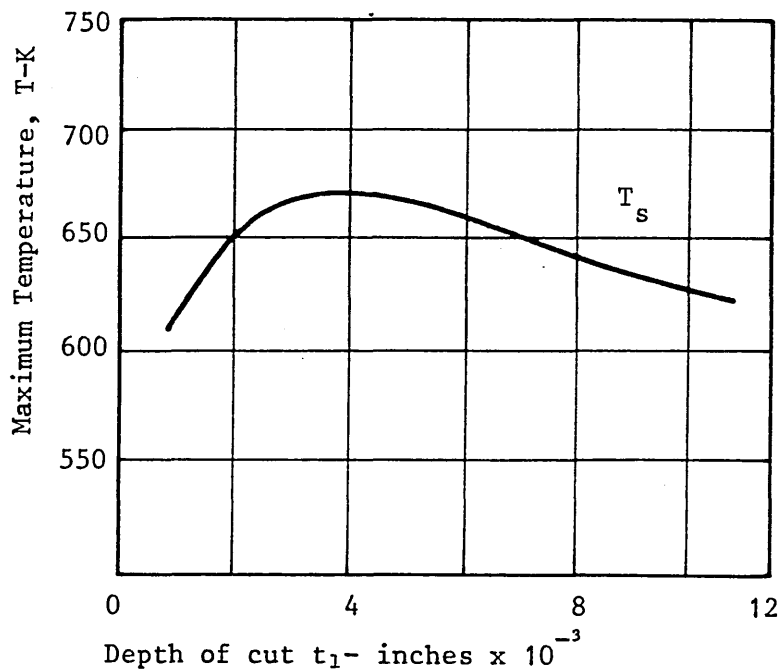
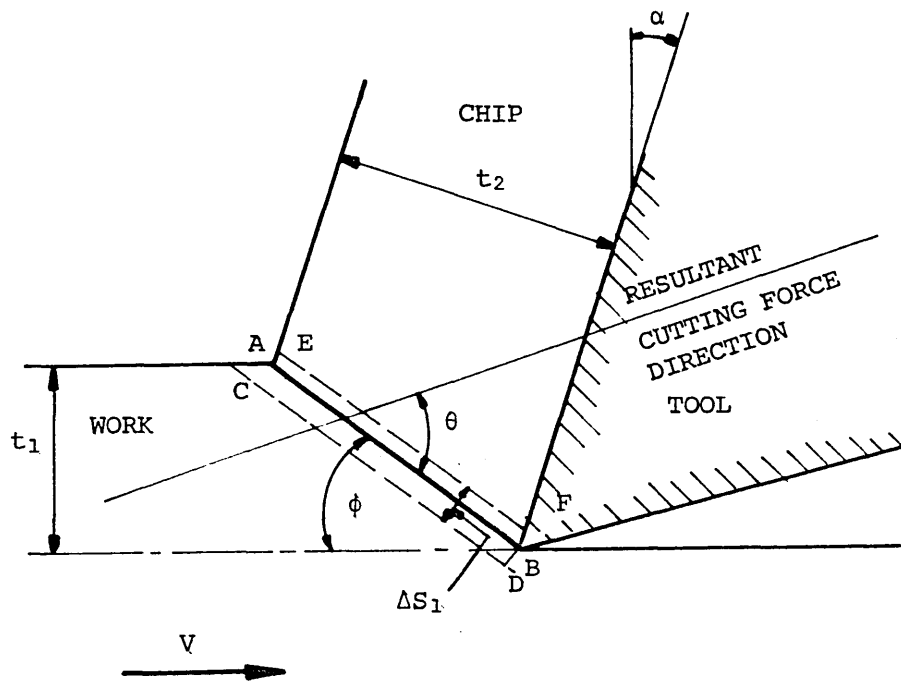
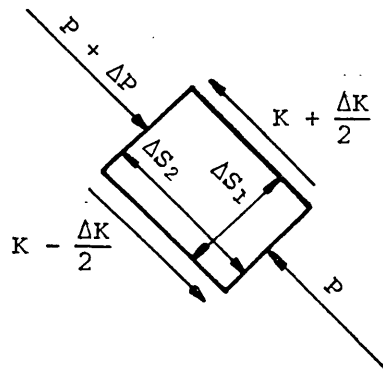


FIGURE 24 : Variation in shear zone temperature with depth of cut $U = 542$ ft/ins
 Ref [29]



(a) Slip line field



(b) Element of shear zone

FIGURE 27 : Shear plane model

(a) Slip line field

(b) Element of shear zone

Ref [30]

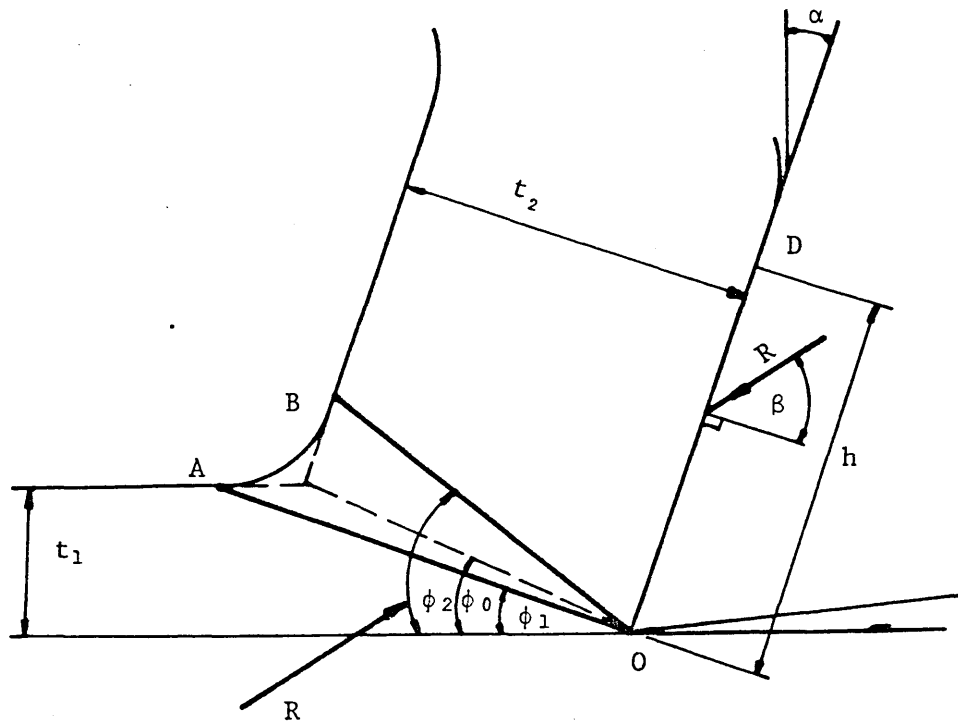


FIGURE 28 : Model of analysis presented by Okushima
and Hitomi Ref [31]

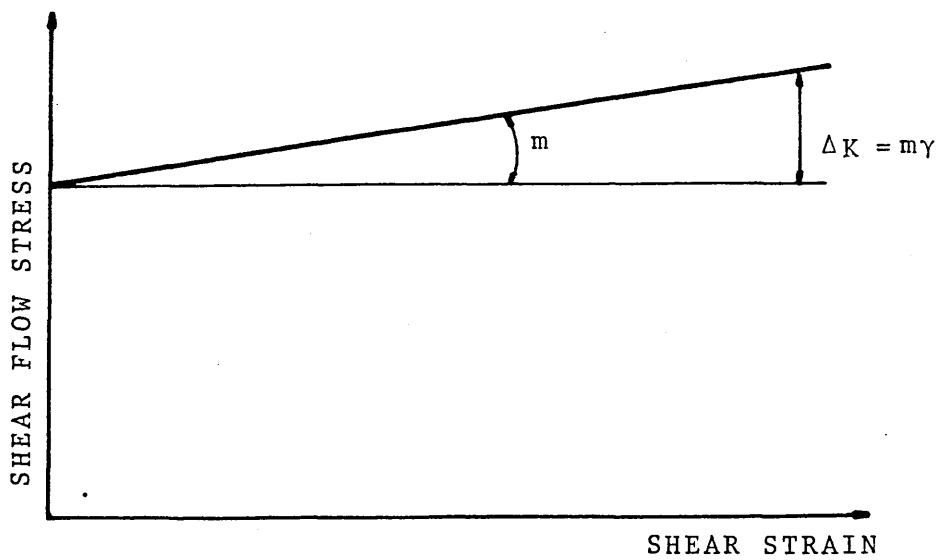


FIGURE 29 : Idealized shear flow stress-strain curve

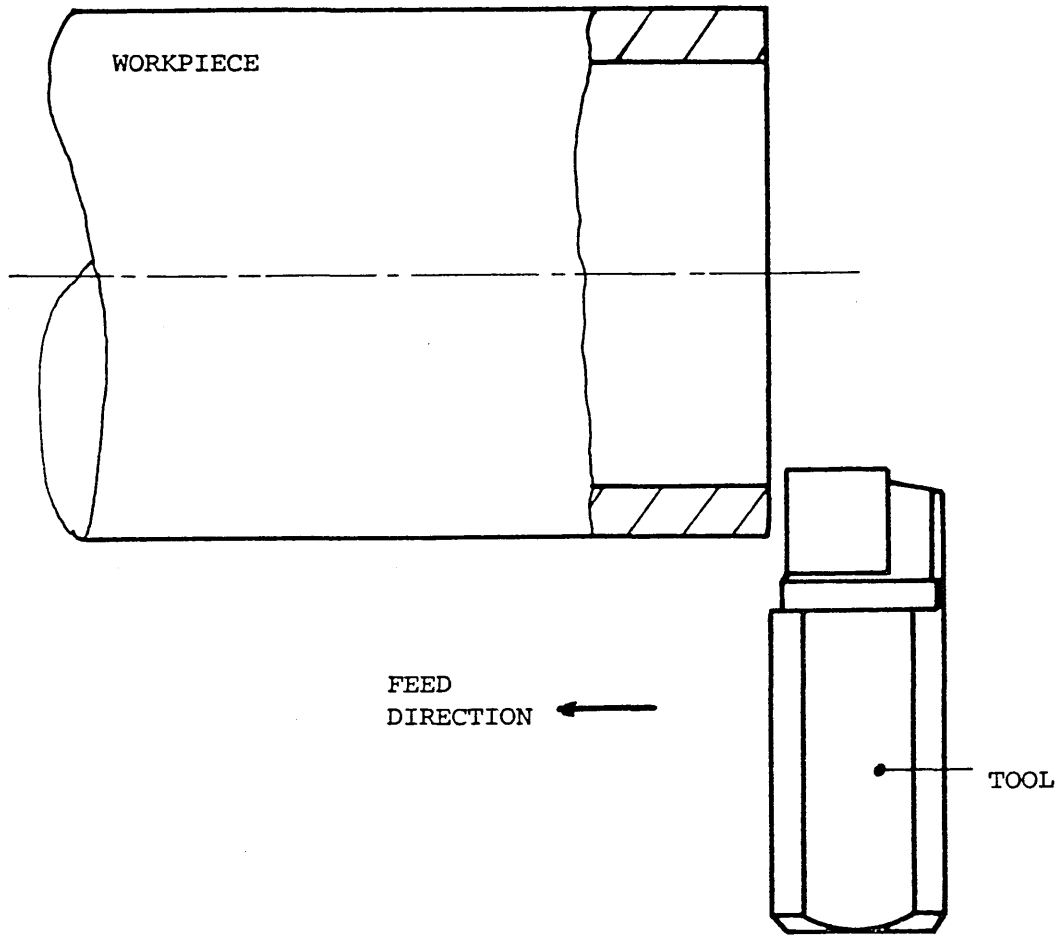


FIGURE 30 : Geometry of Cutting

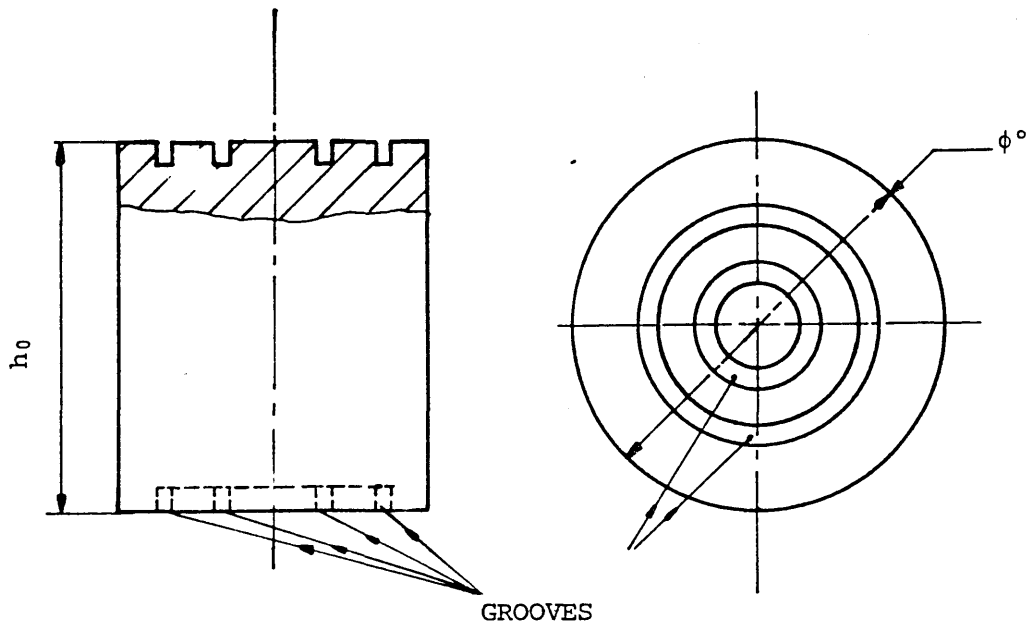


FIGURE 31 : Configuration of the specimen used in the compression test

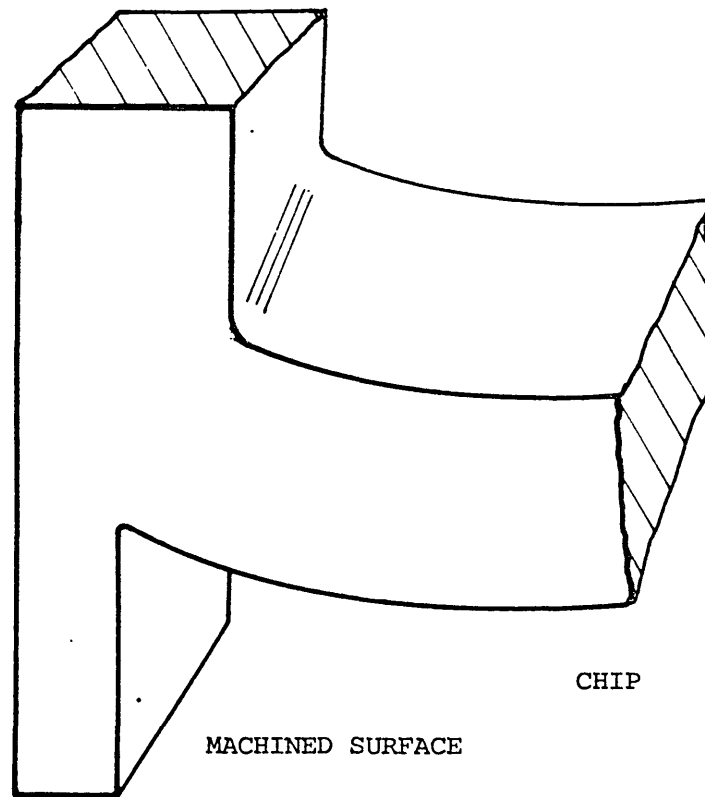


FIGURE 32 : Plain strain section

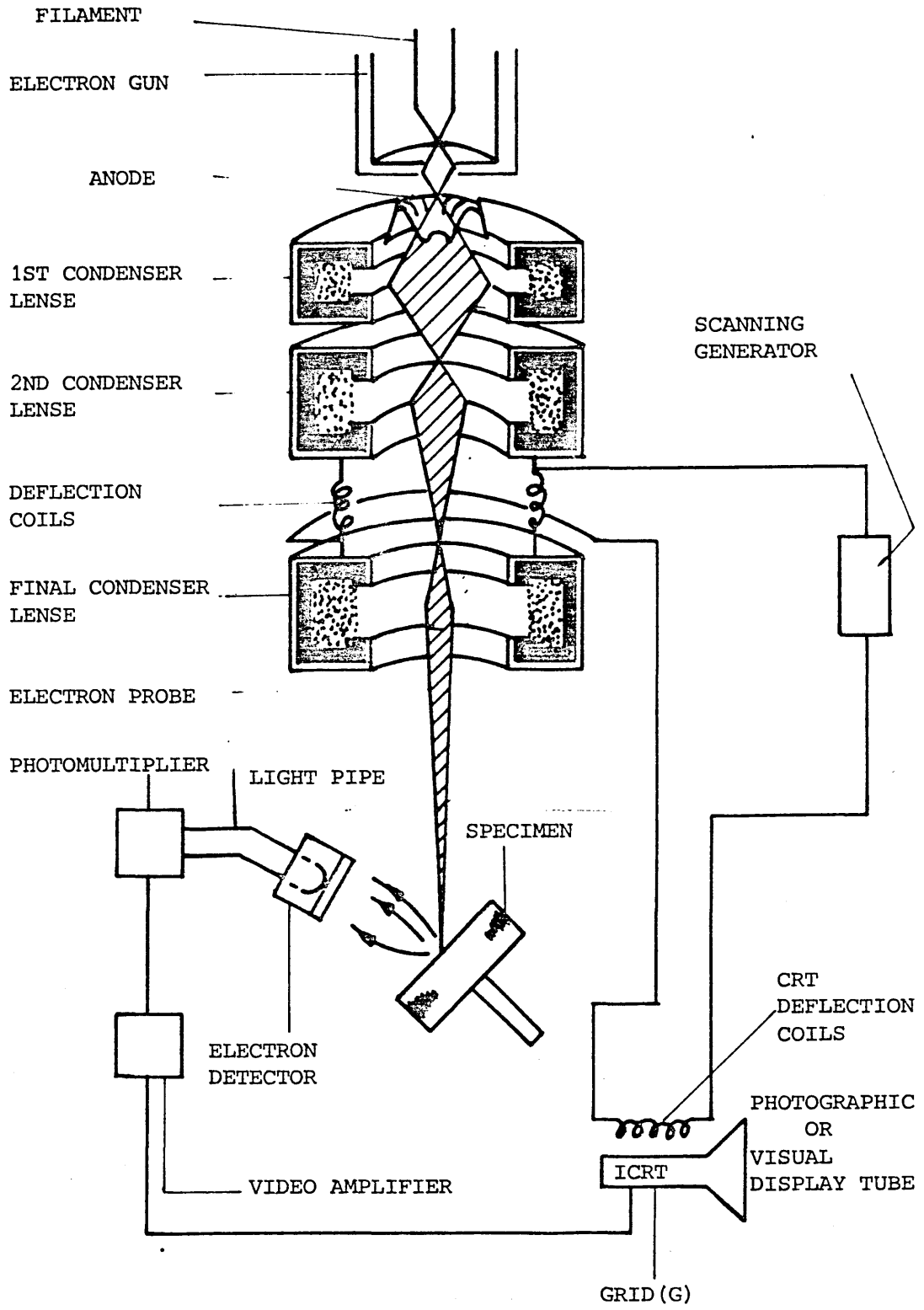


FIGURE 33 : Principle of the scanning-electron microscope

MATERIAL EN₈
 $t_1 = 0.488$ [mm]
 $w = 3.15$ [mm]
 $\alpha = 0^\circ$

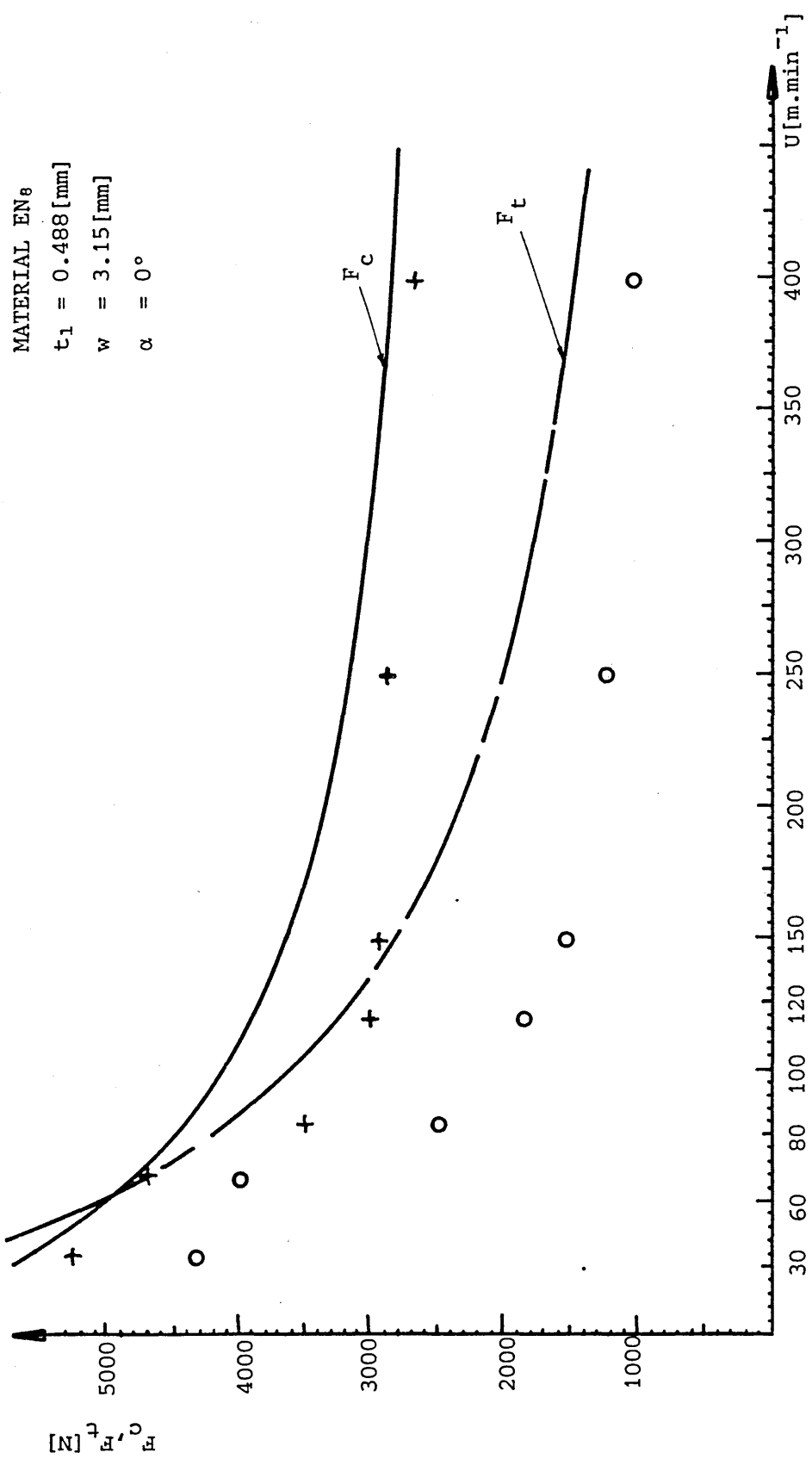


FIGURE 34 : Variation of the cutting forces with change in cutting speed in machining the EN₈ (+,o) results obtained from experiments

MATERIAL ALUMINIUM

$t_1 = 0.488$ [mm]

$w = 3.20$ [mm]

$\alpha = 0^\circ$

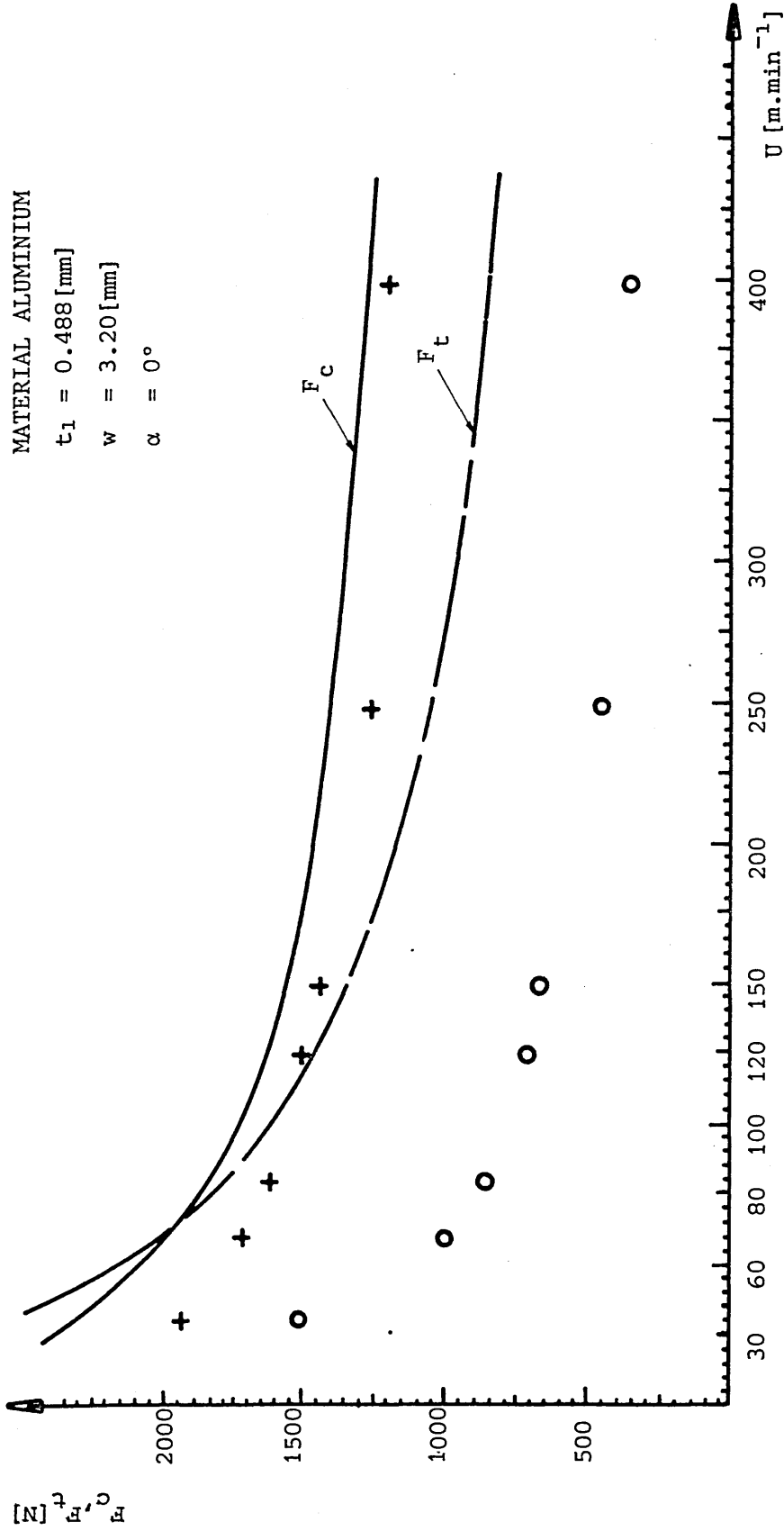


FIGURE 35 : Variation of the cutting forces with change in cutting speed in machining Aluminium (+,o) results obtained from experiments

MATERIAL 70-30 BRASS
 $t_i = 0.244$ [mm]
 $w = 3.35$ [mm]
 $\alpha = 0^\circ$

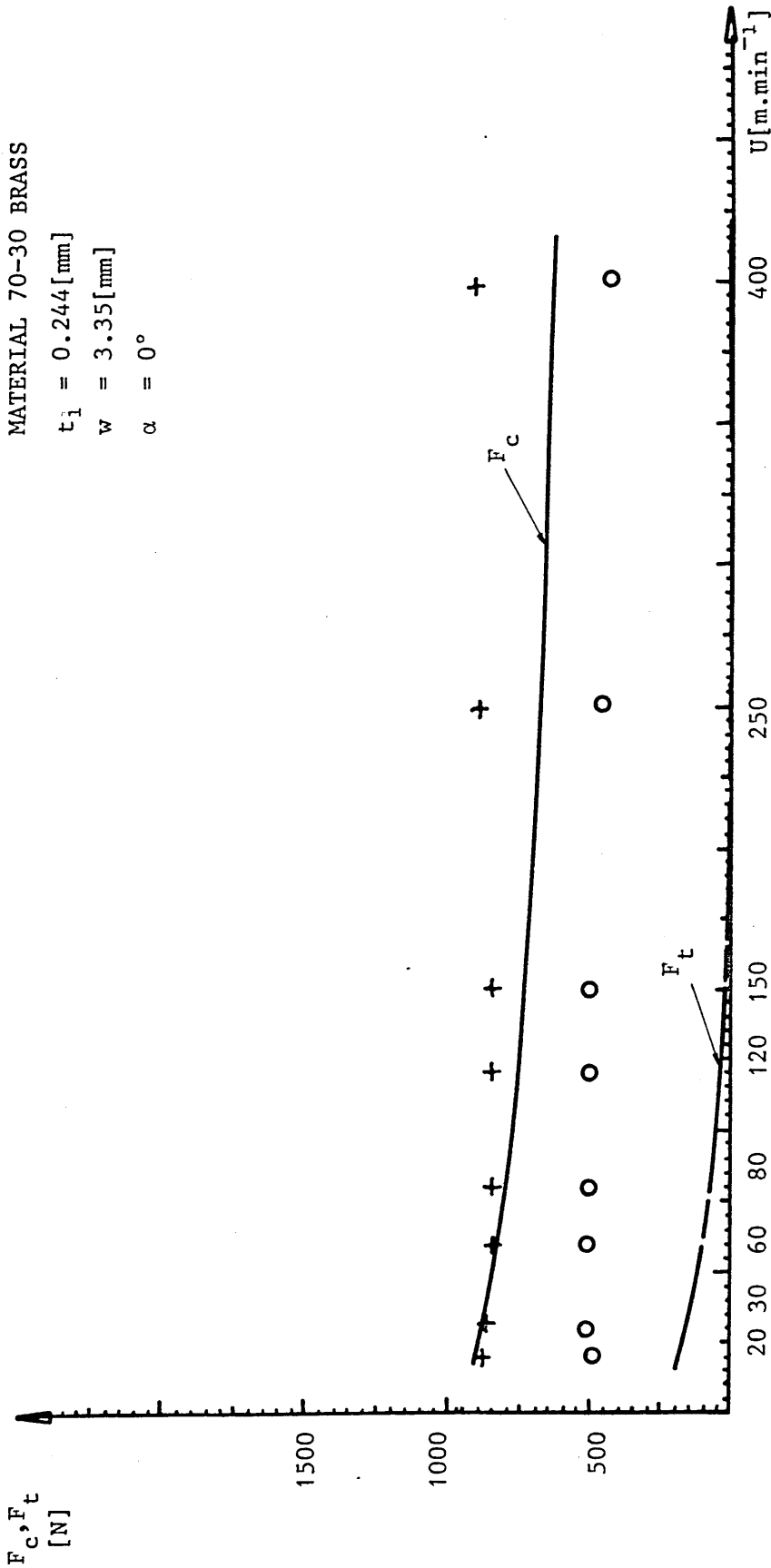


FIGURE 36 : Variation of the cutting forces with change in cutting speed (+,o) results obtained from experiments

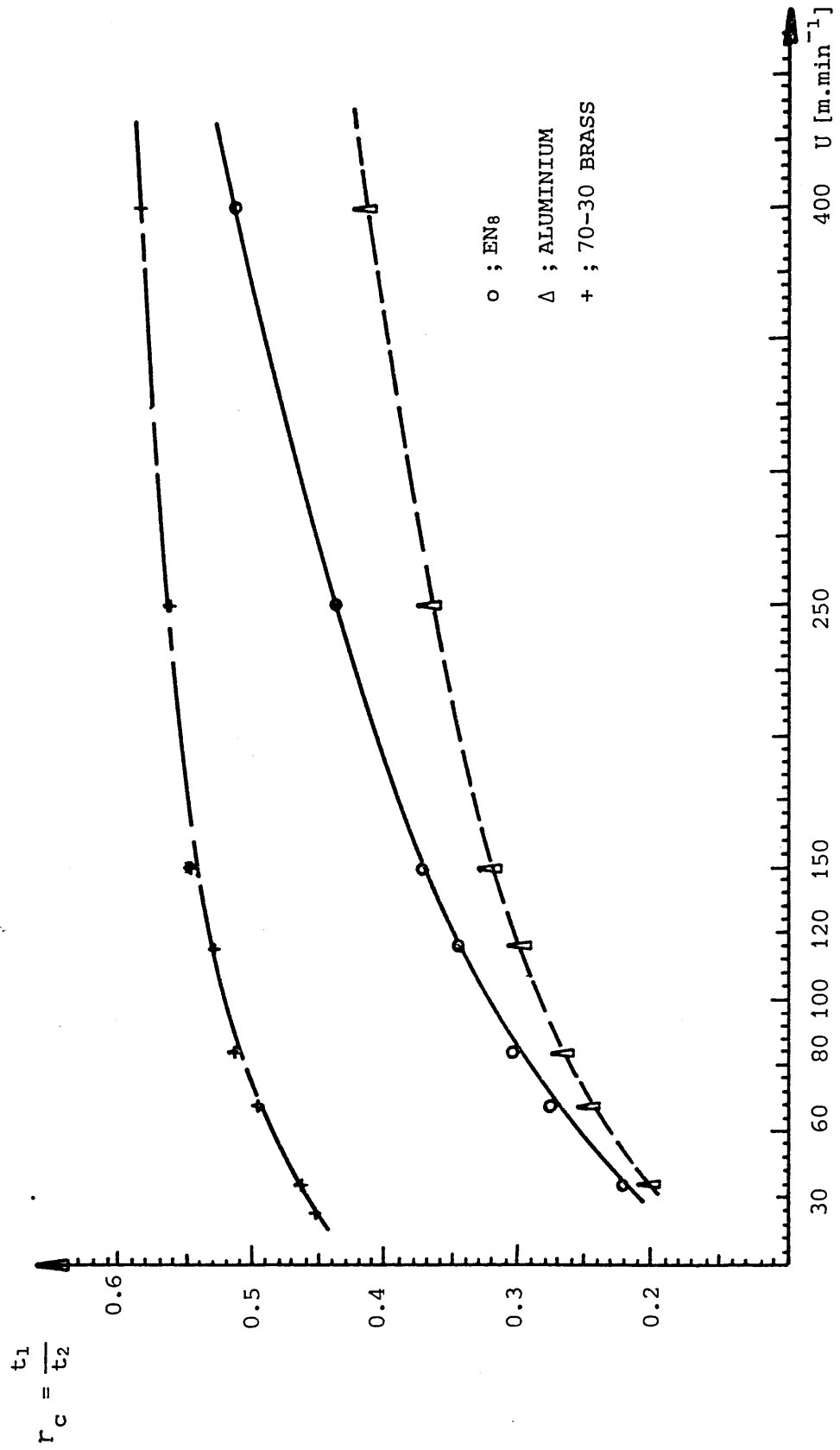


FIGURE 37 : Variation of the chip thickness ratio with cutting speed

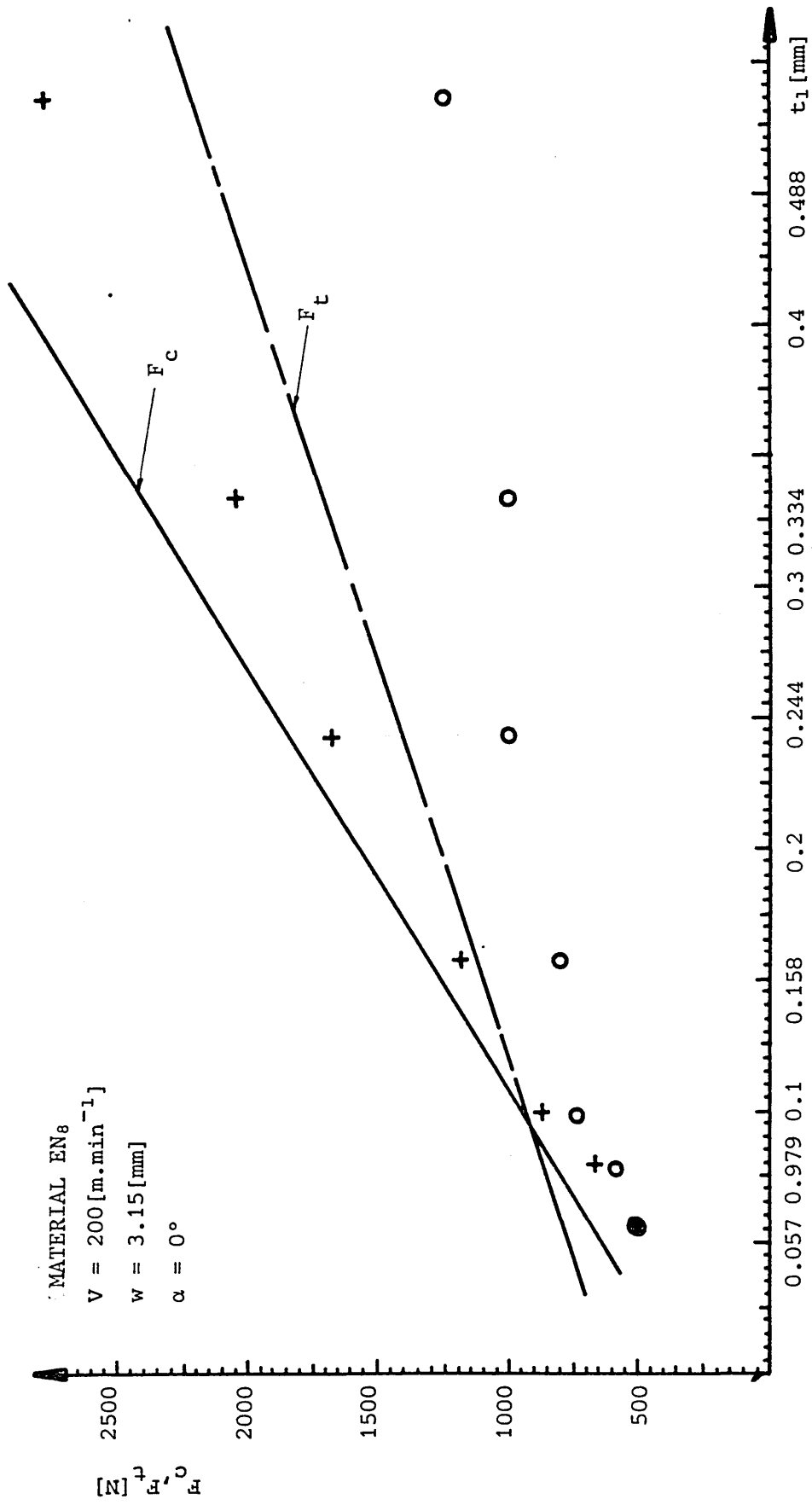


FIGURE 38 : Variation of the cutting forces with change in the undeformed chip thickness
 (+,o) results obtained from experiments (————); (-----) predicted

MATERIAL ALUMINIUM

$V = 200 \text{ [m.min}^{-1}\text{]}$

$w = 3.20 \text{ [mm]}$

$\alpha = 0^\circ$

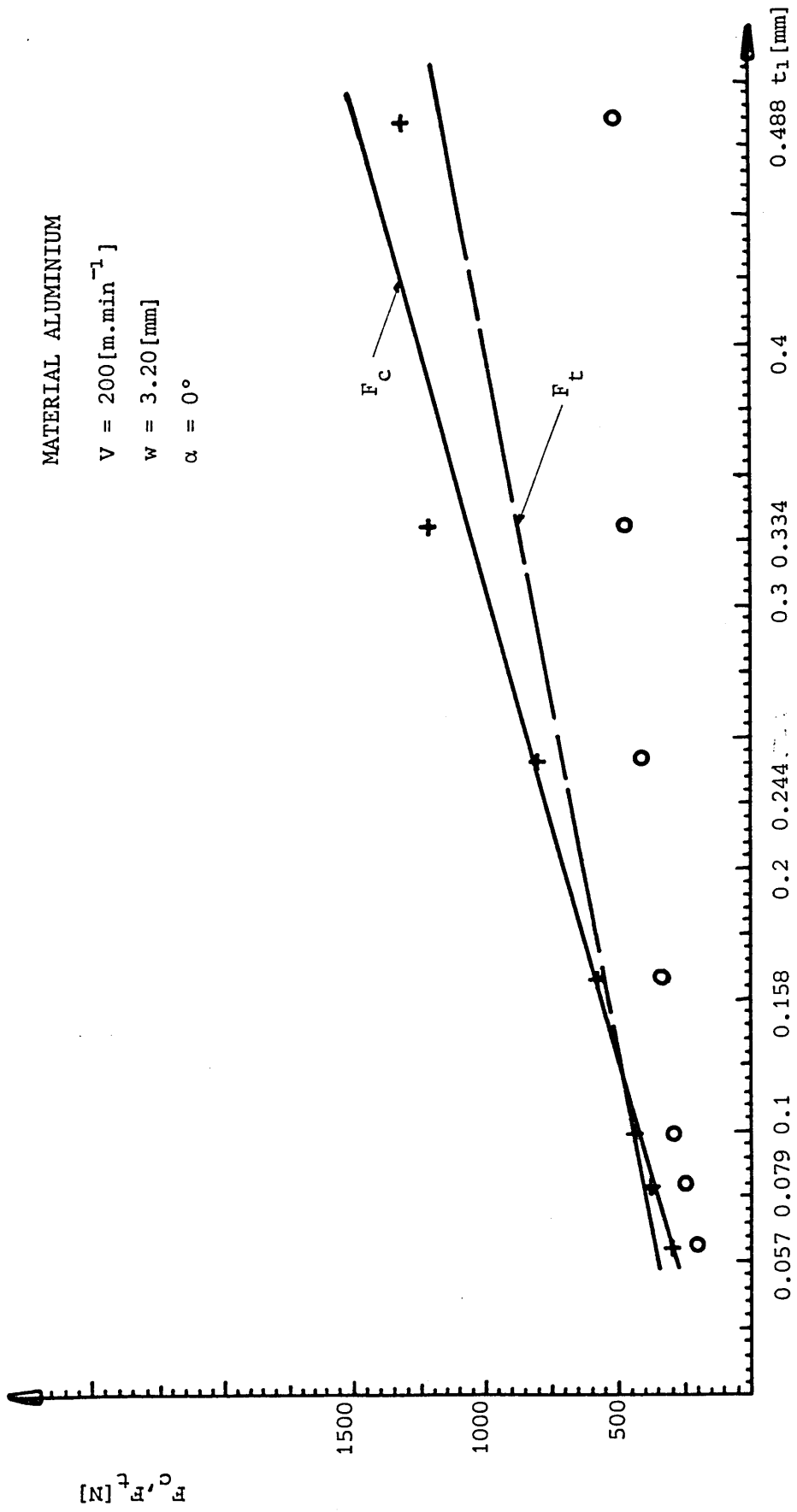


FIGURE 39 : Variation of the cutting forces with undeformed chip thickness (+,o) results obtained from experiments

MATERIAL 70-30 BRASS
 $U \doteq 200[\text{m.min}^{-1}]$
 $w = 3.35[\text{mm}]$
 $\alpha = 0^\circ$

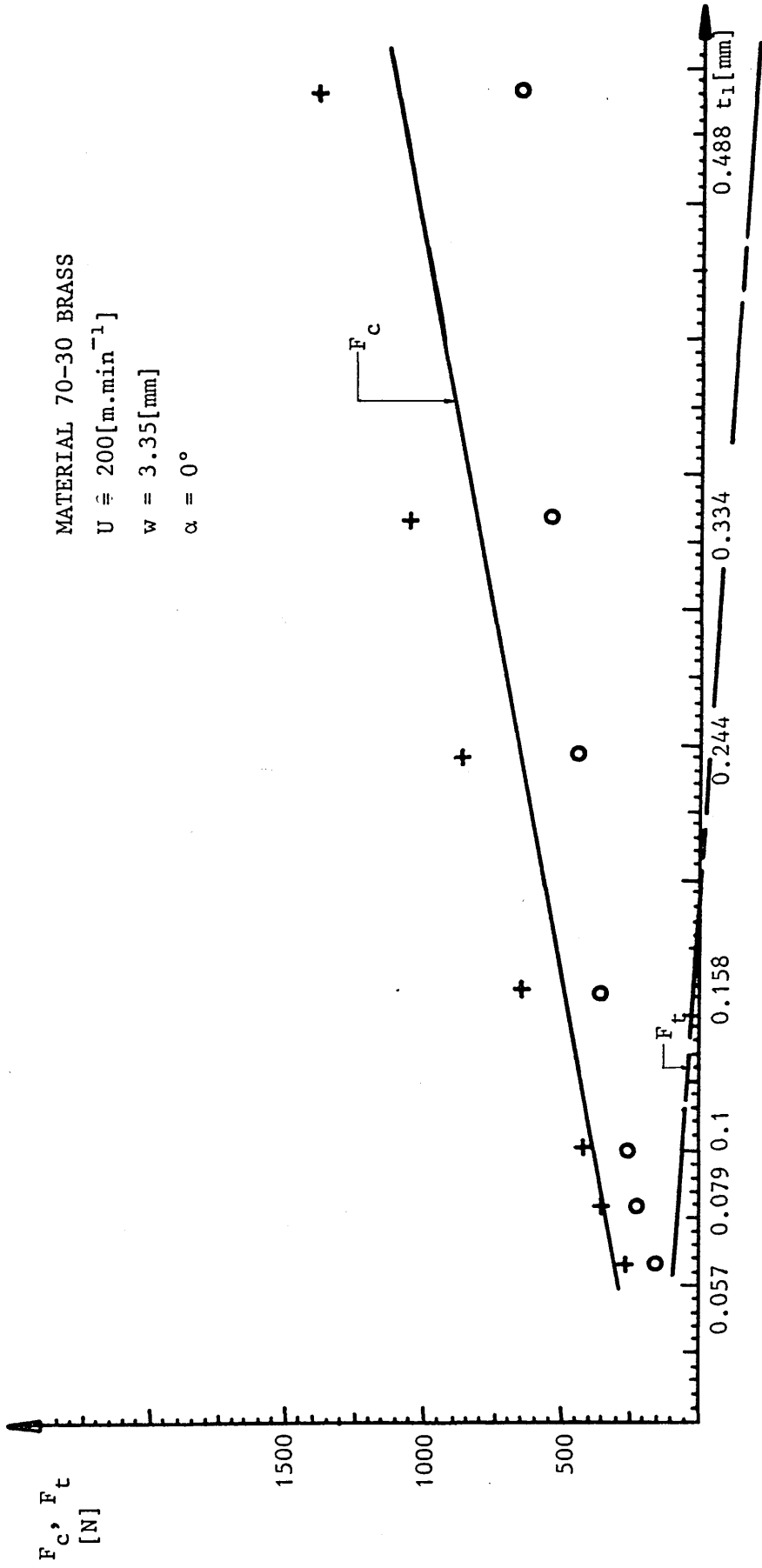


FIGURE 40 : Variation of the cutting forces with undeformed chip thickness (+,o) results obtained from experiments

○ ; EN8
 △ ; ALUMINIUM
 + ; 70-30 BRASS

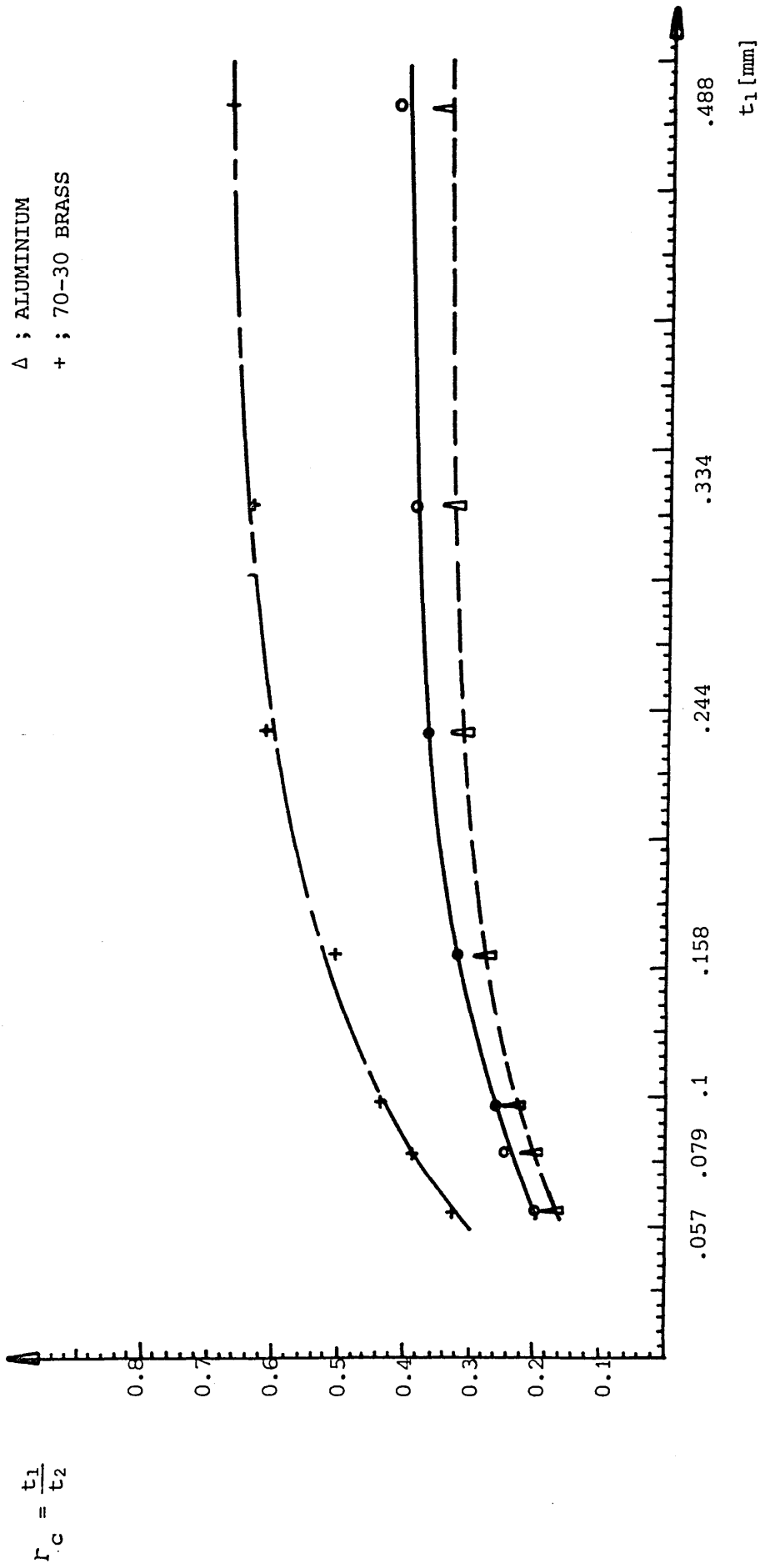


FIGURE 41 : Variation of the chip thickness ratio with the undeformed chip thickness

[N] F_c F_t

MATERIAL EN8
V = 200 [m.min⁻¹]
t₁ = 0.244 [mm]
w = 3.15 [mm]

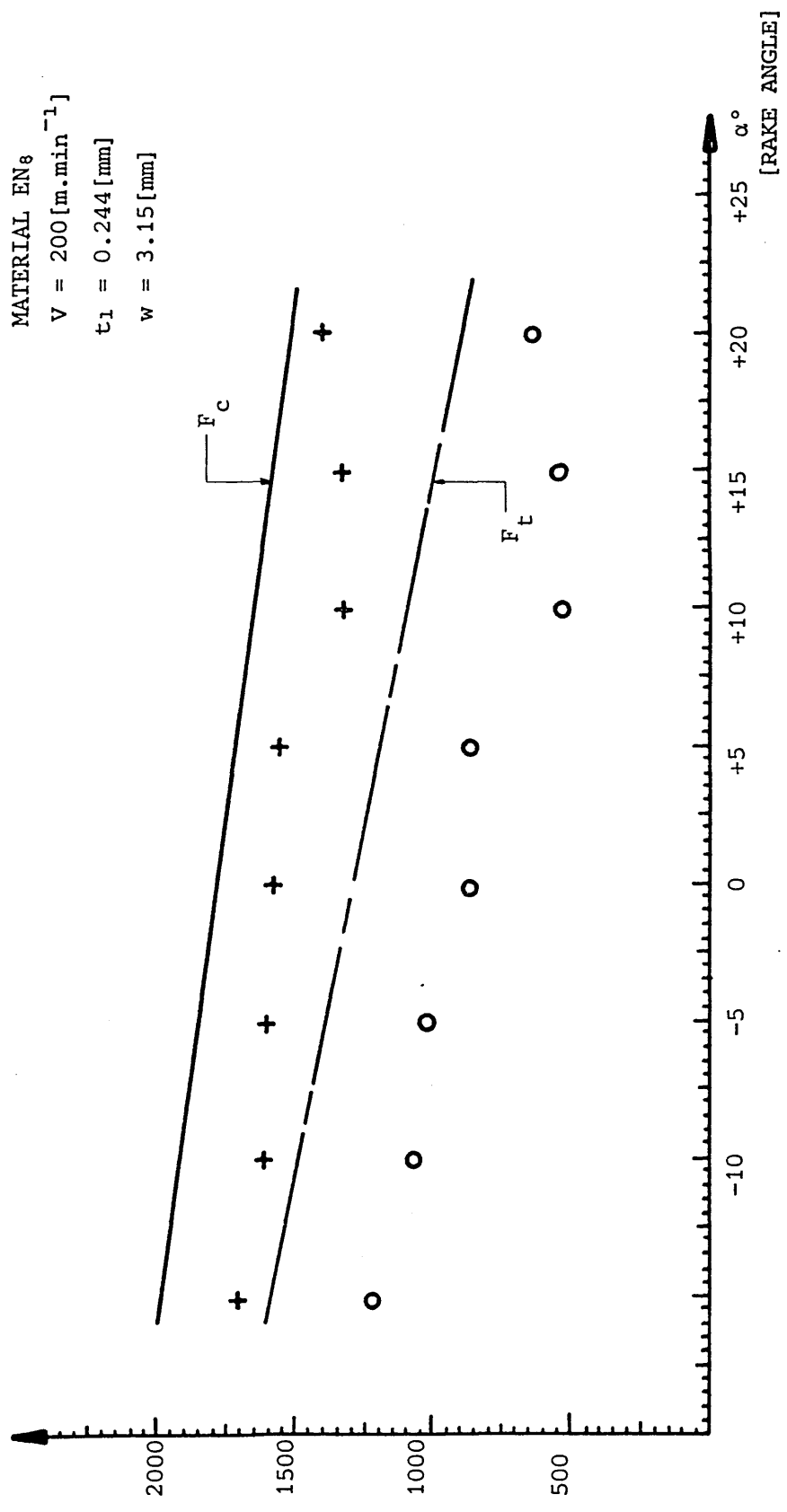


FIGURE 42 : Variation of cutting forces with a change in rake angle (+,o) results obtained from experiments

MATERIAL ALUMINIUM

$V = 200 \text{ [m.min}^{-1}\text{]}$

$t_1 = 0.244 \text{ [mm]}$

$w = 3.20 \text{ [mm]}$

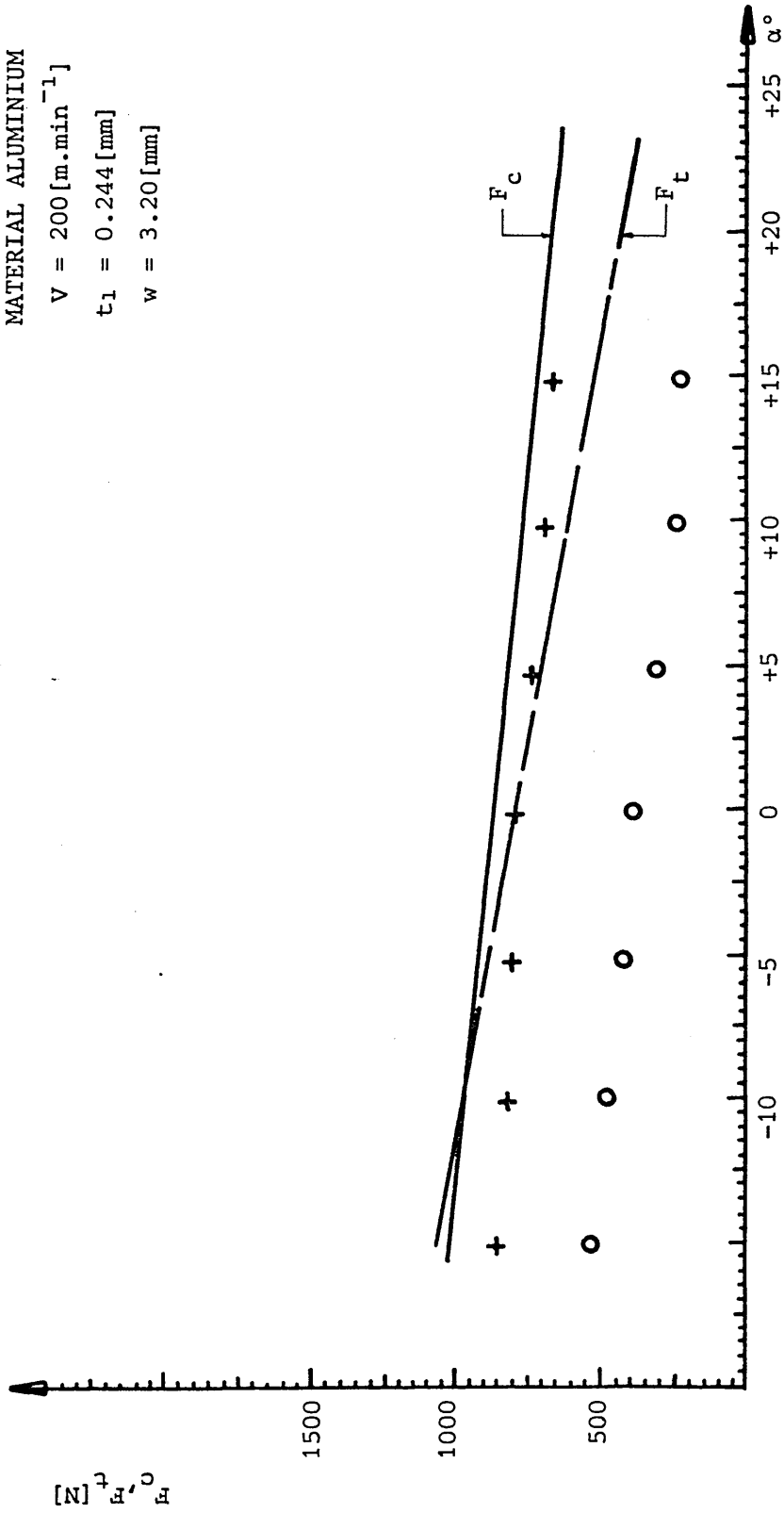


FIGURE 43 : Variation of the cutting forces with a change in rake angle (+,o) results obtained from experiments

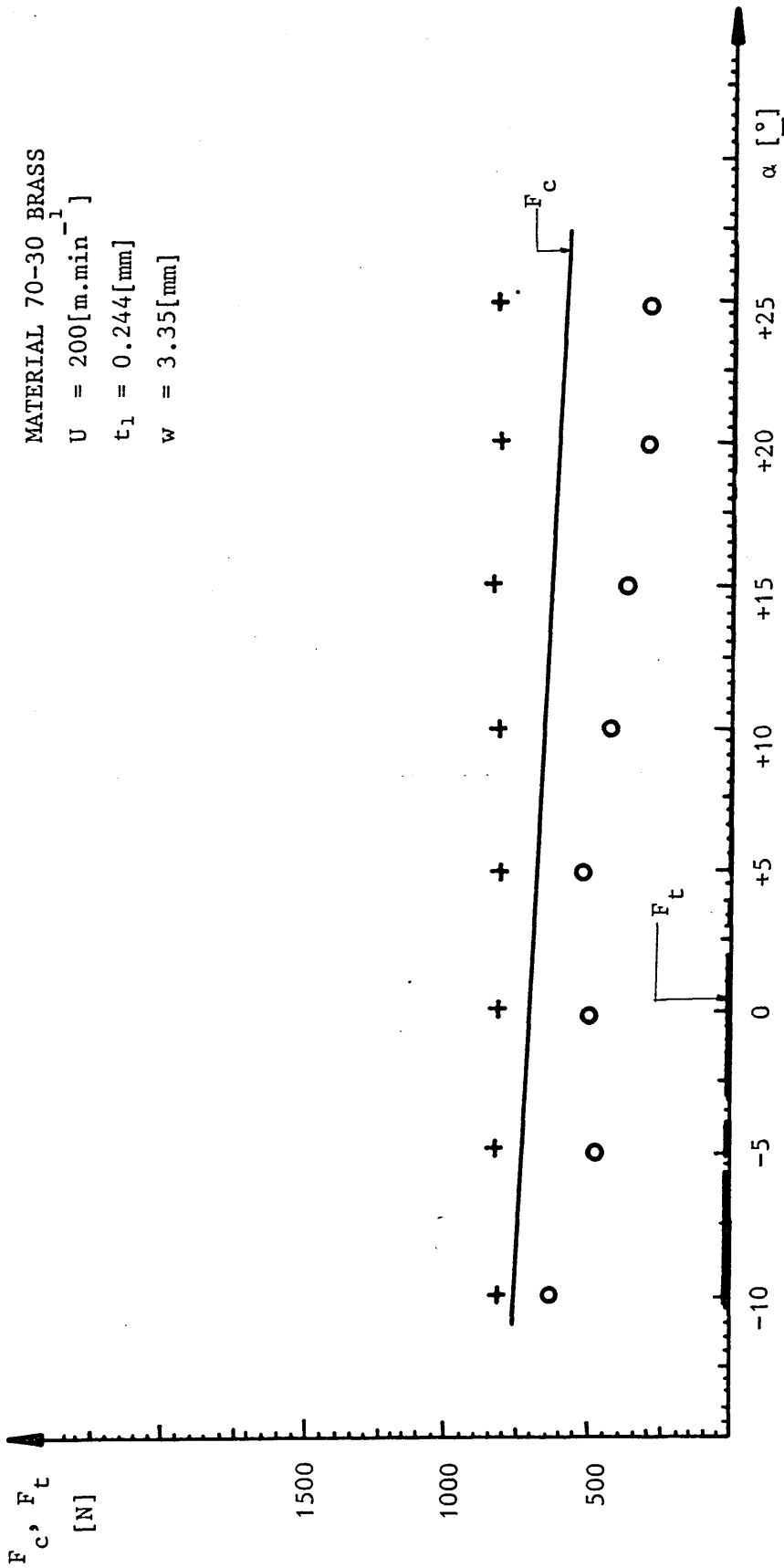


FIGURE 44 : Variation of the cutting forces with change in rake angle (+,o) results
obtained from experiments

o EN8
 Δ ALUMINIUM
 + 70-30 BRASS

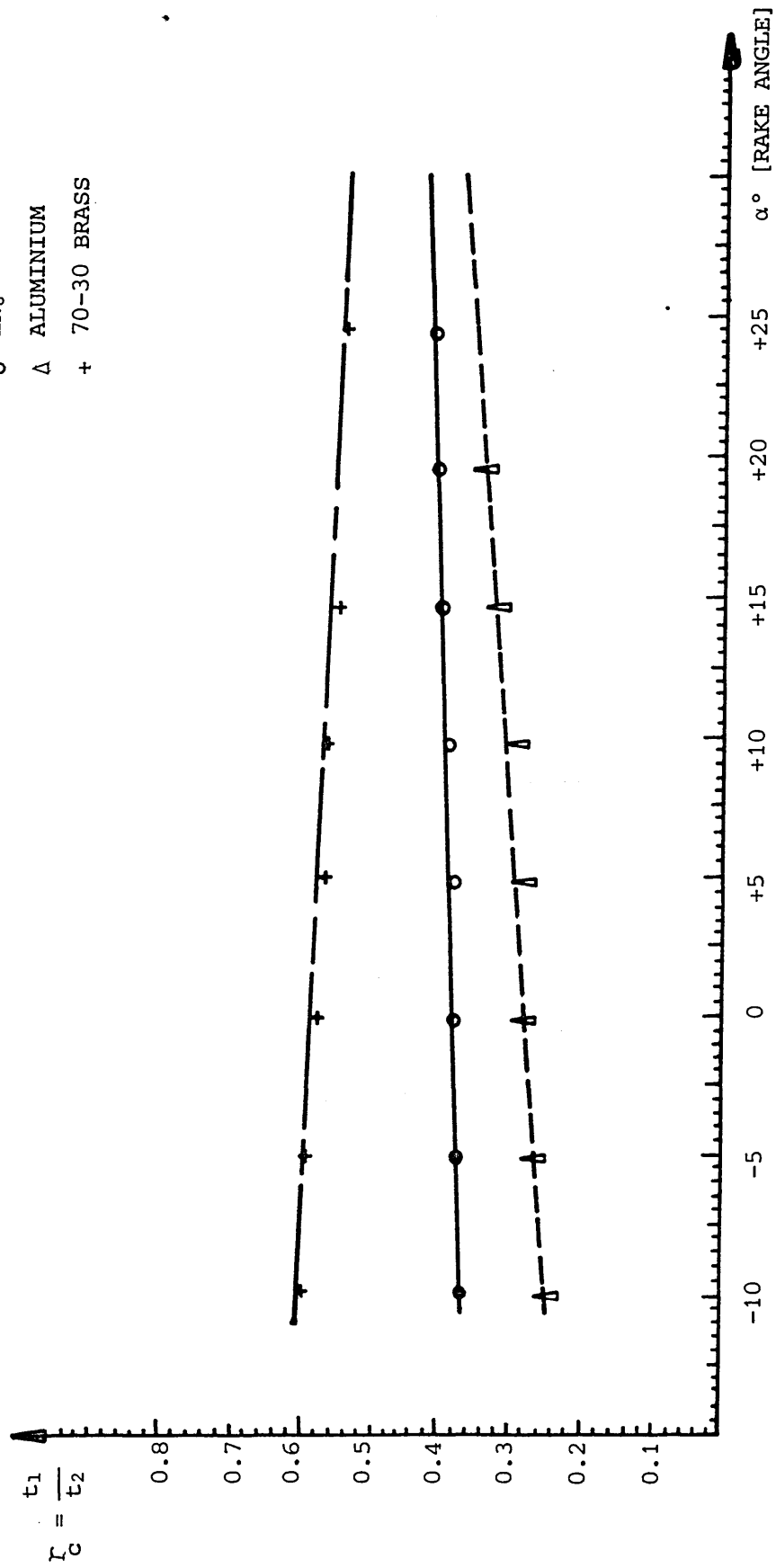


FIGURE 45 : Variation of the chip thickness ratio with a change in rake angle

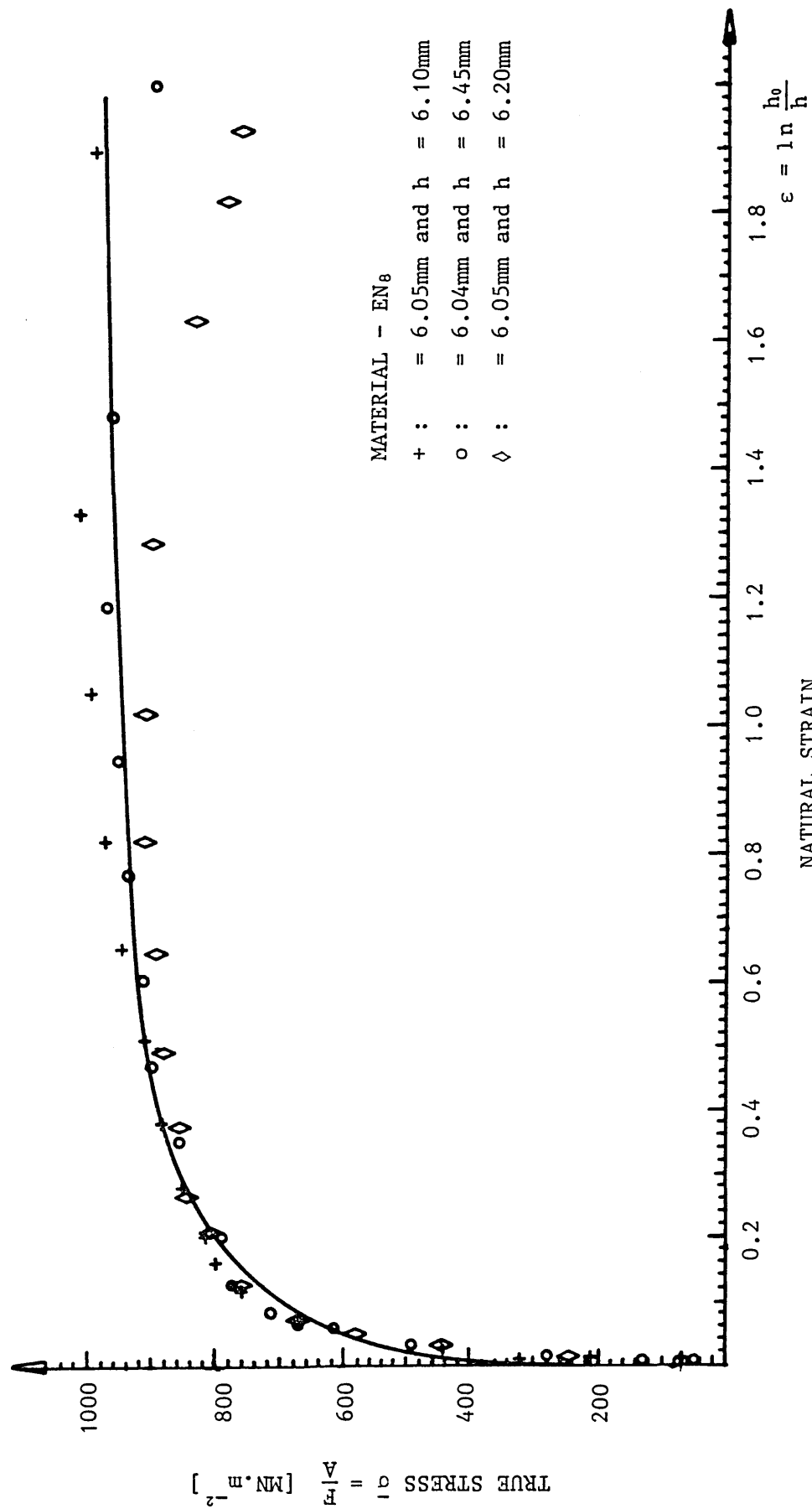


FIGURE 46 : True stress-strain curve for EN₈
 $(\sigma = 940\epsilon^{0.1})$

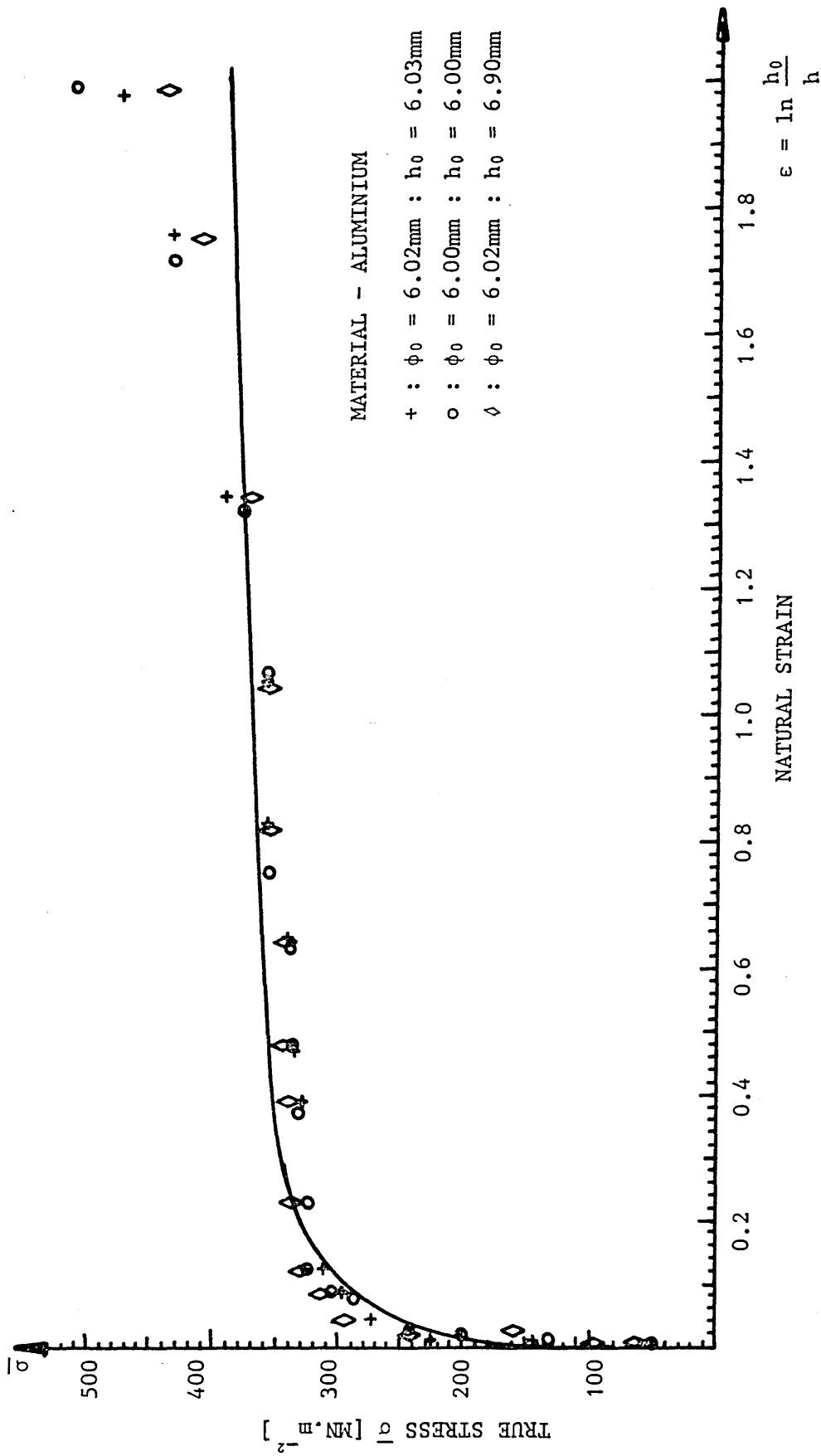


FIGURE 47 : True stress-strain curve for Aluminium
 ($\sigma = 360\epsilon^{0.09}$)

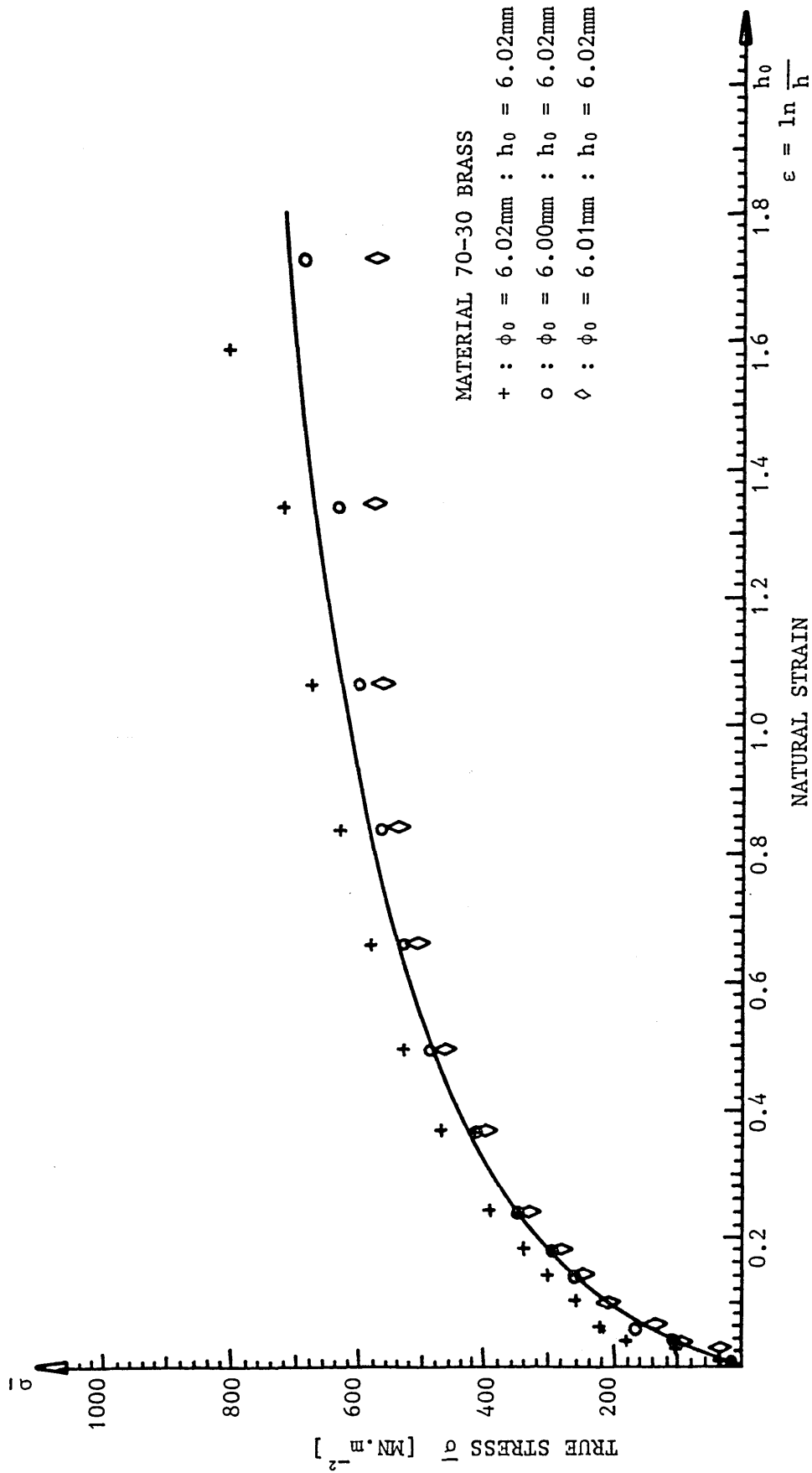


FIGURE 48 : True stress-strain curve for 70-30 Brass
 $(\sigma = 590 \epsilon^{0.33})$

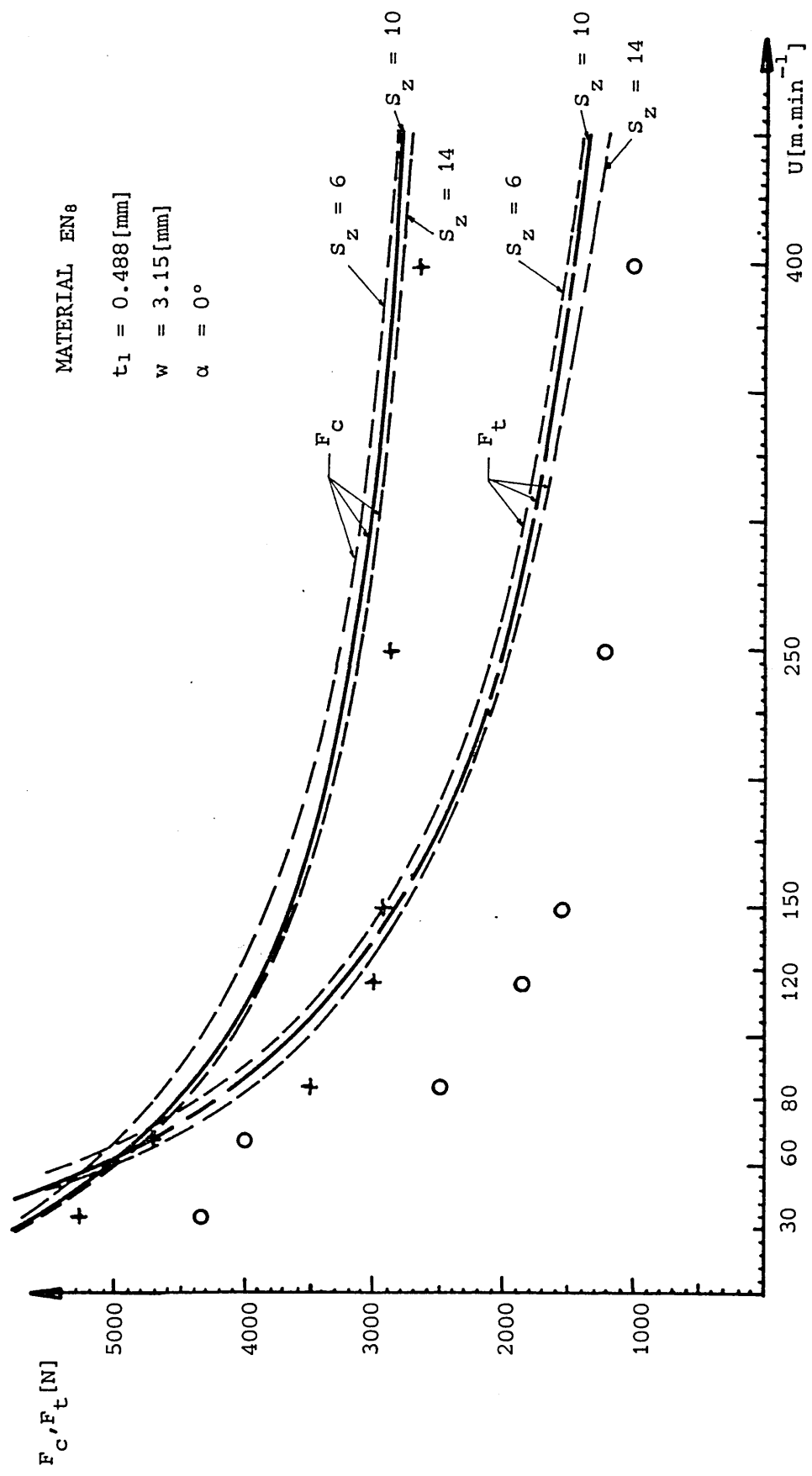


FIGURE 49 : Variation of the cutting forces with cutting speed

$$S_z = \frac{t_1}{\Delta S_1 \sin \phi} \quad (\text{LENGTH TO WIDTH RATIO})$$

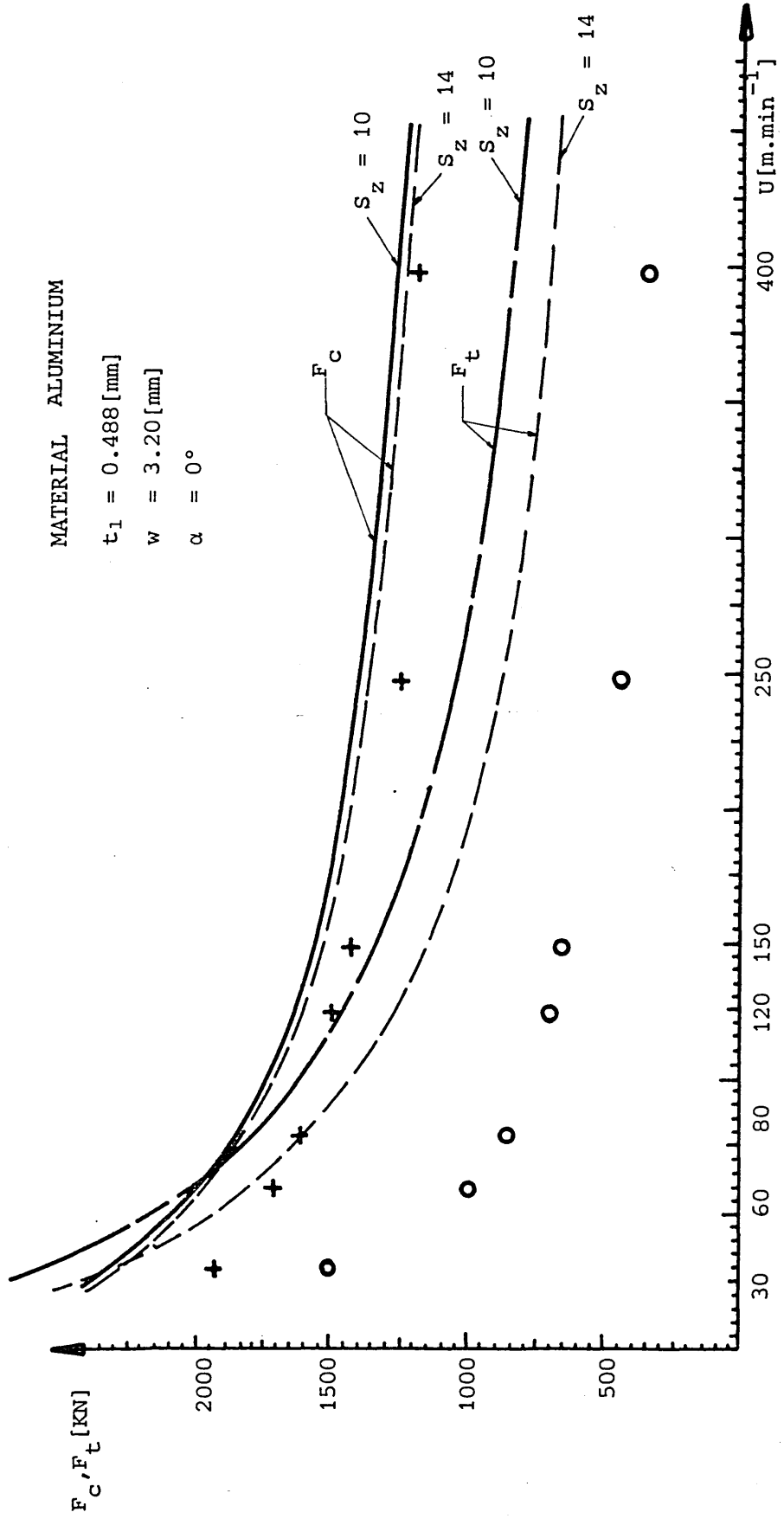


FIGURE 50 : Variation of the cutting forces with change in cutting speed

$$S_z = \frac{t_1}{\Delta S_1 \sin \phi} \quad (\text{LENGTH TO WIDTH RATIO})$$

MATERIAL 70-30 BRASS

$t_1 = 0.244$ [mm]

$w = 3.35$ [mm]

$\alpha = 0^\circ$

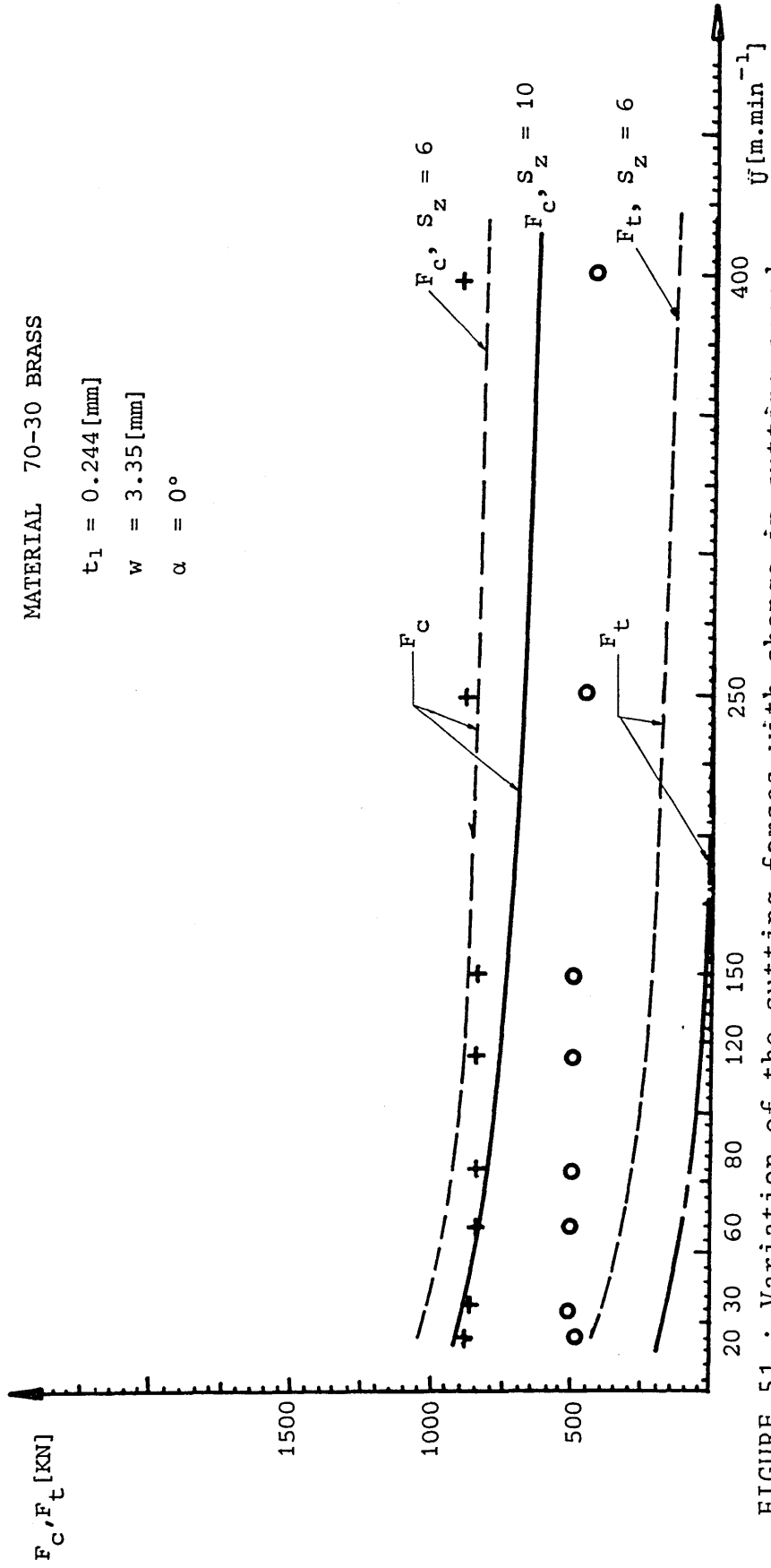


FIGURE 51 : Variation of the cutting forces with change in cutting speed

$$S_z = \frac{t_1}{\Delta S_1 \sin \phi} \quad (\text{LENGTH TO WIDTH RATIO})$$

MATERIAL . 70-30 BRASS

$V = 200 [\text{m.min}^{-1}]$

$w = 3.35 [\text{mm}]$

$\alpha = 0^\circ$

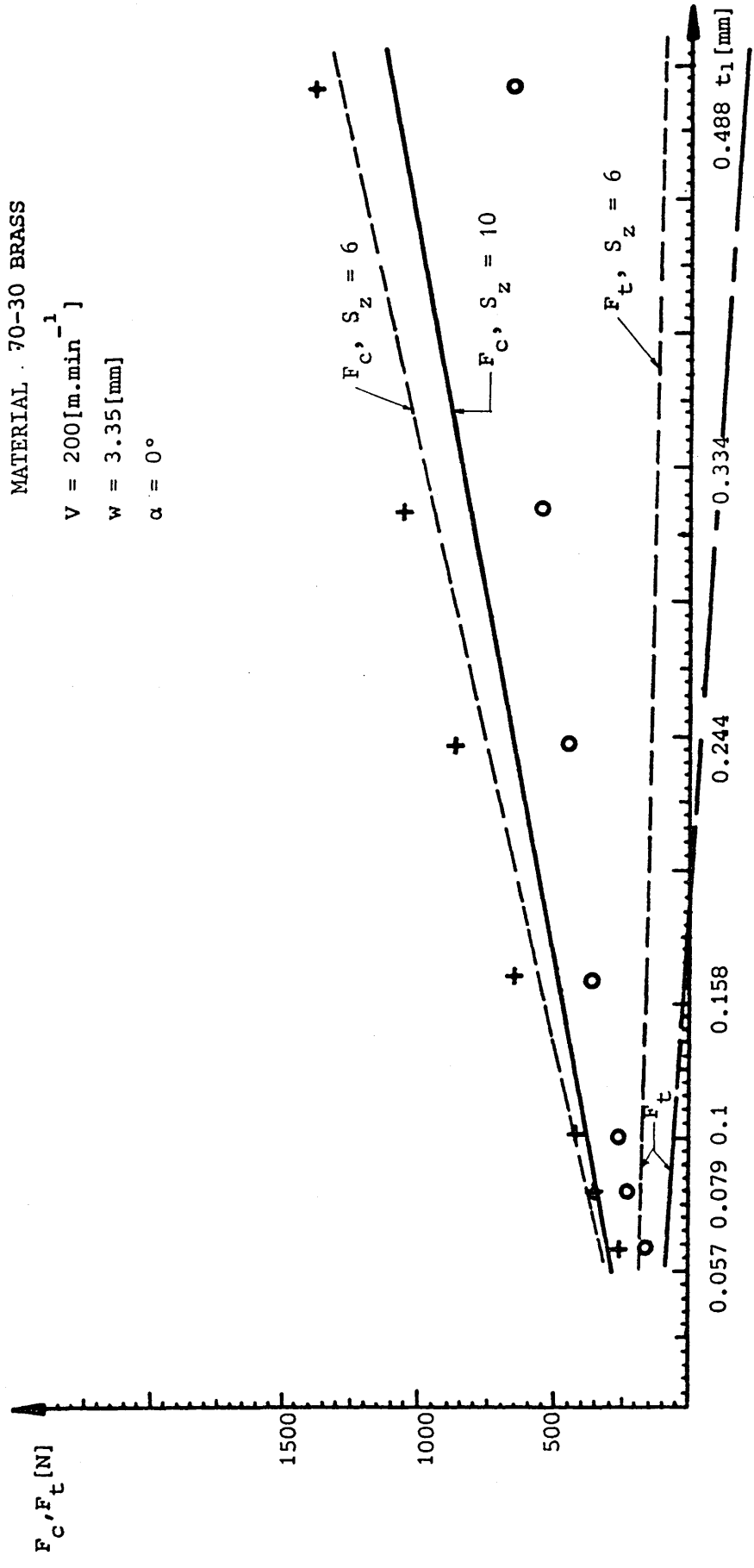


FIGURE 52 : Variation of cutting forces with change in the undeformed chip thickness

$$S_z = \frac{t_1}{\Delta S_1 \sin \phi} \quad (\text{LENGTH TO WIDTH RATIO})$$

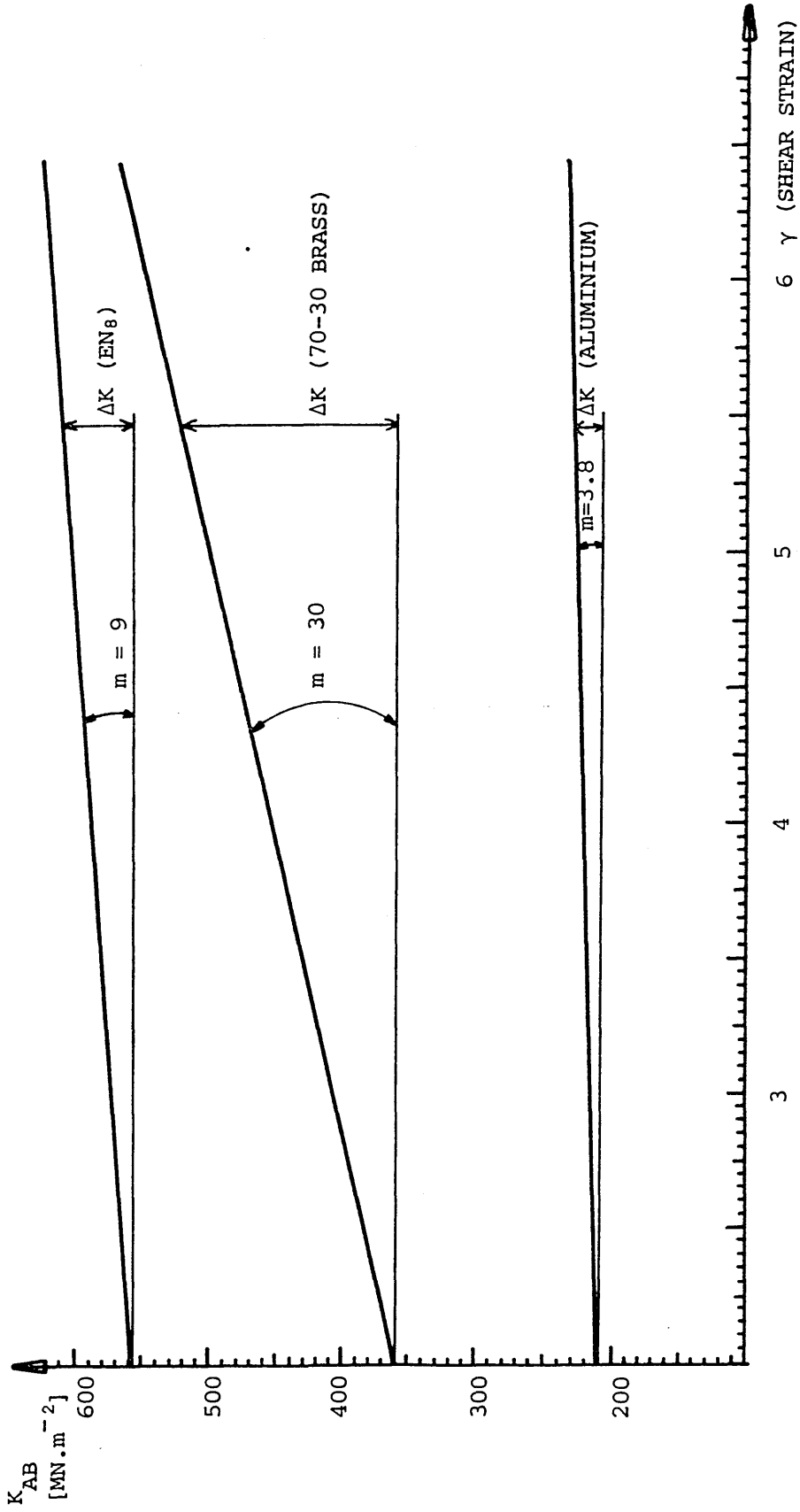


FIGURE 53 : Variation of the shear flow stress with shear strain

$$m = \frac{\Delta K}{\gamma}$$

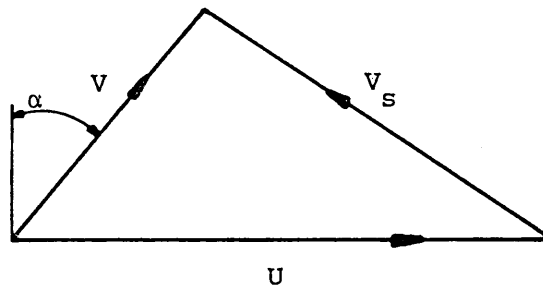
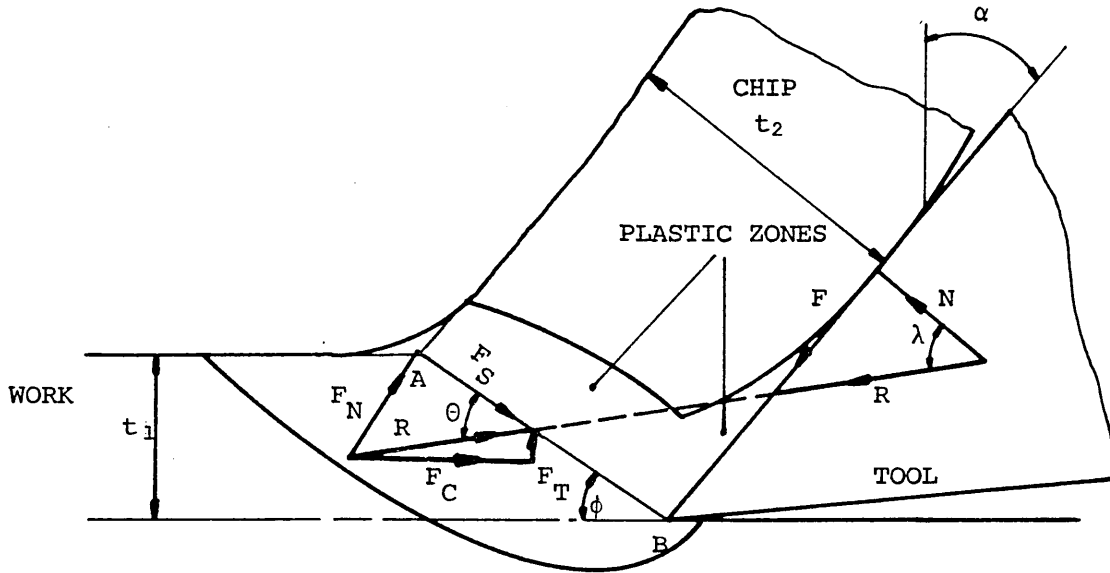


FIGURE 54 : Model of chip formation

Ref [47]

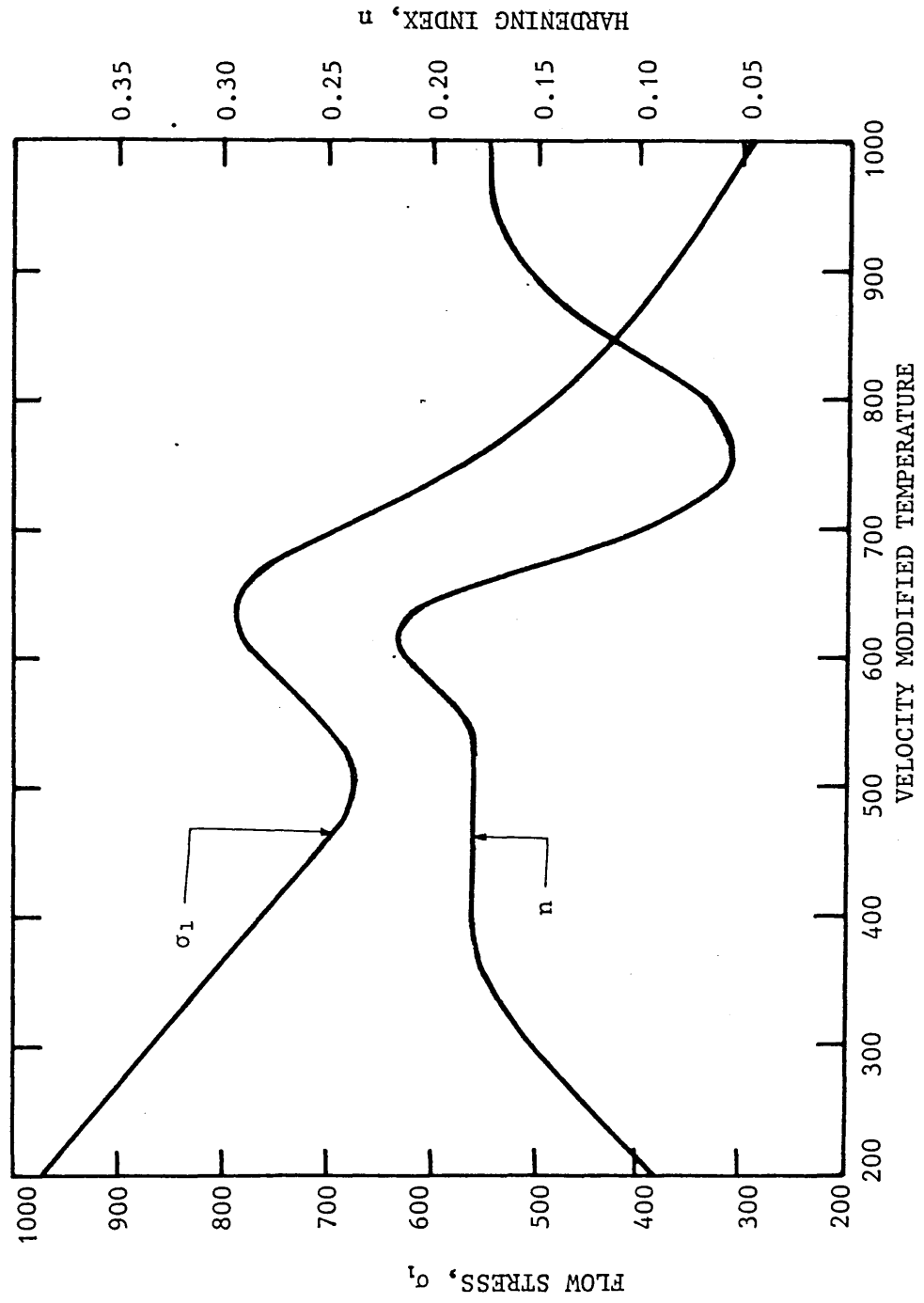


FIGURE 55 : Flow stress (σ_1) and strain hardening index (n) variations with velocity modified temperature
 Ref [50]

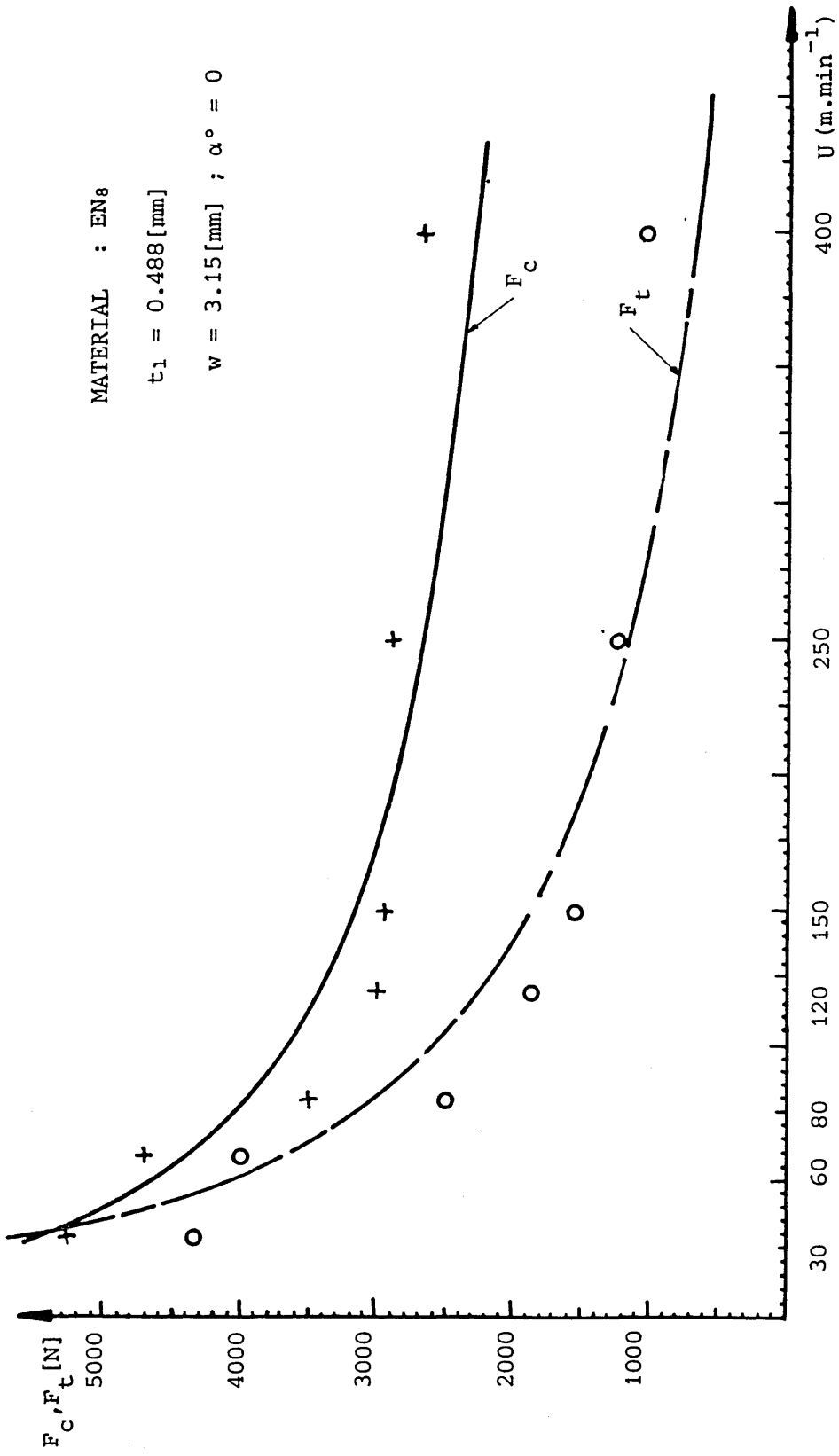


FIGURE 56 : Variation of cutting forces with cutting speed (+,0) results obtained from experiments

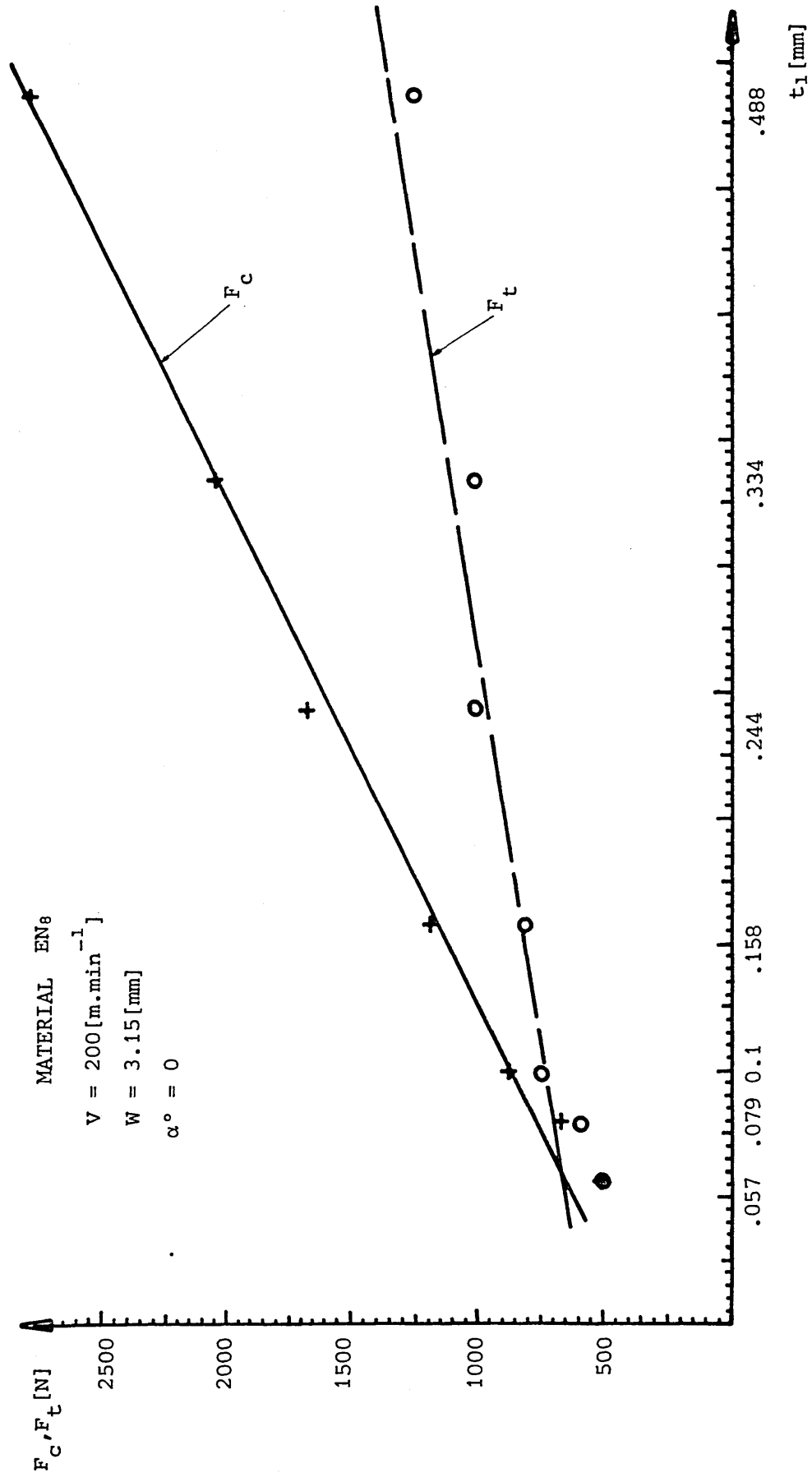


FIGURE 57 : Variation of cutting forces with the undeformed chip thickness (+,0) results obtained from experiments

MATERIAL EN8

$V = 200 \text{ [m.min}^{-1}\text{]}$

$t_1 = .244 \text{ [mm]}$

$W_0 = 3.15 \text{ [mm]}$

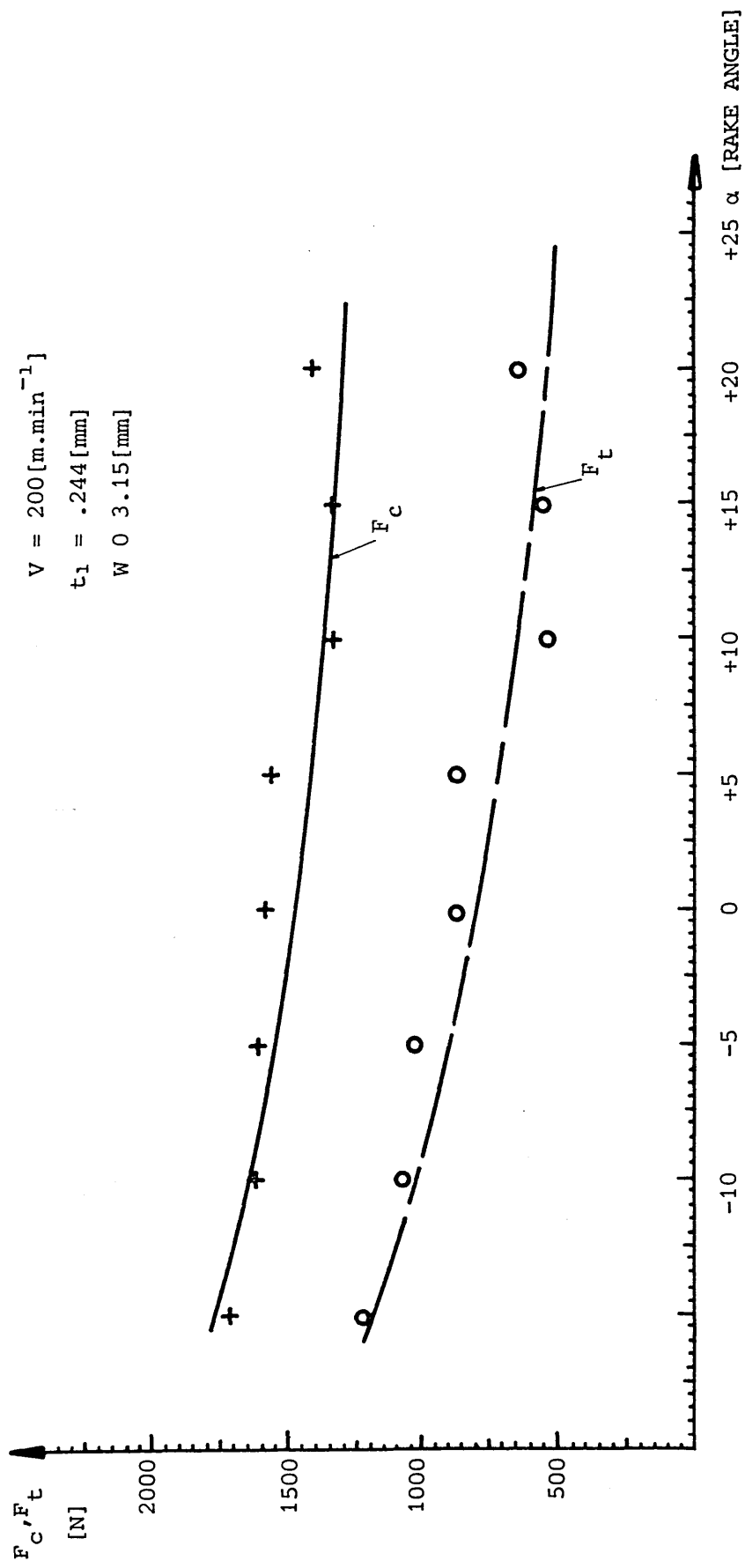


FIGURE 58 : Variation of the cutting forces with change in rake angle (+,0) results obtained from experiments

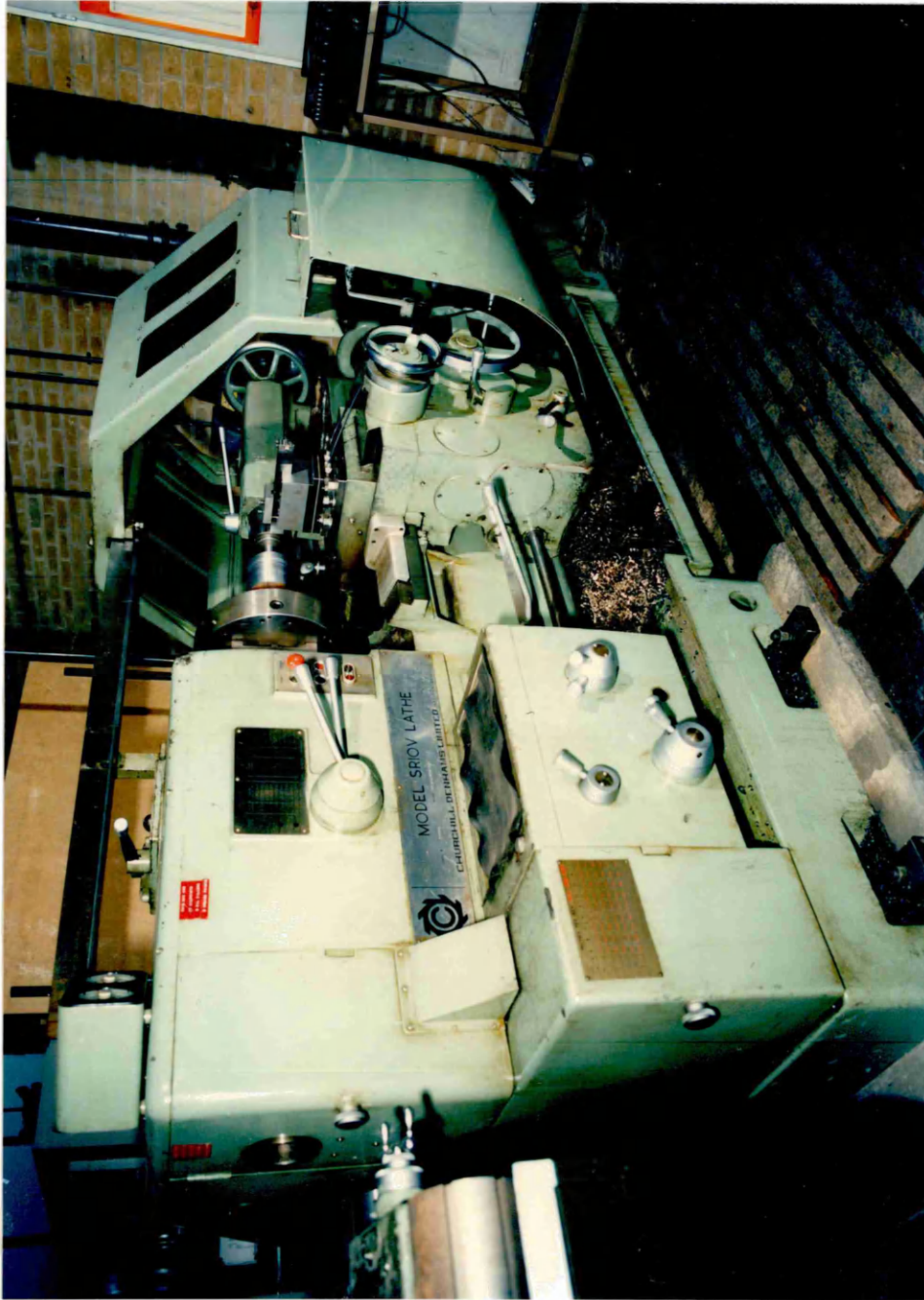


PLATE 1 : LATHE USED IN THE EXPERIMENTS

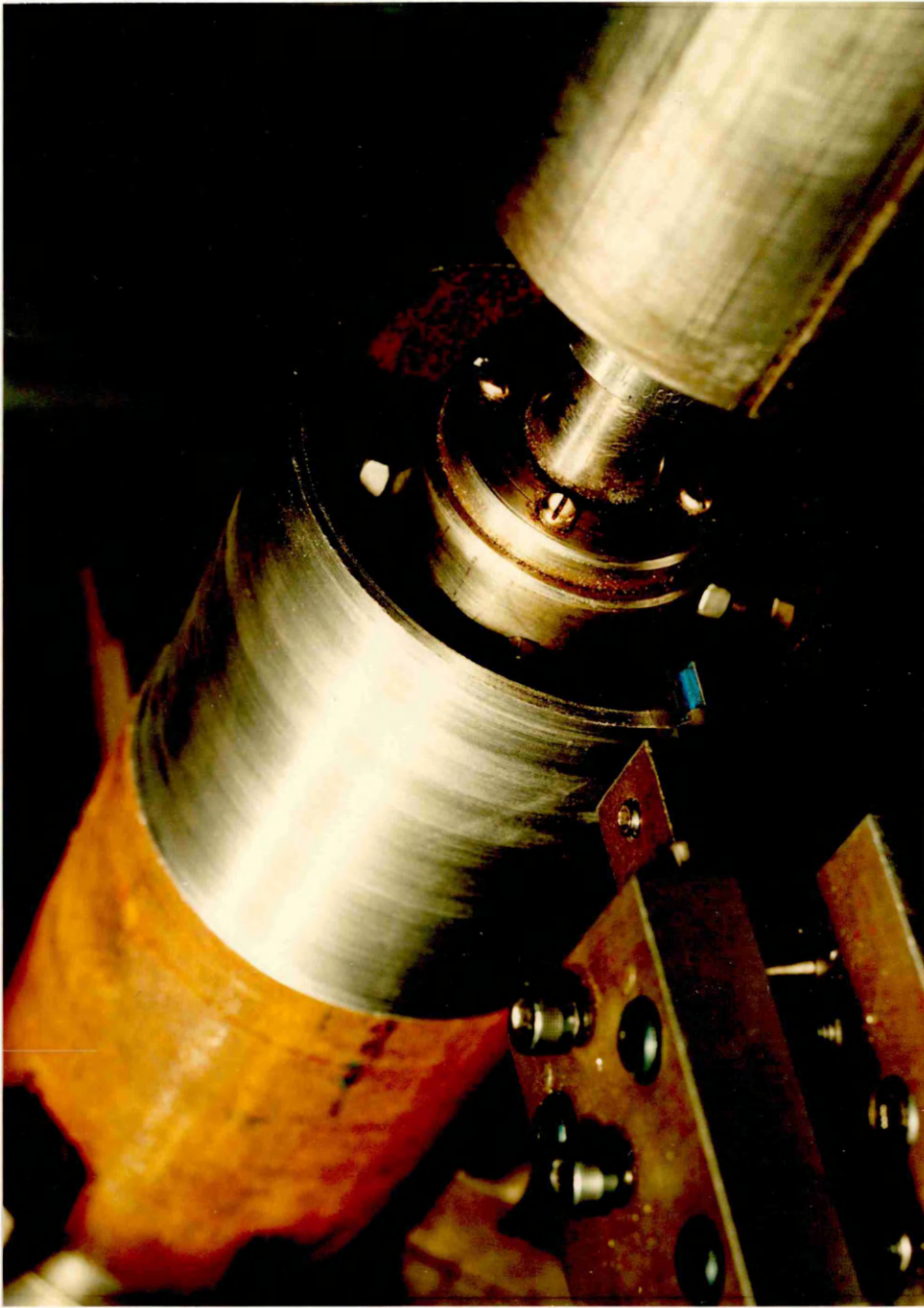


PLATE 2 : EXPERIMENTAL SET-UP FOR ORTHOGONAL MACHINING

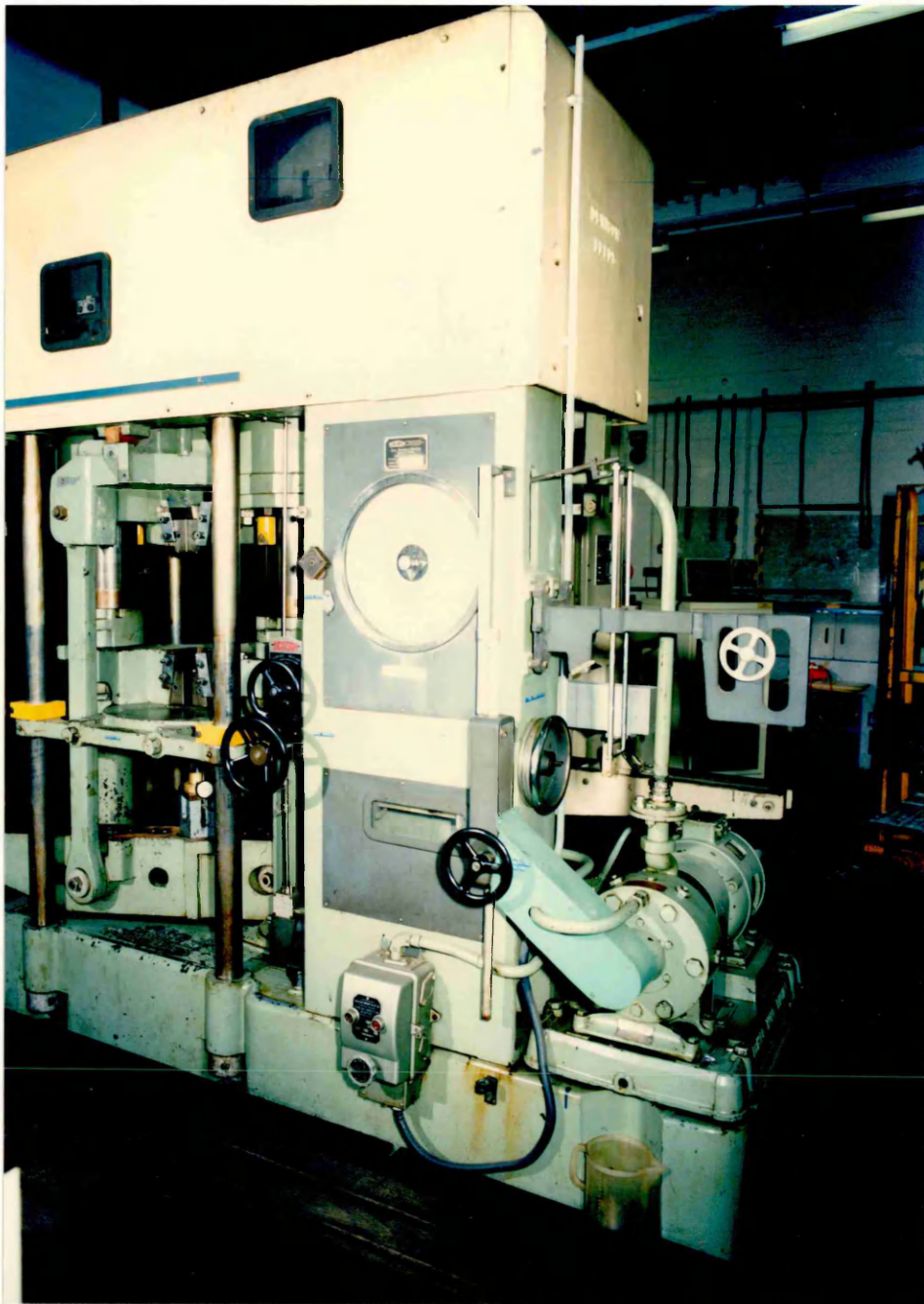


PLATE 3 : DENISON UNIVERSAL TESTING MACHINE

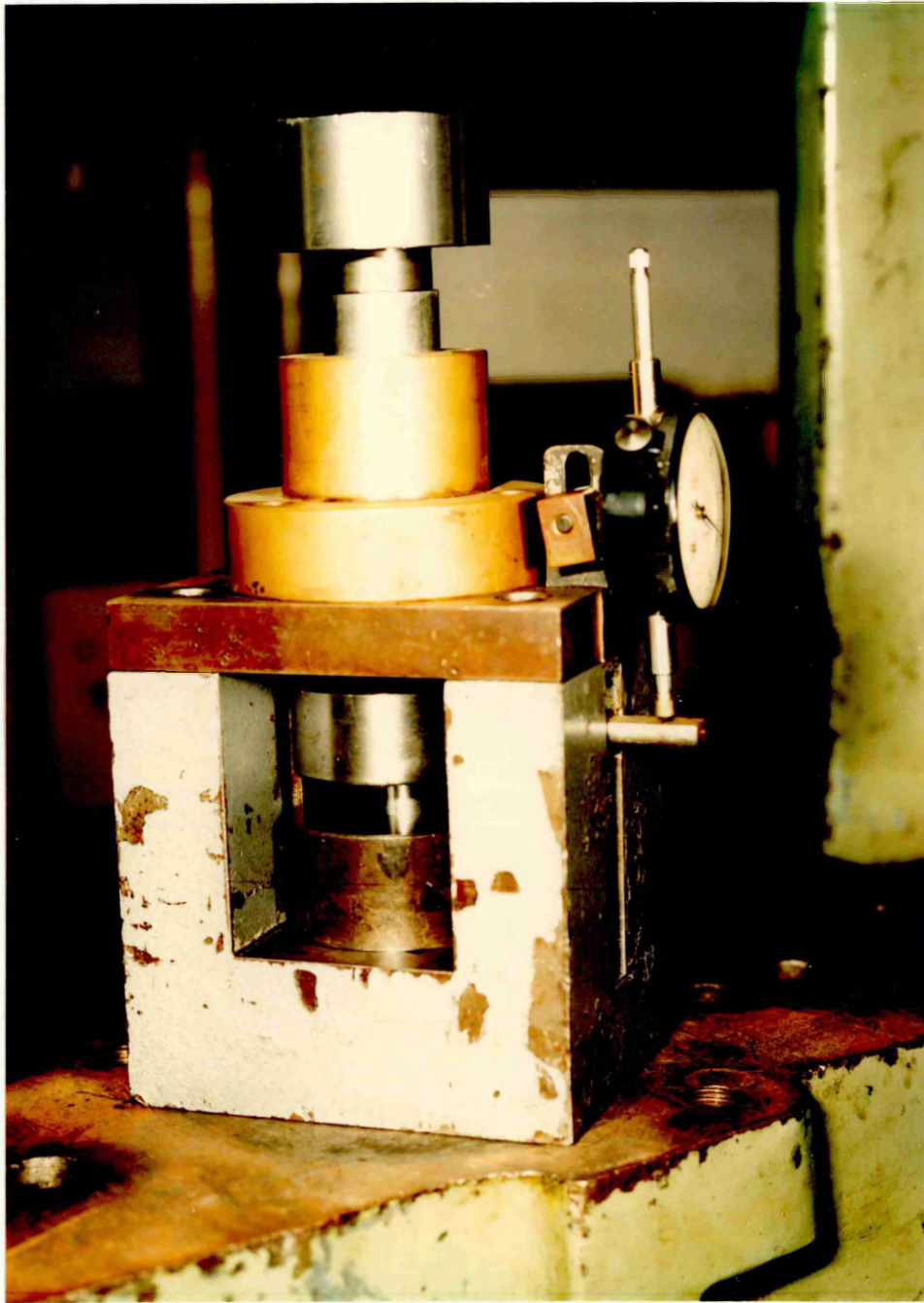


PLATE 4 : (1) PARALLEL PLATENS
 (2) CYLINDRICAL SPECIMEN

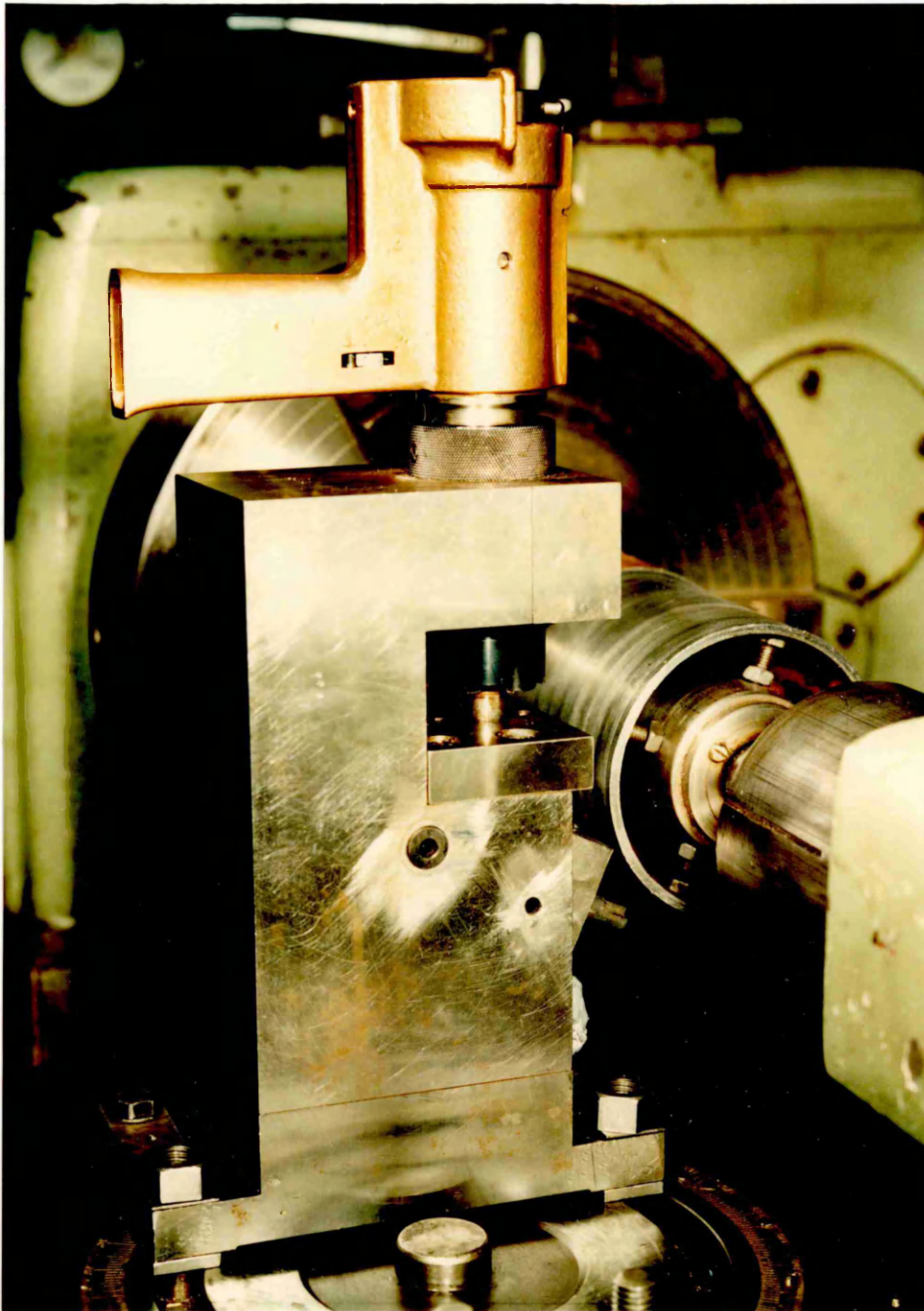


PLATE 6 : QUICK STOP DEVICE MOUNTED ON THE LATHE

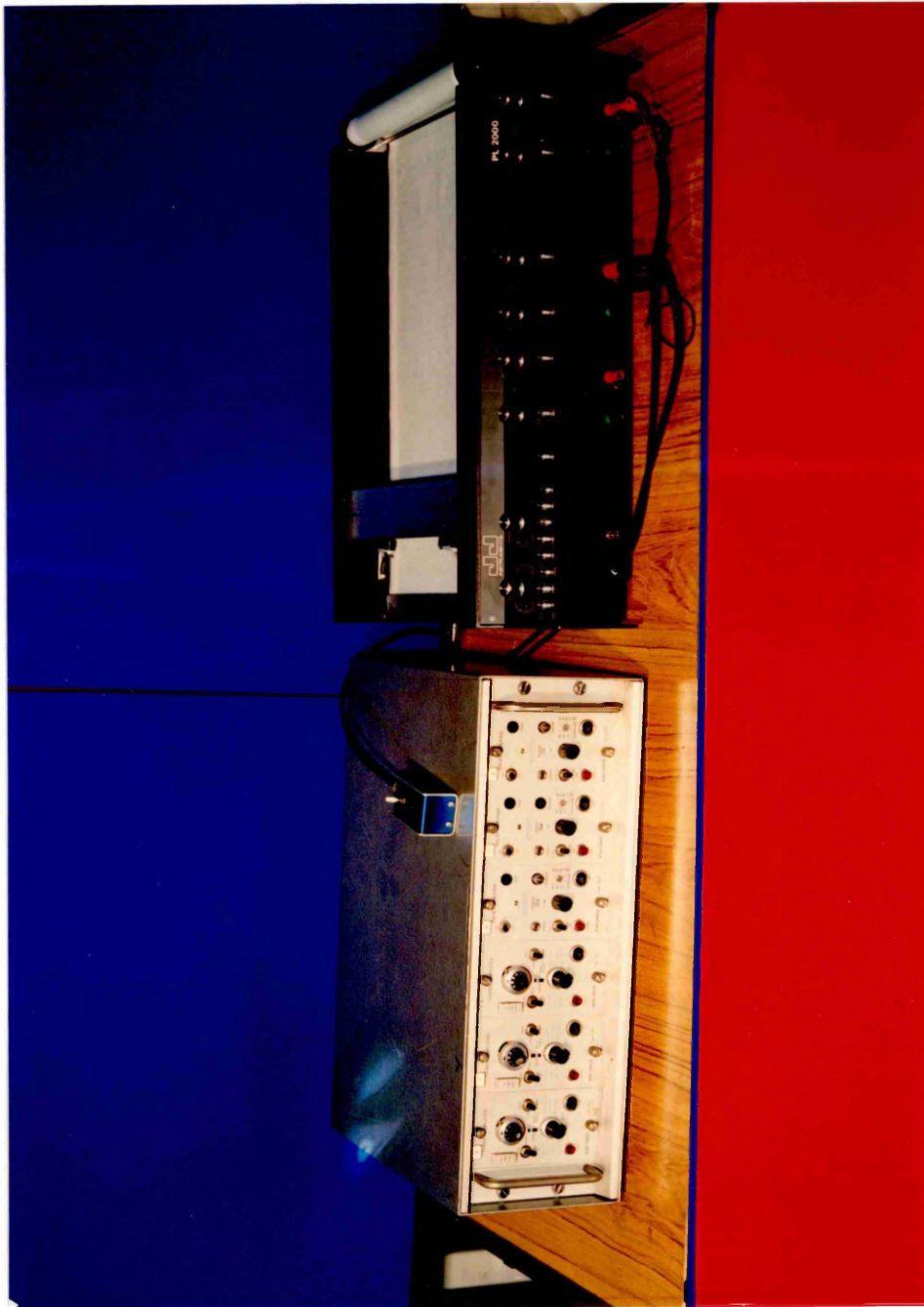


PLATE 7 : AMPLIFIER AND UV RECORDER USED WITH

DYNAMOMETER DURING FORCE MEASUREMENT

(1) Amplifier

(2) Platform recorder

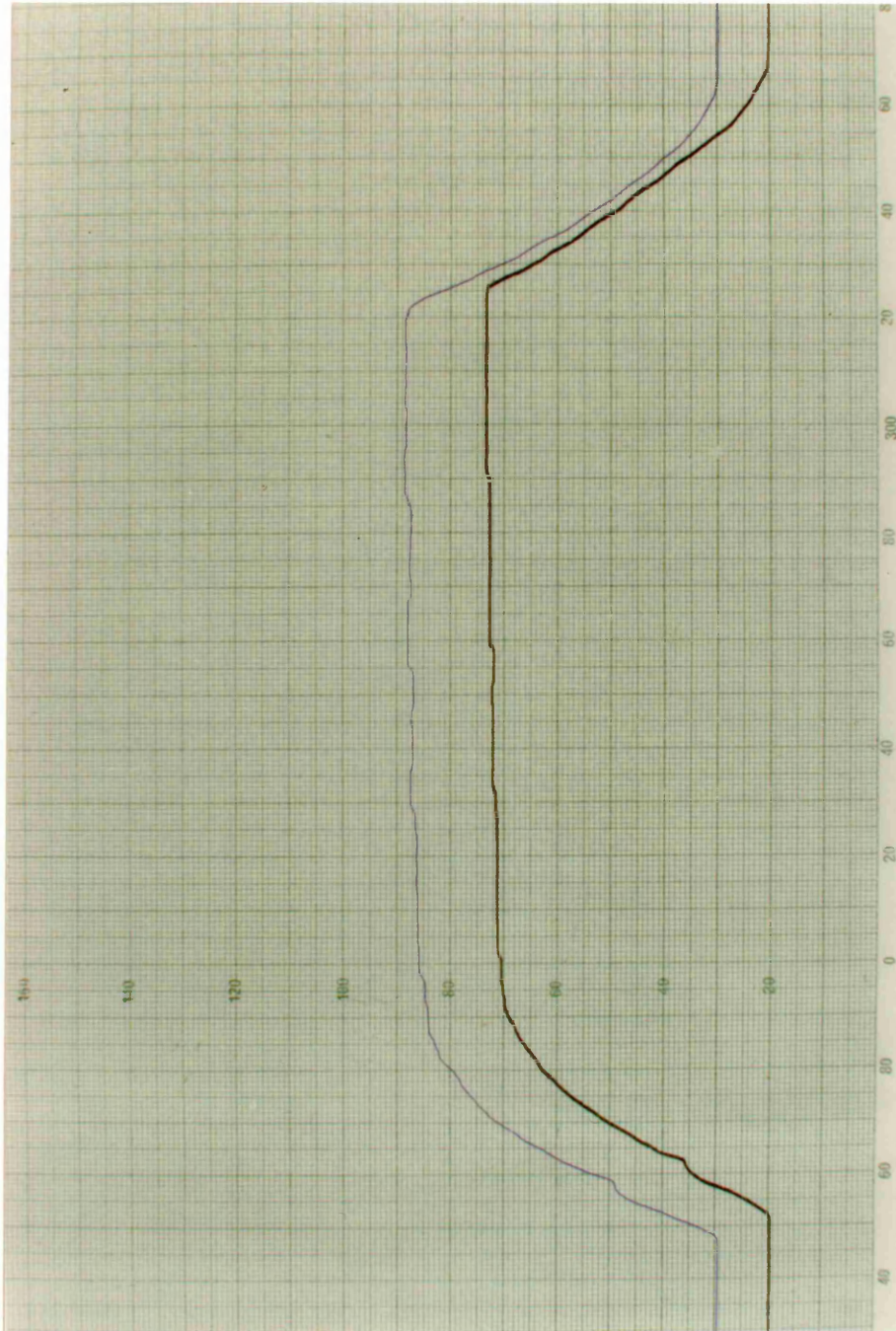


PLATE 8 : TRACES OF THE CUTTING FORCES

- (1) Horizontal Cutting Force " F_c "
- (2) Vertical Force " F_t "

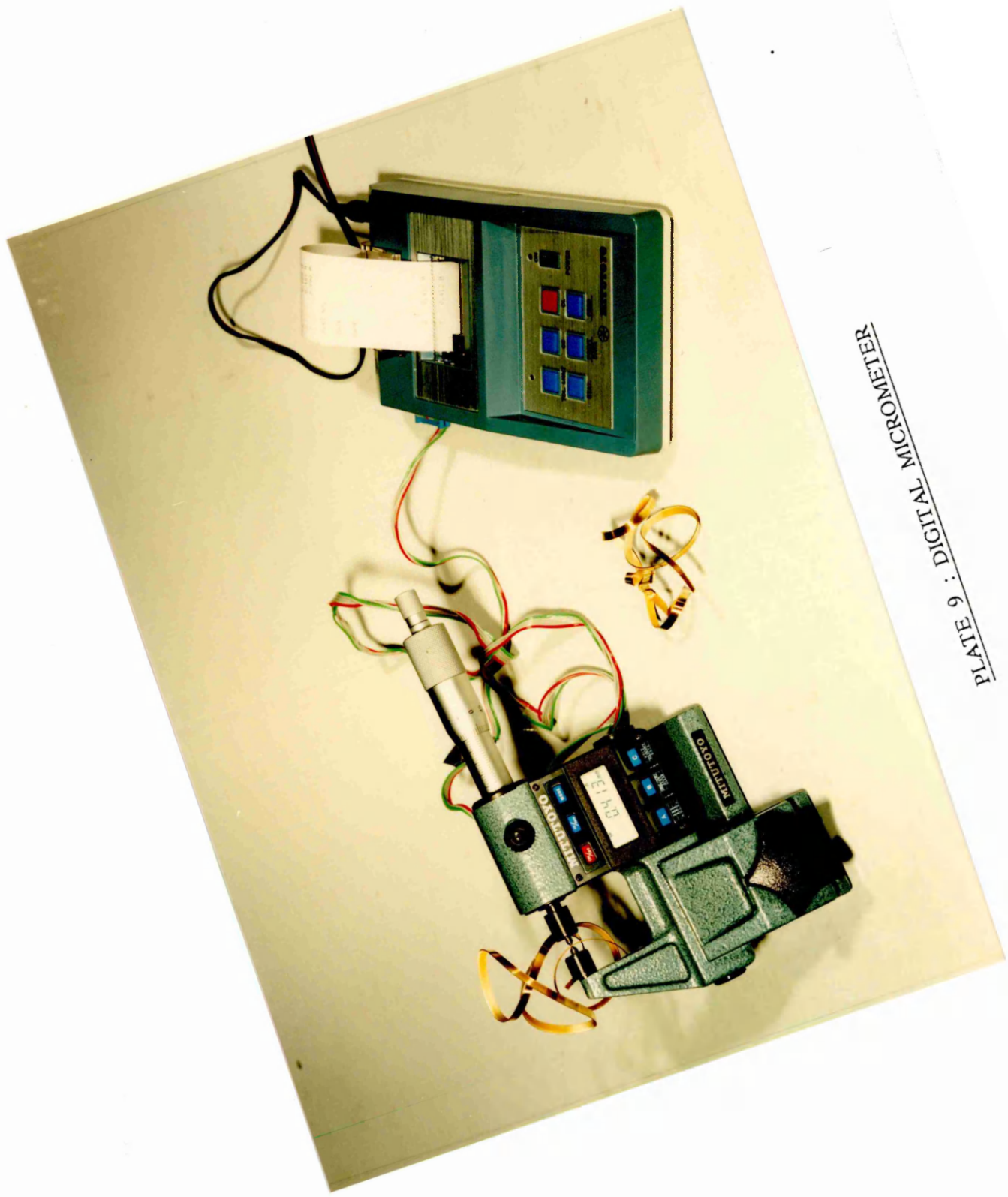


PLATE 9 : DIGITAL MICROMETER



PLATE 10 : DIGITAL MICROMETER AND ITS EQUIPMENT

- (1) Digital micrometer
- (2) Digital mini-processor
- (3) AC adaptor
- (4) Connector wire
- (5) Chip

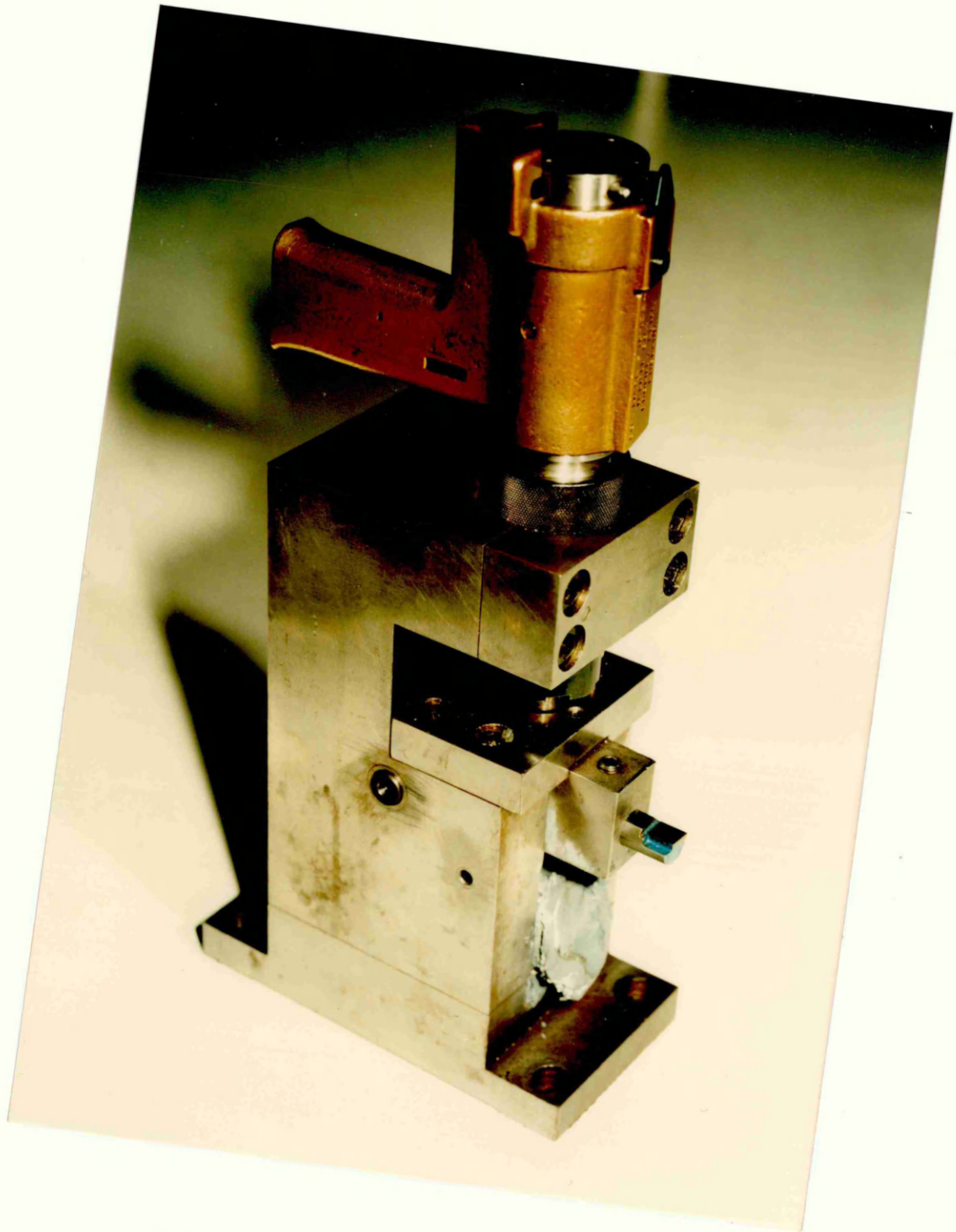


PLATE 11 : QUICK STOP DEVICE

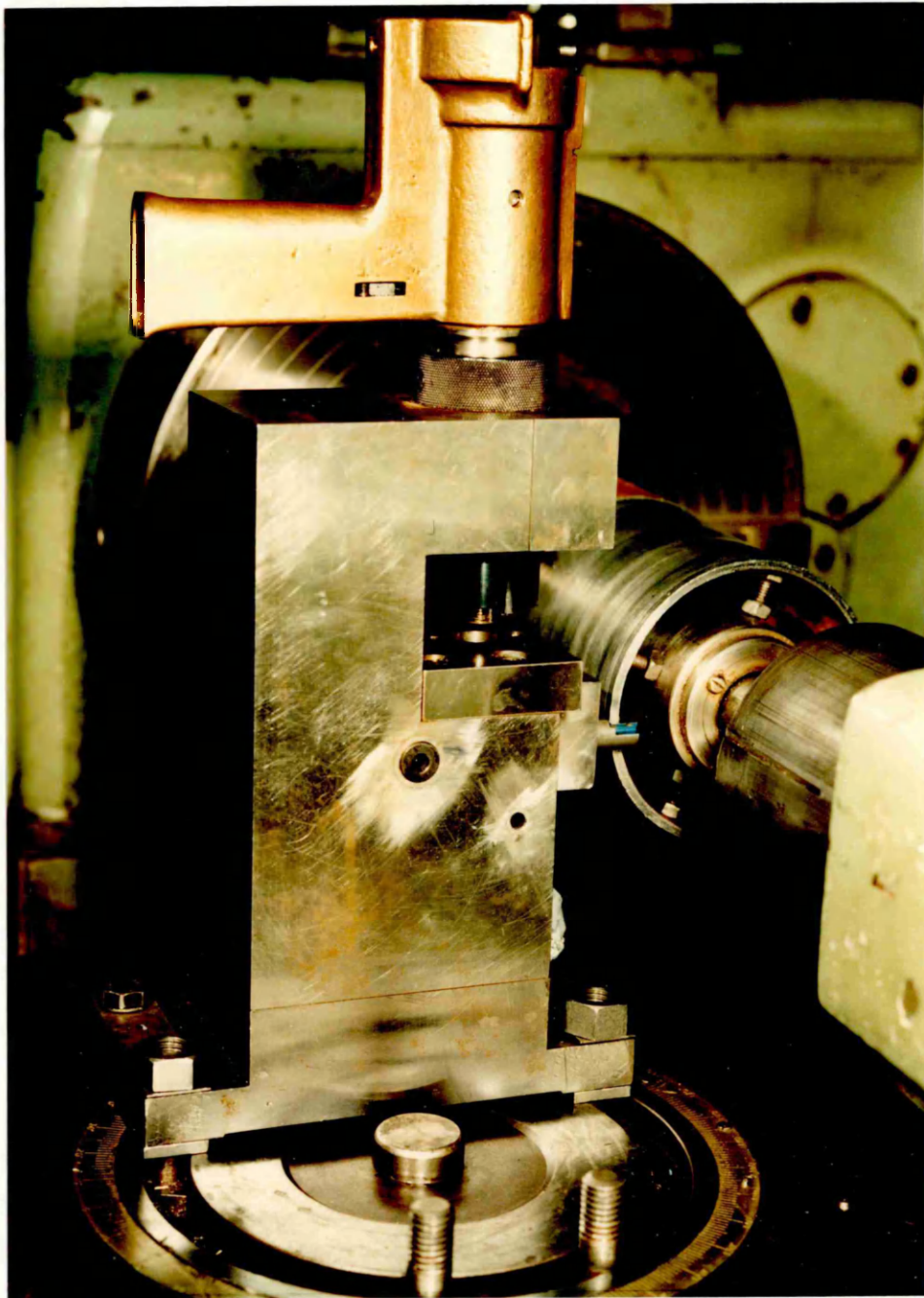


PLATE 12 : QUICK STOP DEVICE MOUNTED ON THE CROSS-SLIDE OF
THE LATHE

(1) Tubular workpiece

(2) Quick stop

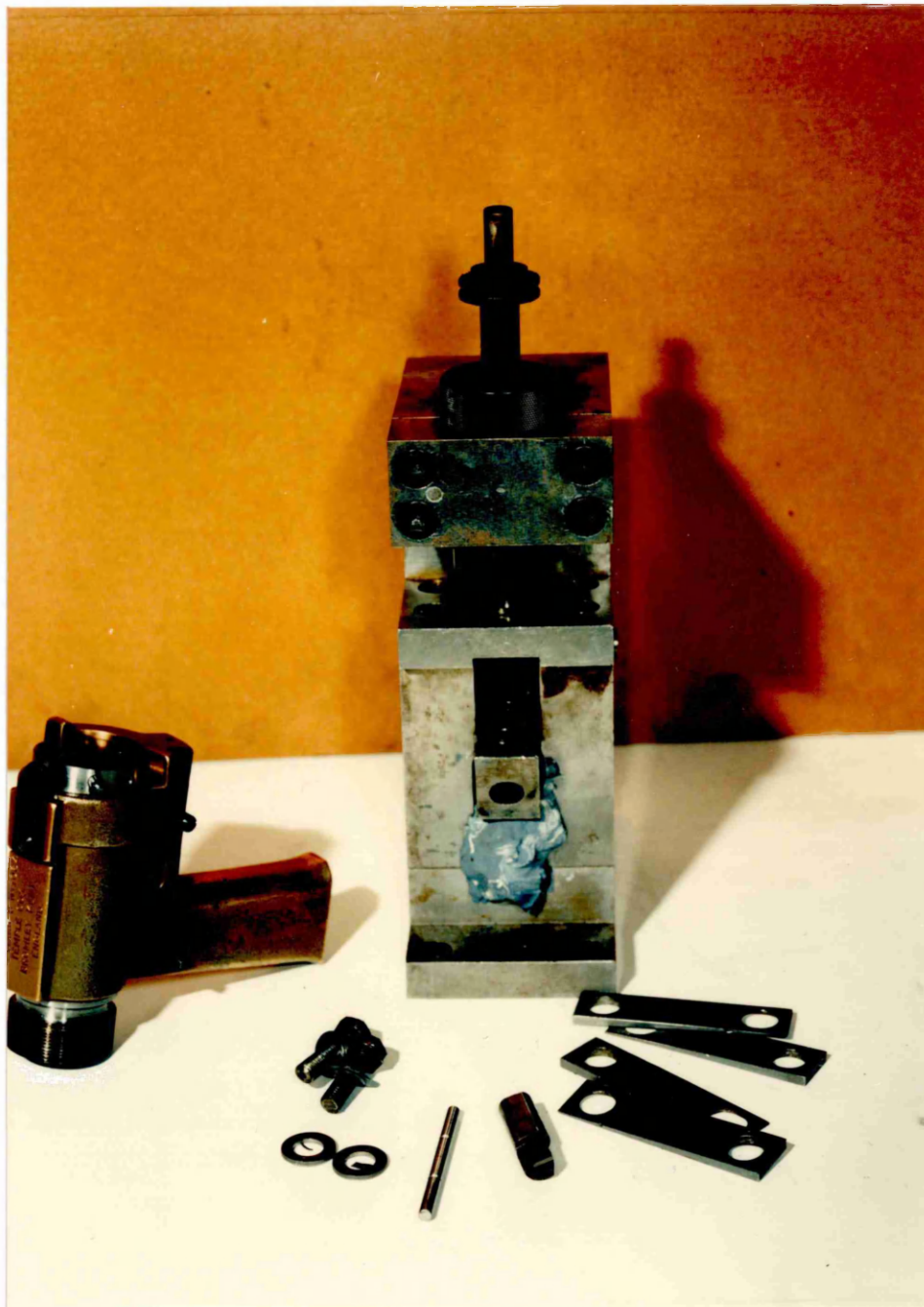


PLATE 13 : QUICK STOP AND ACCESSORIES

- (1) Human killer gun
- (2) Quick stop body
- (3) Standard spacers
- (4) Shear pins
- (5) Machined surface and chip root

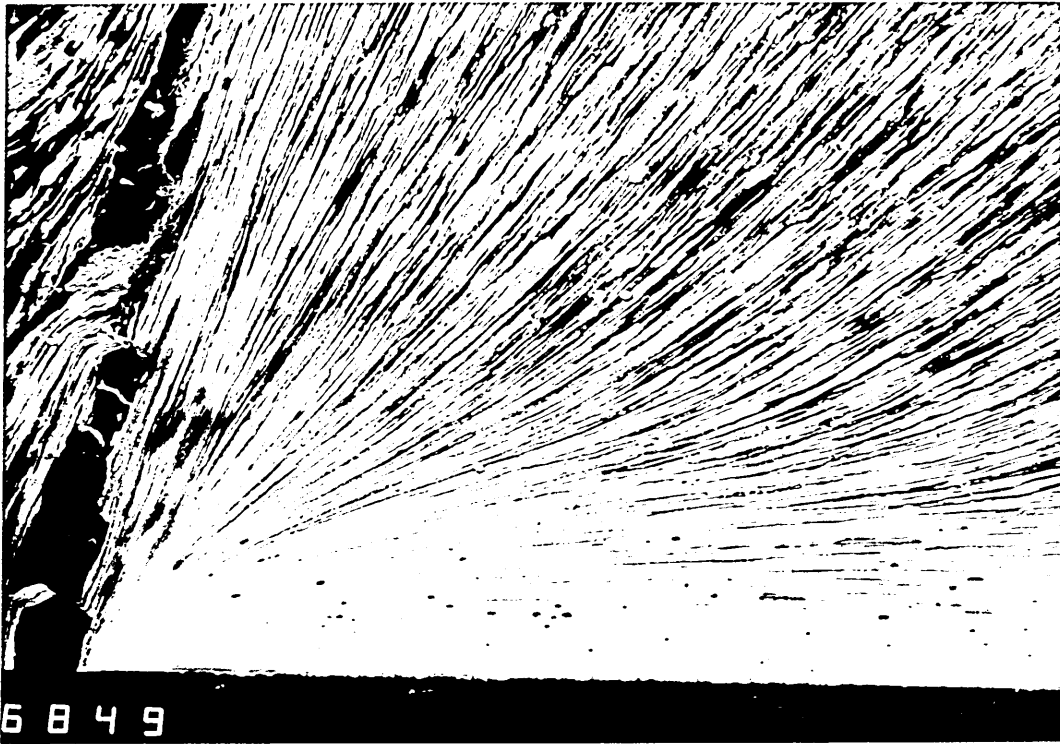


PLATE 14 : BUILT-UP-EDGE HEIGHT AT SPEED $U = 30$ [m.min⁻¹]
Magnification (200×0.85)



PLATE 15 : BUILT-UP-EDGE HEIGHT AT SPEED $U = 60$ [m.min⁻¹]
Magnification (200×0.8)

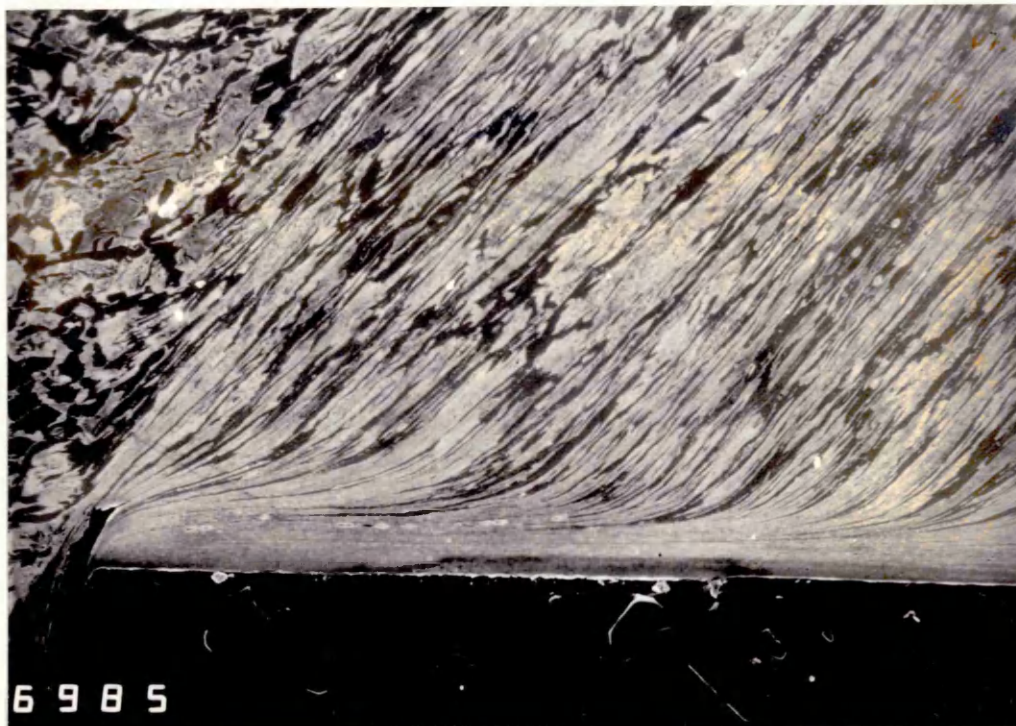


PLATE 16 : BUILT-UP-LAYER HEIGHT AT SPEED $U = 60[m.min^{-1}]$

Magnification (200×0.8)

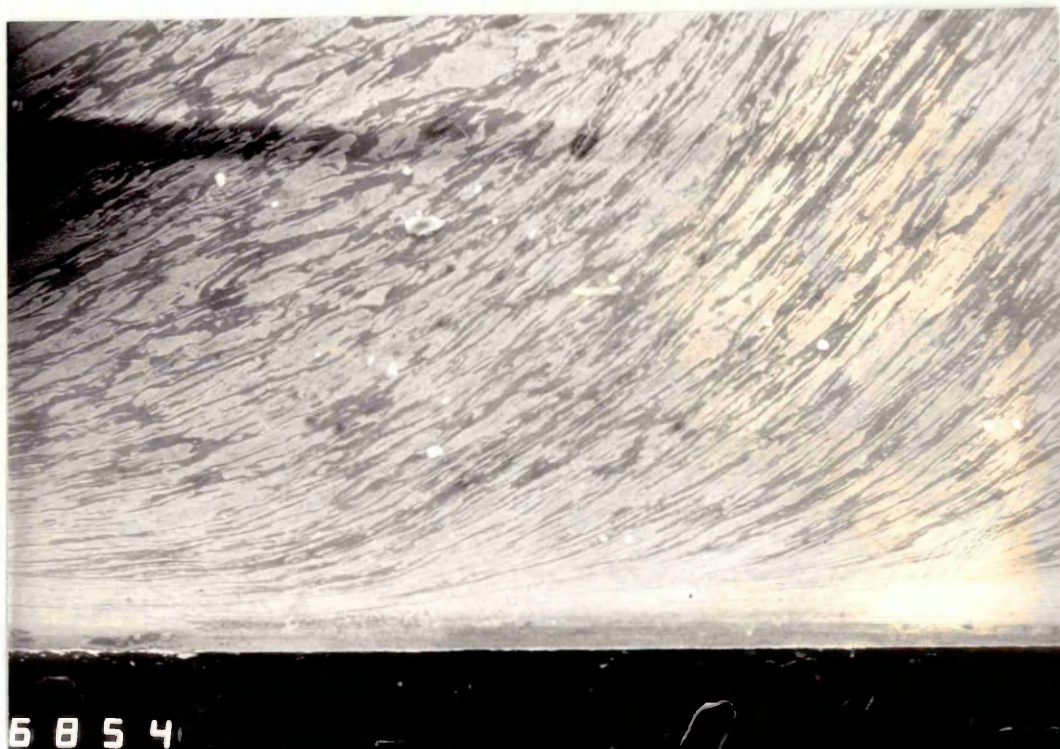


PLATE 17 : BUILT-UP-LAYER AT SPEED $U = 80[m.min^{-1}]$

Magnification (200×0.8)

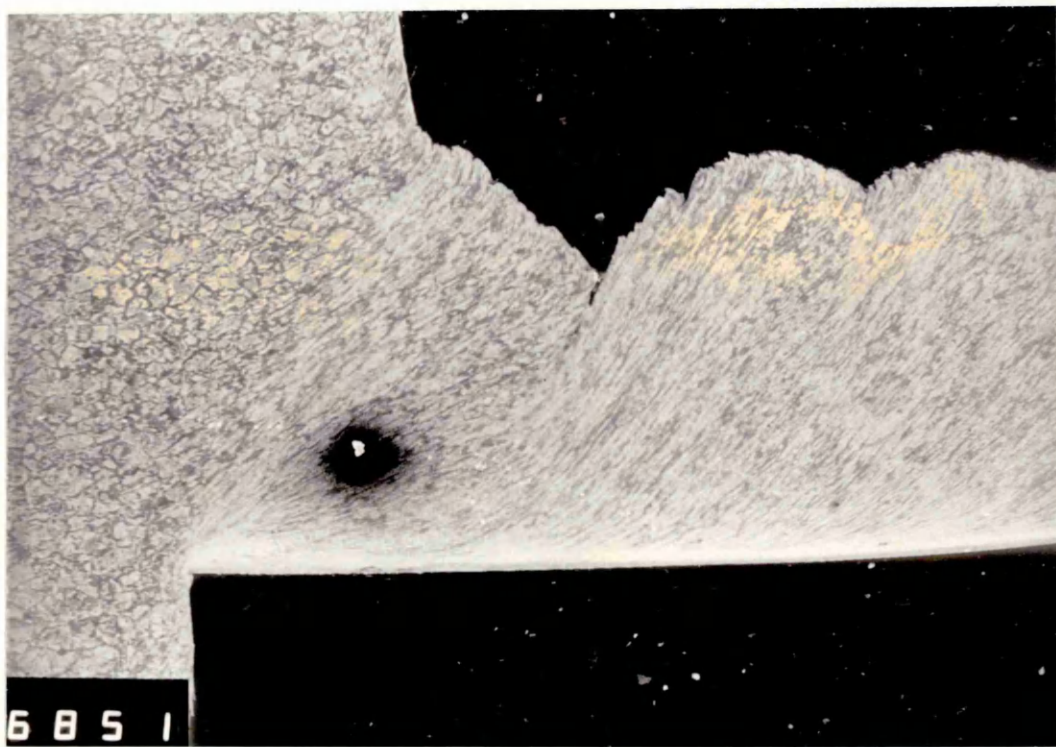


PLATE 18 : PRIMARY DEFORMATION ZONE WIDTH WHEN MACHINING

EN₀ AT SPEED U = 60[m.min⁻¹] ΔS₁ = 0.15mm

Magnification (50×0.8)

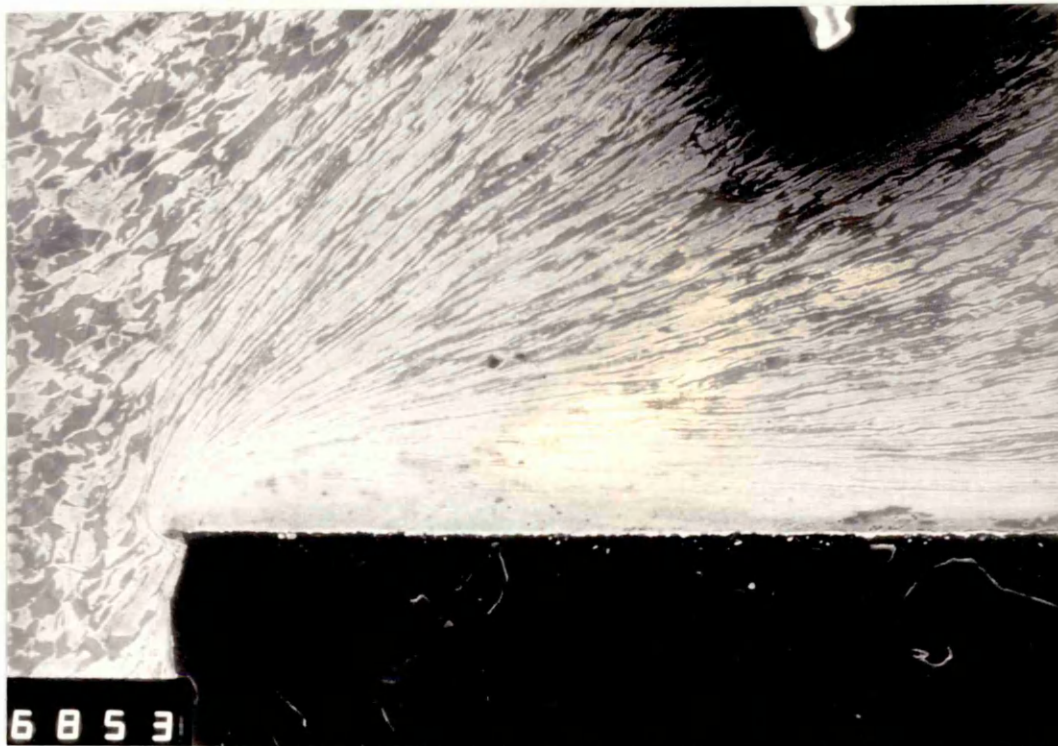


PLATE 19 : SECONDARY DEFORMATION ZONE WIDTH WHEN

MACHINING EN₀ AT SPEED U = 60[m.min⁻¹]

δt₂ = 0.086mm

Magnification (200×0.8)

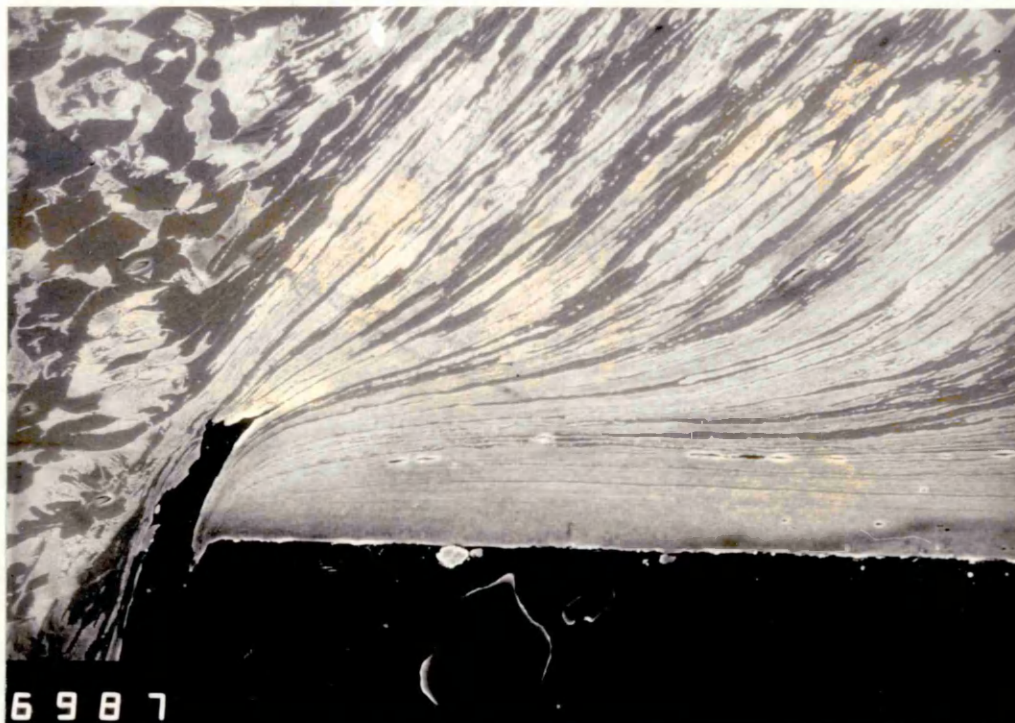


PLATE 20 : PRIMARY DEFORMATION ZONE WIDTH WHEN MACHINING

EN₀ AT SPEED U = 60[m.min⁻¹] ΔS₀ = 0.13mm

Magnification (400×0.8)

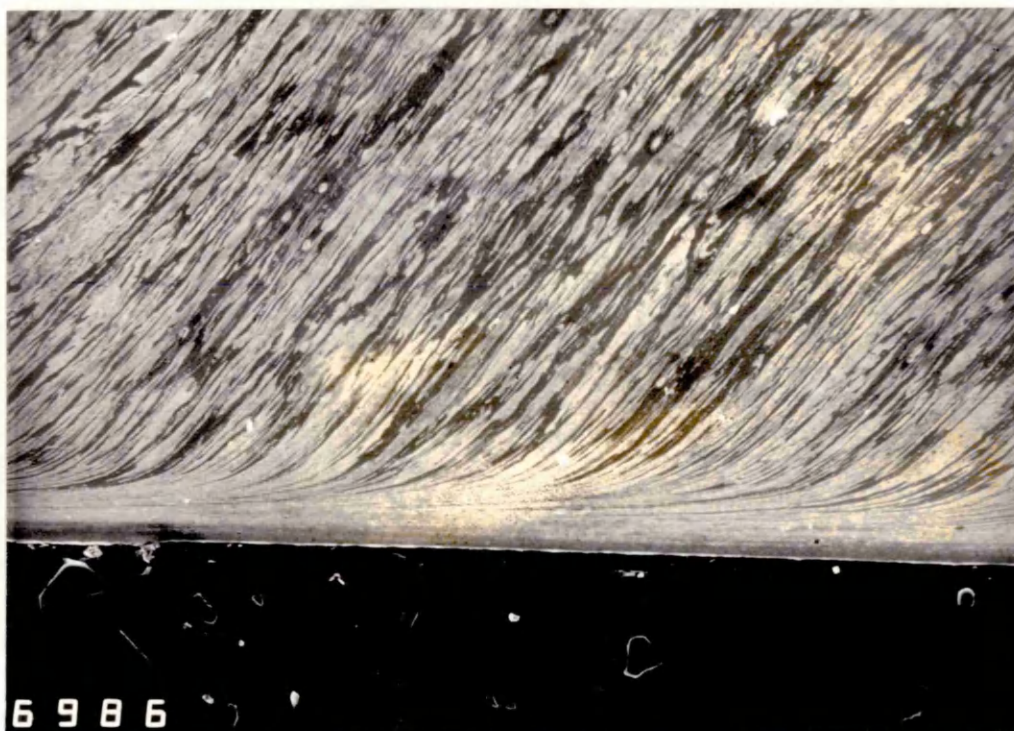


PLATE 21 : SECONDARY DEFORMATION ZONE WIDTH WHEN

MACHINING EN₀ AT SPEED U = 80[m.min⁻¹]

δt₀ = 0.064mm

Magnification (200×0.8)

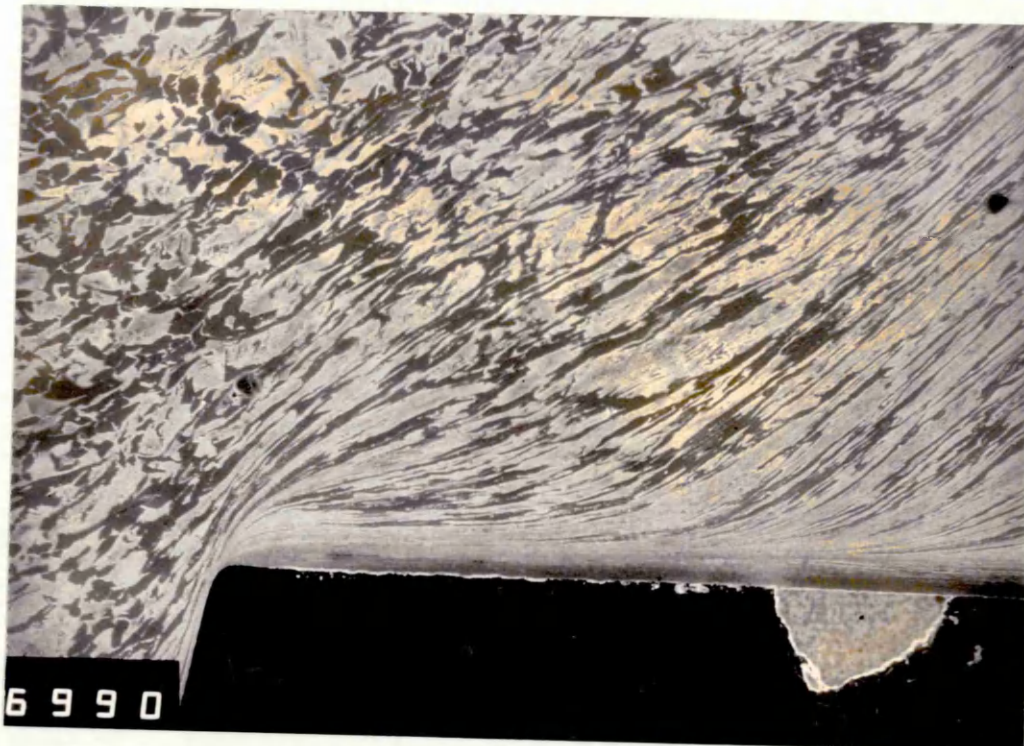


PLATE 22 : PRIMARY DEFORMATION ZONE WIDTH WHEN MACHINING

EN₈ AT SPEED U = 150[m.min⁻¹] ΔS₁ = 0.10mm

Magnification (200×0.8)

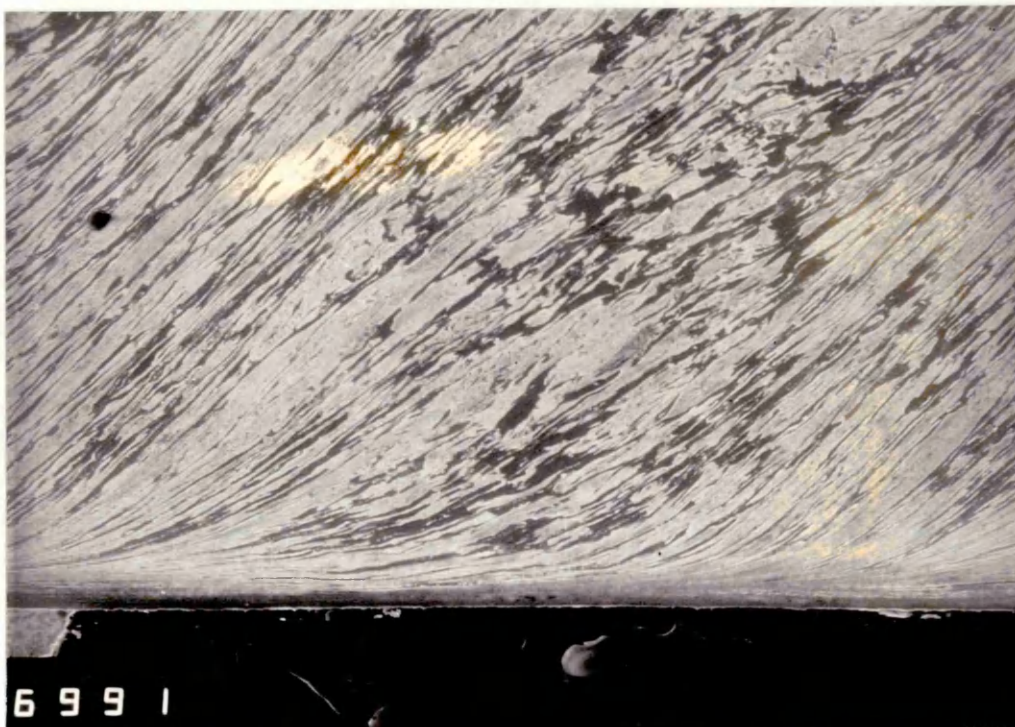


PLATE 23: SECONDARY DEFORMATION ZONE WIDTH WHEN

MACHINING EN₈ AT SPEED U = 150[m.min⁻¹],

δt₂ = 0.064mm

Magnification (200×0.8)



PLATE 24 : PRIMARY DEFORMATION ZONE WIDTH WHEN MACHINING

EN₀ AT SPEED U = 150[m.min⁻¹] ΔS₁ = 0.10mm

Magnification (400×0.8)

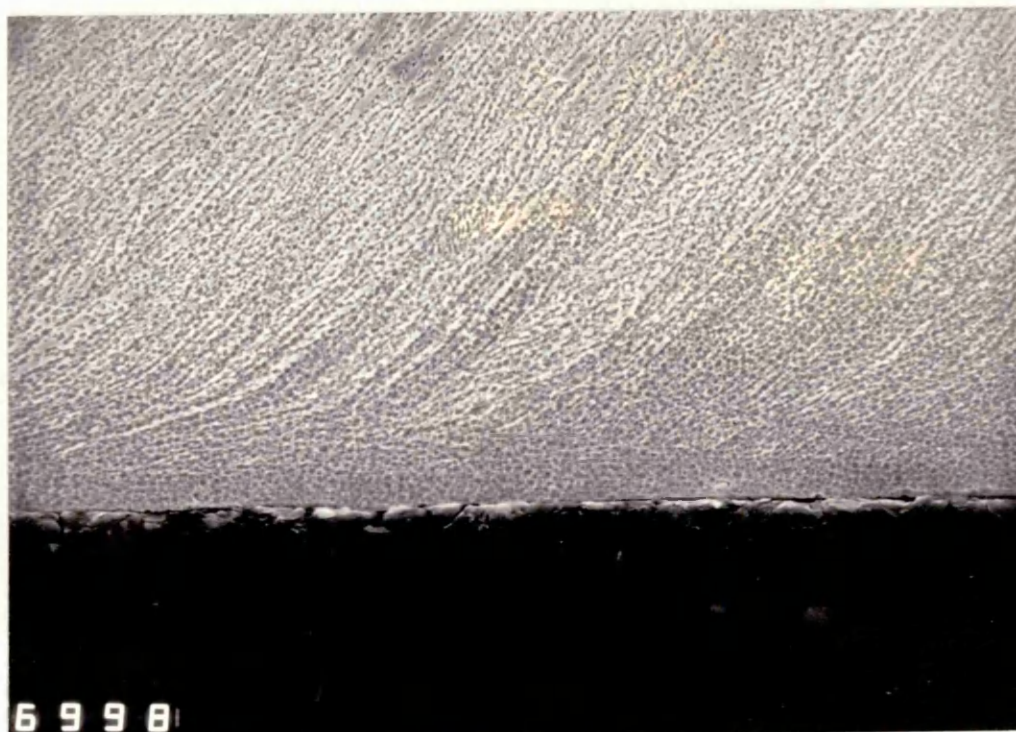


PLATE 25 : SECONDARY DEFORMATION ZONE WIDTH WHEN

MACHINING 70-30 BRASS AT SPEED U = 120[m.min⁻¹]

δt₂ = 0.029mm

Magnification (800×0.85)



PLATE 26 : SCANNING ELECTRON MICROSCOPE USED

APPENDIX I

DEMONSTRATION OF SOME EXPRESSIONS USED IN THE
SEMI-EMPIRICAL MODEL (CHAPTER 3)

DEMONSTRATION OF EXPRESSIONS

1. The expression for shear angle given in equation (3.1) is obtained from a geometric view-point as follows:

$$\tan \varphi = \frac{t_1/t_2 \cos \alpha}{1 - t_1/t_2 \cos \alpha}$$

In the geometry of Figure (59) it is shown that

- the triangle SBF gives:

$$\alpha + 90 + (z) = 180$$

so,

$$z = 180 - 90 - \alpha$$

$$z = 90 - \alpha$$

- and, from the triangle AEF:

$$z + 90 + y = 180$$

$$z = 90 - \alpha$$

therefore

$$90 - \alpha + 90 + y = 180$$

thus,

$$y = 180 - 90 - 90 + \alpha$$

$$y = \alpha$$

- if the distance AF (Figure 59) is equal to K then

$$\cos \alpha = \frac{t_2}{K}$$

and

$$K = \frac{t_2}{\cos \alpha}$$

$$\tan \alpha = \frac{m}{t_1} \quad \text{where } m = DC$$

$$m = t_1 \tan \alpha$$

then

$$\tan \varphi = \frac{t_1}{K - m}$$

and replacing K and m by their values so that,

$$\tan \varphi = \frac{t_1}{t_2/\cos \alpha - t_1 \tan \alpha}$$

$$\tan \varphi = \frac{t_1}{t_2/\cos \alpha - t_1 \frac{\sin \alpha}{\cos \alpha}}$$

and,

$$\tan \varphi = \frac{t_1/t_2 \cos \alpha}{1 - t_1/t_2 \sin \alpha}$$

2. The change in the hydrostatic stress Δp which occurs between A and B in Figure (27) and which is expressed in equation (3.4), is demonstrated as follows:

$$\Delta p = \Delta K \frac{\Delta S_2}{\Delta S_1}$$

Figure 2 shows an element of the small shear zone.

From the equilibrium it is obtained:

$$(P + \Delta p)\Delta S_1 + \left[K - \frac{\Delta K}{2}\right]\Delta S_2 = P\Delta S_1 + \left[K + \frac{\Delta K}{2}\right]\Delta S_2$$

$$(P + \Delta p)\Delta S_1 + \left[K - \frac{\Delta K}{2}\right]\Delta S_2 - P\Delta S_1 - \left[K + \frac{\Delta K}{2}\right]\Delta S_2 = 0$$

$$P\Delta S_1 + \Delta P\Delta S_1 + K\Delta S_2 - \frac{\Delta K}{2} \Delta S_2 - P\Delta S_1 - K\Delta S_2 - \frac{\Delta K}{2} \Delta S_2 = 0$$

$$\Delta P\Delta S_1 - \Delta K\Delta S_2 = 0$$

so,

$$\Delta P = \Delta K \frac{\Delta S_2}{\Delta S_1}$$

Integration of the expression

$$\Delta P = \Delta K \frac{\Delta S_2}{\Delta S_1}$$

along the shear plane AB gives:

$$\int_B^A \Delta P = \int_0^{\ell} \frac{\Delta K}{\Delta S_1} \Delta S_2$$

where,

$$\ell = AB = \frac{t_1}{\sin \varphi}$$

and

$$\frac{\Delta K}{\Delta S_1} \text{ is constant}$$

thus,

$$P_A - P_B = \frac{\Delta K}{\Delta S_1} \frac{t_1}{\sin \varphi}$$

3. The angle θ in equation (3.11) is determined geometrically as follows:

The geometry of Figure (60) gives:

- (a) from the triangle BDE:

$$180^\circ - \lambda + f + g = 180^\circ$$

- (b) from the triangle ABC:

$$\alpha + 90^\circ + 90^\circ - g = 180^\circ$$

and

- (c) the triangle GHF gives:

$$\varphi + f + 180^\circ - \theta = 180^\circ$$

from (b) it is obtained:

$$g = 180^\circ - 180^\circ + \alpha$$

$$g = \alpha$$

from (b) and (a) the following result is obtained

$$180^\circ - \lambda - f - \alpha = 180^\circ$$

thus

$$f = -\alpha + \lambda$$

and from (a) and (c), the following expression is obtained:

$$\varphi - \alpha + \lambda + 180 - \theta = 180$$

and

$$\theta = \varphi - \alpha + \lambda$$

4. The resultant cutting forces transmitted by the shear plane and the tool-chip interface given in equation (3.13) and the forces given in equation (3.14) are demonstrated as follows:

From Figure 26 it is shown that

$$\cos \theta = \frac{F_s}{R}$$

so,

$$R = \frac{F_s}{\cos \theta}$$

The shearing force F_s is expressed by:

$$F_s = K_{AB} \times A_s$$

where

K_{AB} is the shear stress

and

A_s is the area of shear plane.

A_s is then expressed by:

$$A_s = \omega \times \ell_{AB}$$

where

ω is the width of cut

and

ℓ_{AB} is the length of the shear plane expressed by

$$\ell_{AB} = \frac{t_1}{\sin \varphi} .$$

Thus,

$$F_s = K_{AB} \cdot \omega \cdot \frac{t_1}{\sin \varphi}$$

and the resultant cutting force is then

$$R = \frac{K_{AB} \cdot \omega \cdot t_1}{\sin \varphi \cos \theta}$$

$$\cos(\lambda - \alpha) = \frac{F_c}{R}$$

$$F_c = R \cos(\lambda - \alpha)$$

$$\sin(\lambda - \alpha) = \frac{F_t}{R}$$

$$F_t = R \sin(\lambda - \alpha)$$

APPENDIX II

AN EXAMPLE OF CALCULATING THE FORCES IN USING THE
SEMI-EMPIRICAL MODEL

An example of calculating the force in using the semi-empirical model (Chapter 3).

In order to show the semi-empirical model used to predict the cutting forces an example of the analytical results is given as follows:

- let
- the speed $U = 150\text{m}\cdot\text{min}^{-1}$
 - the undeformed chip thickness $t_1 = 0.488\text{mm}$
 - the width of cut (ie of the tube) $\omega = 3.15\text{mm}$.
 - the chip thickness $t_2 = 1.21\text{mm}$
- and
- the work material is a medium steel EN₈
 - the rake angle $\alpha = 0$

To begin with:

- the shear angle is determined by:

$$\tan \varphi = \frac{t_1/t_2 \cos \alpha}{1 - t_1/t_2 \sin \alpha} = 0.403$$

so, the angle φ is equal to $21^\circ 96'$

$$\varphi = 21^\circ 96'$$

- the hydrostatic stress p_A is calculated from

$$p_A = k_{AB} \left[1 + 2 \left[\frac{\pi}{2} - \varphi \right] \right]$$

the shear stress k_{AB} is determined from equation (3.12) as follows:

$$k_{AB} = \frac{\sigma_1}{\sqrt{3}} \varepsilon_{AB}^n$$

where $\sigma_1 = 940 \text{ MN}\cdot\text{m}^{-2}$ and $n = 0.1$ which are obtained from the compression test results (after plotting the stress-strain curve).

When the value of the angle φ is $21^{\circ}96'$, the shear strain occurring along the ship line AB in equation (3.9) will have the value of $\gamma_{AB} = 3.02$, thus the natural strain ϵ_{AB} equation (3.12) is

$$\epsilon_{AB} = \frac{1}{\sqrt{3}} \cdot \gamma_{AB} = 1.662.$$

Therefore,

$$k_{AB} = 573 \text{MN.m}^{-2}$$

and

$$p_A = 1059 \text{MN.m}^{-2}.$$

- The hydrostatic stress p_B is determined from:

$$p_B = p_A - \frac{\Delta k}{\Delta S_1} \cdot \frac{t_1}{\sin \varphi}$$

the value of Δk (the change in shear flow stress) is determined from equation (3.7)

$$\Delta k = m \gamma_{EF}$$

where m is found from idealized stress-strain curve (Figure 53) so that:

$$\Delta k = 28.13 \text{MN.m}^{-2}$$

$$m = 9$$

Thus,

$$p_B = 788 \text{MN.m}^{-2}$$

Then from equation (3.10) $\tan \theta = 1.61$ so, $\theta = 58^{\circ}18'$.

When the angle θ is calculated, equations (3.11), (3.13) and (3.14) are then obtained as:

- from equation (3.11) $\lambda = 37^{\circ}29'$

(3.13) $R = 4.728 \text{KN}$

and (3.14) gives $F_c = 3.75 \text{KN}$

$F_t = 2.87 \text{KN}.$

TABLE 4 : EXPERIMENTAL RESULTS - MATERIAL : EN₈

V	S	α	F _c	F _t
[M.MN ⁻¹]	[MM.REV ⁻¹]	[°]	[KN]	[KN]
30	.488	0°	5.250	4.350
60	-	-	4.700	4.000
80	-	-	3.500	2.500
120	-	-	3.000	1.850
150	-	-	2.950	1.550
250	-	-	2.900	1.250
400	-	-	2.700	1.050
200	.057	0°	.525	.500
-	.079	-	.675	.600
-	.099	-	.875	.750
-	.158	-	1.200	.837
-	.244	-	1.700	1.025
-	.334	-	2.075	1.025
-	.488	-	2.825	1.300
200	.244	-10	1.725	1.225
-	-	-5	1.650	1.075
-	-	0	1.650	1.025
-	-	+5	1.600	0.875
-	-	+10	1.575	.875
-	-	+15	1.350	.525
-	-	+20	1.350	.550
-	-	+25	1.425	.650

TABLE 5 : PREDICTED RESULTS - MATERIAL : EN₈

V [m.min ⁻¹]	30	60	80	120	150	250	400
t ₂ [mm]	2.19	1.745	1.588	1.390	1.292	1.092	0.936
φ[°]	12.56	15.62	17.08	19.34	20.69	24.07	27.53
γ _{AB}	4.71	3.85	3.56	3.20	3.02	2.685	2.44
ε _{AB}	2.72	2.22	2.05	1.84	1.74	1.55	1.40
K _{AB} [MN.m ⁻²]	600	587	583	576	573	567	561
ΔK[MN.m ⁻²]	42.32	34.59	31.98	28.75	27.13	24.12	21.92
P _A [MN.m ⁻²]	1278	1188	1150	1092	1059	980	902
P _B [MN.m ⁻²]	855	842	830	804	788	739	683
θ[°]	60.63	59.93	59.50	58.71	58.18	56.58	54.70
R[KN]	8.647	6.692	6.012	5.147	4.728	3.880	3.220
λ[°]	48.07	44.33	42.44	39.37	37.49	32.51	27.17
F _C [KN]	4.240	3.353	3.051	2.673	2.492	2.137	1.865
F _T [KN]	6.433	4.676	4.055	3.264	2.877	2.085	1.474
F _S [KN]	5.778	4.787	4.438	3.978	3.750	3.272	2.870

TABLE 6 : PREDICTED RESULTS - MATERIAL : EN₈

S [mm.rev ⁻¹]	.057	.079	.099	.158	.244	.334	.488
t ₂ [mm]	0.274	0.318	0.358	0.476	0.648	0.828	1.136
φ[°]	11.75	13.95	15.45	18.36	20.63	21.96	23.24
γ _{AB}	5.015	4.274	3.894	3.345	3.032	2.883	2.758
ε _{AB}	2.895	2.747	2.248	1.931	1.750	1.664	1.592
K _{AB} [MN.m ⁻²]	603	594	588	579	574	571	568
ΔK[MN.m ⁻²]	45	38.40	35	30	27.20	25.90	24.70
P _A [MN.m ⁻²]	1302	1237	1195	1117	1062	1030	1000
P _B [MN.m ⁻²]	852	853	845	817	790	771	753
θ[°]	60.75	60.38	60.03	59.08	58.20	57.62	57.05
R[KN]	1.088	1.240	1.377	1.780	2.376	3.000	4.068
λ[°]	49	46.43	44.58	40.72	37.57	35.66	33.81
F _S [KN]	0.531	0.612	0.687	0.914	1.252	1.606	2.121
F _C [KN]	0.713	0.854	0.980	1.349	1.883	2.437	3.380
F _T [KN]	0.821	0.898	0.966	1.160	1.448	1.749	2.260

TABLE 7 : PREDICTED RESULTS - MATERIAL : EN₈

α [°]	-10	-5	0	+5	+10	+15	+20	+25
t_2 [mm]	.653	.640	.630	.627	.607	.595	.584	.572
φ [°]	19.06	20.20	21.17	21.86	23.05	23.89	24.61	25.21
γ_{AB}	3.45	3.19	2.97	2.79	2.58	2.41	2.26	2.12
ε_{AB}	1.99	1.84	1.71	1.61	1.49	1.39	1.30	1.22
K_{AB} [MN.m ⁻²]	581	576	572	569	564	561	557	554
ΔK [MN.m ⁻²]	31	28.7	26.7	25	23	21.7	20	19
P_A [MN.m ⁻²]	1106	1074	1047	1028	995	974	953	936
P_B [MN.m ⁻²]	796	787	780	777	763	757	750	745
θ [°]	58.27	58.24	57.94	57.77	57.31	57.05	56.81	56.66
R [KN]	2.62	2.43	2.29	2.20	2.05	1.95	1.87	1.81
λ [°]	29.51	33.05	36.77	40.91	44.26	48.16	52.50	56.4
F_S [KN]	1.36	1.28	1.21	1.17	1.11	1.06	1.03	1.00
F_C [KN]	2.02	1.92	1.83	1.78	1.70	1.63	1.59	1.55
F_t [KN]	1.66	1.50	1.37	1.29	1.15	1.07	1.00	.946

TABLE 8 : EXPERIMENTAL RESULTS - MATERIAL : ALUMINIUM

V	S	α	F _c	F _t
[M.MN ⁻¹]	[MM.REV ⁻¹]	[°]	[KN]	[KN]
30	.488	0°	1.950	1.500
60	-	-	1.725	1.000
80	-	-	1.625	.875
120	-	-	1.500	.725
150	-	-	1.450	.675
250	-	-	1.275	.450
400	-	-	1.225	.365
200	.057	0°	.300	.200
-	.079	-	.370	.250
-	.099	-	.430	.310
-	.158	-	.580	.340
-	.244	-	.800	.420
-	.344	-	1.210	.490
-	.488	-	1.320	.510
200	.244	-10	.850	.530
-	-	-5	.810	.460
-	-	0	.800	.410
-	-	+5	.800	.410
-	-	+10	.720	.300
-	-	+15	.720	.300
-	-	+20	.670	.220
-	-	+25	.650	.230

TABLE 9 : PREDICTED RESULTS - MATERIAL : ALUMINIUM

V [m.min ⁻¹]	30	60	80	120	150	250	400
t ₂ [mm]	2.37	1.95	1.80	1.60	1.51	1.31	1.15
φ [°]	11.63	14.05	15.16	16.96	17.90	20.43	23
γ _{AB}	5.06	4.24	3.96	3.58	3.42	3.06	2.78
ε _{AB}	2.92	2.44	2.28	2.06	1.97	1.76	1.60
K _{AB} [MN.m ²]	229	225	224	222	221	218	216
ΔK [MN.m ⁻²]	19	16	15	13.6	13	11.6	10.5
P _A [MN.m ⁻²]	495	468	457	439	430	405	382
P _B [MN.m ⁻²]	305	308	307	303	300	289	277
θ [°]	60.20	59.89	56.61	59.10	58.80	57.86	56.75
R [KN]	3.57	2.88	2.65	2.31	2.16	1.83	1.57
λ [°]	48.57	45.84	44.45	42.14	40.9	37.43	33.75
F _S [KN]	1.77	1.44	1.33	1.18	1.12	.97	.86
F _C [KN]	2.35	2.00	1.88	1.71	1.63	1.45	1.31
F _t [KN]	2.67	2.07	1.85	1.55	1.41	1.11	.87

TABLE 10 : PREDICTED RESULTS - MATERIAL : ALUMINIUM

S [mm.rev ⁻¹]	.057	.079	.099	.158	.244	.334	.488
t ₂ [mm]	.31	.36	.41	.55	.76	.99	1.36
φ[°]	10.41	12.37	13.57	16.02	17.79	18.64	19.74
γ _{AB}	5.62	4.78	4.38	3.76	3.43	3.30	3.14
ε _{AB}	3.24	2.76	2.52	2.17	1.98	1.90	1.81
K _{AB} [MN.m ⁻²]	231	227	226	223	221	220	219
ΔK[MN.m ⁻²]	21	18	16.6	14	13	12.5	12
P _A [MN.m ⁻²]	509	485	473	448	430	422	412
P _B [MN.m ⁻²]	293	305	307	306	300	297	292
θ[°]	60	60.11	59.9	59.4	58.8	58.5	58.11
R[KN]	.46	.53	.61	.80	1.09	1.41	1.91
λ[°]	49.6	47.7	46.3	43.4	41	39.9	38.4
F _S [KN]	.23	.26	.30	.41	.58	.73	1.01
F _C [KN]	.30	.36	.42	.58	.82	1.08	1.50
F _t [KN]	.35	.39	.44	.55	.71	.91	1.19

TABLE 11 : PREDICTED RESULTS - MATERIAL : ALUMINIUM

α [°]	-10	-5	0	+5	+10	+15	+20	+ 25
t_2 [mm]	.95	.91	.87	.83	.79	.75	.70	
φ [°]	13.37	14.67	15.64	16.73	17.76	18.92	21.55	
γ_{AB}	4.64	4.19	3.85	3.53	2.98	2.56		
ϵ_{AB} [MN.m ⁻²]	2.67	2.42	2.22	2.04	1.87	1.72	1.47	
K_{AB} [MN.m ⁻²]	227	225	223	221	219	218	215	
ΔK [MN.m ⁻²]	17.6	16	14.6	13.4	12.3	11.3	9.7	
P_A [MN.m ⁻²]	477	463	451	438	427	416	390	
P_B [MN.m ⁻²]	301	303	305	304	303	303	293	
θ [°]	59.73	59.56	59.46	59.21	59.07	58.76	57.8	
R [KN]	1.44	1.37	1.27	1.17	1.09	.98	.85	
λ [°]	36.36	39.9	43.8	47.5	51.31	54.84	56.25	
F_S [KN]	.72	.69	.64	.60	.56	.51	.45	
F_C [KN]	.99	.97	.92	.86	.82	.75	.69	
F_t [KN]	1.04	.97	.88	.79	.72	.63	.51	

TABLE 12 : EXPERIMENTAL RESULTS - MATERIAL : 70-30 BRASS

V	S	α	F_c	F_t
[m.min ⁻¹]	[mm.rev ⁻¹]	[°]	[KN]	[KN]
20	.244	0	.870	.480
30	-	-	.850	.500
60	-	-	.830	.510
80	-	-	.840	.500
120	-	-	.850	.500
150	-	-	.850	.500
250	-	-	.880	.450
400	-	-	.910	.440
200	.057	0	.270	.180
-	.079	-	.360	.250
-	.099	-	.430	.280
-	.158	-	.650	.380
-	.244	-	.880	.470
-	.334	-	1.080	.560
-	.488	-	1.400	.650
200	.244	-10	.830	.650
-	-	-5	.810	.480
-	-	0	.830	.510
-	-	+5	.840	.520
-	-	+10	.840	.420
-	-	+15	.850	.370
-	-	+20	.830	.300
-	-	+25	.830	.310

TABLE 13 : PREDICTED RESULTS - MATERIAL : 70-30 BRASS

V [m.min ⁻¹]	20	30	60	80	120	150	250	400
t ₂ [mm]	.53	.516	.485	.47	.456	.44	.428	.41
φ[°]	24.72	25.30	26.70	27.43	28.15	29.01	29.68	30.75
γ _{AB}	2.63	2.58	2.49	2.44	2.40	2.35	2.32	2.27
ε _{AB}	1.51	1.49	1.43	1.40	1.38	1.35	1.34	1.31
K _{AB} [MN.m ⁻²]	390	388	383	380	379	376	375	372
ΔK[MN.m ⁻²]	79	77.4	74.7	73.2	72	70.5	60.5	68
P _A [MN.m ⁻²]	666	655	627	613	602	585	575	557
P _B [MN.m ⁻²]	-124	-119	-120	-119	-118	-120	-121	-123
θ[°]	34.79	34.60	33.49	33.02	32.56	31.78	31.18	30.25
R[KN]	.928	.903	.835	.804	.779	.745	.723	.688
λ[°]	10.07	9.3	6.79	5.59	4.41	2.72	1.5	-0.5
F _S [KN]	.762	.743	.700	.673	.656	.633	.618	.594
F _C [KN]	.914	.89	.83	.80	.777	.744	.723	.688
F _t [KN]	.162	.146	.100	.078	.06	.035	.019	0

TABLE 14 : PREDICTED RESULTS - MATERIAL : 70-30 BRASS

S							
[mm.rev ⁻¹]	.057	.079	.099	.158	.244	.334	.488
t ₂ [mm]	.17	.20	.22	.30	.38	.51	.70
φ[°]	18.04	21.44	24.22	27.8	32.7	33.2	34.8
γ _{AB}	3.40	2.92	2.67	2.42	2.20	2.18	2.13
ε _{AB}	1.95	1.68	1.54	1.40	1.27	1.25	1.23
K _{AB} [MN.m ⁻²]	424	404	392	380	368	366	364
ΔK[MN.m ⁻²]	101	87	80	73	66	65	64
P _A [MN.m ⁻²]	823	735	676	608	526	516	492
P _B [MN.m ⁻²]	-194	-143	-125	-188	-134	-138	-147
θ[°]	36.5	36.2	35	32.8	28	27.3	25.3
R[KN]	.32	.36	.38	.51	.63	.84	1.15
λ[°]	18.52	14.6	10.7	5.04	-4.66	-5.91	-9.53
F _S [KN]	.26	.29	.31	.43	.55	.75	1.04
F _C [KN]	.30	.35	.38	.51	.62	.83	1.13
F _t [KN]	.10	.09	.07	.04	-0.05	-0.08	-0.19

TABLE 15 : PREDICTED RESULTS - MATERIAL : 70-30 BRASS

α [$^{\circ}$]	-10	-5	0	+5	+10	+15	+20	+25
t_2 [mm]	0.4	0.4	0.41	0.42	0.42	0.43	0.43	0.44
φ [$^{\circ}$]	28.48	29.64	30.66	31.55	32.22	32.75	33.11	33.18
γ_{AB}	2.63	2.44	1.18	1.12	1.99	1.87	1.76	1.67
ϵ_{AB}	1.51	1.40	1.31	1.22	1.15	1.08	1.01	0.96
K_{AB} [MN.m $^{-2}$]	390	380	372	363	356	349	342	336
ΔK [MN.m $^{-2}$]	79	73	68	63.6	59.7	56	53	50
P_A [MN.m $^{-2}$]	615	599	558	553	515	498	484	474
P_B [MN.m $^{-2}$]	-175	-133	-126	-103	-82	-63	-44	-26
θ [$^{\circ}$]	29.4	31.51	30.14	30.64	31.30	31.93	32.75	33.69
R [KN]	.767	.736	.689	.659	.639	.621	.608	.603
λ [$^{\circ}$]	-9.06	-3.13	-0.52	4.08	9.08	14.18	19.64	25.51
F_S [KN]	.668	.627	.595	.567	.546	.527	.511	.501
F_C [KN]	.767	.736	.689	.659	.639	.621	.608	.603
F_t [KN]	.006	.024	-0.006	-0.01	-0.01	-0.007	-0.003	-0.005

TABLE 16 : CHIP THICKNESS RATIO VERSUS CUTTING SPEED

Speed U [m.min ⁻¹]	Chip thickness ratio $r_c = t_1/t_2$		
	EN ₈	Aluminium	70-30 Brass
20	-	-	0.460
30	0.222	0.206	0.472
60	0.280	0.250	0.503
80	0.307	0.271	0.519
120	0.351	0.305	0.535
150	0.377	0.323	0.554
250	0.446	0.372	0.570
400	0.525	0.424	0.595

TABLE 17 : CHIP THICKNESS RATIO VERSES UNDEFORMED CHIP THICKNESS

Undeformed Chip Thickness t_1 [mm.rev ⁻¹]	Chip thickness ratio $r_c = t_1/t_2$		
	EN ₈	Aluminium	70-30 Brass
0.057	0.208	0.183	0.335
0.079	0.248	0.220	0.395
0.099	0.276	0.241	0.450
0.158	0.320	0.287	0.526
0.244	0.376	0.321	0.642
0.334	0.403	0.337	0.655
0.488	0.430	0.358	0.697

TABLE 18 : CHIP THICKNESS RATIO VERSES RAKE ANGLE

Rake Angle α (degree)	Chip thickness ratio $r_c = t_1/t_2$		
	EN ₈	Aluminium	70-30 Brass
-10	0.373	0.256	0.61
-5	0.381	0.268	0.61
0	0.387	0.280	0.591
+5	0.389	0.293	0.581
+10	0.402	0.308	0.581
+15	0.410	0.325	0.567
+20	0.417	0.348	0.567
+25	0.426	-	0.555

TABLE 19 : BUILT-UP EDGE SIZE VERSUS SPEED WHEN MACHINING

EN₈

Speed V[m.min ⁻¹]	Built-up edge BUE
30	0.07
60	0.048
80	0.048
150	0.024

TABLE 20 : LENGTH/WIDTH OF THE PRIMARY SHEAR ZONE VERSUS CUTTING SPEED WHEN MACHINING EN₈

	Speed V[m.min ⁻¹]	L _s /Δ _s
	30	8.19
	60	11.96
EN ₈	80	12.19
	150	13.62
Brass	120	8.87

TABLE 21 : THE CONSTANT δ IN THE WIDTH OF THE SECONDARY SHEAR ZONE δt₂ VERSUS SPEED WHEN MACHINING EN₈

	Speed V[m.min ⁻¹]	δ
	30	0.06
	60	0.055
EN ₈	80	0.04
	150	0.051
Brass	120	0.049

TABLE 22 : PREDICTED RESULTS FOR EN₈

$$\frac{t_1}{\Delta S_1 \sin \varphi} = 6$$

V[m.min ⁻¹]	30	60	80	120	150	250	400
t ₂ [mm]	2.19	1.745	1.588	1.390	1.292	1.092	0.976
φ[°]	12.56	15.69	17.00	19.34	20.69	24.07	27.53
γ _{AB}	4.71	3.85	3.56	3.20	3.02	2.685	2.44
ε _{AB}	2.72	2.22	2.05	1.84	1.74	1.55	1.40
K _{AB} [MN.m ⁻²]	600	587	583	576	573	567	561
ΔK[MN.m ⁻²]	42.32	34.59	31.98	28.75	27.13	24.12	21.92
P _A [MN.m ⁻²]	1278	1188	1150	1092	1059	980	902
P _B [MN.m ⁻²]	1024	980	958	920	897	835	768
θ[°]	62.46	61.56	61.05	60.20	59.63	58	56.10
R[KN]	9320	7148	6394	5465	5000	4100	3400
λ[°]	49.9	46	44	40.86	39	34	28.5
F _c [KN]	6000	4965	4600	4130	3885	3400	2990
F _t [KN]	7130	5140	4440	3575	3146	2300	1622
ΔS ₁ [mm]	0.373	0.302	0.276	0.245	0.230	0.199	0.175

TABLE 23 : PREDICTED RESULTS FOR EN₈

$$\text{when } \frac{t_1}{\Delta S_1 \sin \varphi} = 14$$

V[m.min ⁻¹]	30	60	80	120	150	250	400
t ₂ [mm]	2.19	1.745	1.588	1.390	1.292	1.092	0.936
φ[°]	17.56	15.62	17.08	19.34	20.69	24.07	27.53
γ _{AB}	4.71	3.85	3.56	3.20	3.02	2.685	2.44
ε _{AB}	2.72	2.22	2.05	1.84	1.74	1.55	1.40
K _{AB} [MN.m ⁻²]	600	587	583	576	573	567	561
ΔK[MN.m ⁻²]	42.32	34.59	31.98	28.75	27.13	24.12	21.92
P _A [MN.m ⁻²]	1278	1188	1150	1092	1059	980	902
P _B [MN.m ⁻²]	685.52	703.74	702.28	689.5	679	642	595
θ[°]	58.56	58.18	57.81	57.10	56.60	55	53.15
R[KN]	8260	6456	5818	4997	4600	3795	3160
λ[°]	46	42.56	40.73	37.76	36	31	25.63
F _C [KN]	5738	4755	4400	3950	3720	3250	2850
F _t [KN]	5940	4366	3800	3060	2700	1955	1366
ΔS ₁ [mm]	0.160	0.129	0.118	0.105	0.098	0.085	0.075

TABLE 24 : PREDICTED RESULTS FOR EN₈

$$\text{when } \frac{t_1}{\Delta S_1 \sin \varphi} = 50$$

V[m.min ⁻¹]	30	60	80	120	150	250	400
t ₂ [mm]	2.19	1.745	1.588	1.390	1.292	1.092	0.936
φ[°]	12.56	15.62	17.08	19.34	20.69	24.07	27.53
γ _{AB}	4.71	3.85	3.56	3.20	3.02	2.685	2.44
ε _{AB}	2.72	2.72	7.05	1.84	1.74	1.55	1.40
K _{AB} [MN.m ⁻²]	600	587	583	576	573	567	561
ΔK[MN.m ⁻²]	42.32	34.59	31.98	28.75	27.13	24.12	21.92
P _A [MN.m ⁻²]	1278	1188	1150	1092	1059	980	902
P _B [MN.m ⁻²]	-838	-540	-450	-345.5	-297.5	-226	-194
θ[°]	20.13	28.89	30.97	32.94	33.60	33.62	32.25
R[KN]	4589	3888	3615	3236	3040	2600	2240
λ[°]	7.57	13.27	13.89	13.60	12.91	9.55	4.75
F _C [KN]	4550	3784	3509	3145	2960	2564	2233
F _t [KN]	604	892	867	760	678	431	185
ΔS ₁ [mm]	0.044	0.036	0.033	0.029	0.027	0.023	0.021

TABLE 25 : PREDICTED RESULTS FOR ALUMINIUM

$$\text{when } \frac{t_1}{\Delta S_1 \sin \varphi} = 6$$

$V[\text{m.min}^{-1}]$	30	60	80	120	150	250	400
$t_2[\text{mm}]$	2.37	1.95	1.80	1.60	1.51	1.31	1.15
$\varphi[^\circ]$	11.63	14.05	15.16	16.96	17.90	20.43	23
γ_{AB}	5.06	4.24	3.96	3.58	3.42	3.06	2.78
ϵ_{AB}	2.92	2.44	2.28	2.06	1.97	1.76	1.60
$K_{AB}[\text{MN.m}^{-2}]$	229	225	224	222	221	218	216
$\Delta K[\text{MN.m}^{-2}]$	19	16	15	13.6	13	11.6	10.5
$P_A[\text{MN.m}^{-2}]$	495	468	457	439	430	405	382
$P_B[\text{MN.m}^{-2}]$	381	372	367	357	352	335	320
$\theta[^\circ]$	62.39	61.82	61.46	60.84	60.52	59.50	58.39
$R[\text{KN}]$	3827	3065	2800	2440	2280	1920	1647
$\lambda[^\circ]$	50.76	47.8	46.30	43.8	42.62	39	35.39
$F_c[\text{KN}]$	2420	2060	1935	1760	1675	1490	1340
$F_t[\text{KN}]$	2965	2270	2025	1688	1545	1210	955
$\Delta S_1[\text{mm}]$	0.40	0.333	0.309	0.277	0.263	0.232	0.207

TABLE 26 : PREDICTED RESULTS FOR ALUMINIUM

$$\text{when } \frac{t_1}{\Delta S_1 \sin \varphi} = 14$$

V[m.min ⁻¹]	30	60	80	120	150	250	400
t ₂ [mm]	2.37	1.95	1.80	1.60	1.51	1.31	1.15
φ[°]	11.63	14.05	15.16	19.96	17.90	20.43	23
γ _{AB}	5.06	4.24	3.96	3.58	3.42	3.06	2.78
ε _{AB}	2.92	2.44	2.28	2.06	1.97	1.76	1.60
K _{AB} [MN.m ⁻²]	229	225	224	222	221	218	216
ΔK[MN.m ⁻²]	19	16	15	13.6	13	11.6	10.5
P _A [MN.m ⁻²]	495	468	457	439	430	405	382
P _B [MN.m ⁻²]	229	244	247	248	248	243	235
θ[°]	57.68	57.70	57.52	57.12	56.90	56	55
R[KN]	3318	2708	2490	2190	2056	1745	1505
λ[°]	46	43.65	42.63	40.16	39	35.60	32
F _c [KN]	2305	1960	1832	1675	1598	1418	1276
F _t [KN]	2386	1870	1686	1412	1294	1015	737
ΔS ₁ [mm]	0.173	0.143	0.133	0.120	0.113	0.099	0.089

TABLE 27 : PREDICTED RESULTS FOR 70-30 BRASS

$$\text{when } \frac{t_1}{\Delta S_1 \sin \varphi} = 6$$

V[m.min ⁻¹]	20	30	60	80	120	150	250	400
t ₂ [mm]	.53	.516	.485	.47	.456	.44	.428	.41
φ[°]	24.72	25.30	26.70	27.43	28.15	29.01	29.68	30.75
γ _{AB}	2.63	2.58	2.49	2.44	2.40	2.35	2.32	2.27
K _{AB}	390	388	383	380	379	376	375	372
ΔK[MN.m ⁻²]	79	77.4	74.7	73.2	72	70.5	69.5	68
P _A [MN.m ⁻²]	666	655	627	613	602	585	575	557
P _B [MN.m ⁻²]	192	190	179	174	170	162	158	149
θ[°]	47.72	47.43	46.45	4.6	45.52	44.80	44.34	43.50
R[KN]	1133	1097	1011	970	937	893	865	820
λ[°]	23	22.13	19.75	18.57	17.37	15.8	14.66	12.75
F _C [KN]	1043	1016	950	920	895	860	836	780
F _t [KN]	442	413	341	310	280	243	220	180
ΔS ₁ [mm] (6)	0.097	0.093	0.089	0.086	0.084	0.0825	0.082	0.079
ΔS ₁ [mm] (10)	0.058	0.057	0.054	0.053	0.052	0.050	0.049	0.047

TABLE 28 : PREDICTED RESULTS FOR 70-30 BRASS

$$\text{when } \frac{t_1}{\Delta S_1 \sin \varphi} = 6$$

V[m.min ⁻¹]	20	30	60	80	120	150	250
t ₁ [mm]	0.057	0.079	0.099	0.158	0.244	0.334	0.488
φ[°]	18.04	21.44	24.22	27.8	32.7	33.2	34.8
γ _{AB}	3.40	2.92	2.67	2.42	2.20	2.18	2.13
ε _{AB}	1.95	1.68	1.54	1.40	1.27	1.25	1.23
K _{AB} [MN.m ⁻²]	425	404	392	380	368	366	364
ΔK[MN.m ⁻²]	101	87	80	73	66	65	64
P _A [MN.m ⁻²]	823	735	676	608	526	516	492
P _B [MN.m ⁻²]	212	213	196	170	130	126	108
θ[°]	50.67	49.55	48.04	45.67	41.71	41.25	39.49
R[KN]	412.5	450.85	474	617	745	995	1350
λ[°]	32.63	28.11	23.82	17.87	9.01	8.05	4.69
F _c [KN]	347.4	397.6	433.6	587	736	985	1346
F _t [KN]	222	212	191	189	116.5	139	110
ΔS ₁ [mm] (6)	0.030	0.036	0.040	0.056	0.075	0.101	0.142
ΔS ₁ [mm] (10)	0.018	0.021	0.024	0.033	0.045	0.061	0.085

TABLE 29 : PREDICTED RESULTS - MATERIAL : EN8

V [m.min ⁻¹]	30	60	80	120	150	250	400
t ₂ [mm]	2.327	1.807	1.626	1.403	1.293	1.073	.904
φ [°]	11.94	15.11	16.70	19.18	20.61	24.45	28.36
γ _{AB}	2.485	1.98	1.81	1.61	1.51	1.32	1.20
ε _{AB}	1.44	1.15	1.05	.93	.87	.76	.69
K _{AB} [MN.m ⁻²]	562	550	545	538	535	528	523
θ [°]	57.43	55.46	54.40	52.64	51.56	48.39	44.71
R [KN]	7.82	5.72	5.00	4.15	3.75	2.95	2.38
λ [°]	45.61	40.35	37.70	33.46	30.89	23.94	16.35
F _S [KN]	4.21	3.24	2.90	2.50	2.33	1.96	1.70
F _f [KN]	5.60	3.70	3.06	2.28	1.92	1.20	.67
N [KN]	5.47	4.36	3.96	3.46	3.21	2.70	2.30
F _C [KN]	5.47	4.36	3.96	3.46	3.21	2.70	2.30
F _t [KN]	5.60	3.70	3.06	2.28	1.92	1.20	.67

TABLE 30 : PREDICTED RESULTS - MATERIAL : EN8

S [min.rev ⁻¹]	0.057	.079	.099	.158	.244	.334	.488
t ₂ [mm]	.274	.318	.358	.476	.648	.828	1.136
φ[°]	11.75	13.95	15.45	18.36	20.63	21.96	23.24
γ _{AB}	2.50	2.14	1.95	1.67	1.52	1.44	1.38
ε _{AB}	1.44	1.23	1.12	0.96	0.87	0.83	0.79
K _{AB} [MN.m ⁻²]	562	554	548	540	535	532	530
θ[°]	57.50	56.18	55.22	53.26	51.56	50.50	49.43
R[KN]	.922	1.032	1.125	1.430	1.877	2.350	3.175
λ[°]	45.75	42.23	39.77	35	31	28.54	26.20
F _S [KN]	.495	.57	.64	.85	1.17	1.50	2.07
F[KN]	0.66	0.69	0.71	0.82	0.97	1.12	1.40
N[KN]	0.64	0.76	0.86	1.17	1.61	2.07	2.85
F _C [KN]	0.64	0.76	0.86	1.17	1.61	2.07	2.85
F _t [KN]	0.66	0.69	0.72	0.82	0.97	1.12	1.40

TABLE 31 : PREDICTED RESULTS - MATERIAL : EN_s

α [°]	-10	-5	0	+5	+10	+15	+20	+25
t_2 [mm]	.653	.641	.630	.627	.607	.595	.584	.572
φ [°]	19.06	20.19	21.17	21.86	23.05	23.89	24.61	25.71
γ_{AB}	1.725	1.60	1.48	1.40	1.29	1.27	1.13	1.06
ϵ_{AB}	0.995	.923	.954	.808	.745	.733	.652	.612
K_{AB} [MN.m ⁻²]	542	538	534	531	527	526	520	516
θ [°]	52.12	51.89	51.11	50.59	49.60	48.91	48.26	47.72
R [KN]	2.100	1.940	1.800	1.700	1.600	1.500	1.440	1.400
λ [°]	23.66	26.7	29.94	33.74	36.55	40.02	43.65	47.51
F_S [KN]	1.27	1.20	1.13	1.08	1.04	.985	.960	.940
F_C [KN]	1.75	1.65	1.56	1.50	1.43	1.36	1.32	1.30
F_t [KN]	1.16	1.02	.90	.82	.715	.635	.58	.536